UNIVERSITÀ DEGLI STUDI MILANO-BICOCCA
Scuola di Dottorato in Scienze Mediche Sperimentali
e Cliniche
Dottorato in Tecnologie Biomediche

Evaluation of morphological and structural variations in parotid glands during radiotherapy in the head-and-neck district.

Internal tutor: Prof.ssa Rosa Maria Moresco
External tutor: Ing. Giovanna Rizzo

PhD Thesis of:
Elisa Scalco
Matr. 744864

XXVI Ciclo - 2013

A Massimiliano

Summary

Introduction

The treatment of head and neck cancer (HNC) patients is one of the widest applications of radiation treatment; in fact, intensity-modulated radiotherapy (IMRT) is able to provide high dose conformity and homogeneity on complex-shaped targets, allowing at the same time a concomitant sparing of the surrounding organs at risk (OARs) (Eisbruch *et al* 2001). Nevertheless, a complete sparing of some critical structures is quite impossible, thus not preventing the appearance of critical side-effects. One of the main organs involved in dose delivery in HN district and playing a relevant role in the quality of life of patients is the parotid gland, the major salivary gland, responsible of the half of the total saliva secretion, whose damage causes a pathologic condition called xerostomia (Konings *et al* 2005).

During the treatment, HNC patients may undergo significant anatomical changes, like the shrinkage of the primary tumor and nodal volumes, weight loss and alteration in muscle mass and fat distribution. Several studies have focused on anatomical variations of the parotid glands: it was generally reported that parotids shrink during RT with a shift of the center of mass (COM) toward the midline (Barker Jr *et al* 2004, Hansen *et al* 2006, Robar *et al* 2007, Broggi *et al* 2010, Bhide *et al* 2010, Vásquez Osorio *et al* 2008). These modifications cause a translation of the glands into the high dose region, thus the effective delivered dose on parotids is significantly higher than that planned (Robar *et al* 2007, Hansen *et al* 2006, Han *et al* 2008).

The reported parotid shrinkage was found to be correlated with the mean parotid dose (Hansen *et al* 2006, Bhide *et al* 2010, Vásquez Osorio *et al* 2008, Broggi *et al* 2010) and also the risk of xerostomia was demonstrated to be strictly related to the dose-

volume histogram (Eisbruch *et al* 2001, Jellema *et al* 2005, Deasy *et al* 2010, Bussels *et al* 2004, Beetz *et al* 2012). Although there are a very limited number of studies reporting a direct influence of parotid volume decrease in the development of xerostomia in human (Teshima *et al* 2010), it is clear that a relationship between these two conditions exists.

Therefore, the study of local changes in parotid glands due to irradiation is still an open challenge, and the exploitation of the information content in medical images acquired during the radiation treatment is of practical interest for the non-invasiveness of these techniques. Along this line of research, recently some groups have developed new approaches aimed to assess structural and anatomical variations in parotid tissue by studying grey-level variations in terms of local patterns (Teshima *et al* 2012, Obinata *et al* 2013, Houweling *et al* 2011, Kan *et al* 2010, Yang *et al* 2012).

The aim of this work was thus to extensively evaluate morphological and structural modifications induced by RT on parotid glands using image-based indices extracted from CT images acquired during the treatment. In particular, in this PhD project it was proposed to estimate morphological changes by the deformation of the glands, evaluated by applying a non-rigid registration method optimized and validated on CT images of the HN district. Secondly, a method of image analysis based on textural feature extraction was proposed to characterize structural variations of parotid tissue. All these methods were evaluated and optimized for the specific clinical problem and all these parameters were studied in relation to dosimetric and clinical indices and to the clinical outcome, in order to better assess their contribution in this research field.

Methods

Parotid deformation was here estimated through an image registration and contour propagation method (Faggiano *et al* 2011). The adopted registration method was a classic sum of rigid and elas-

tic transformation, modeled by a cubic B-spline hyperpatch (Rueckert *et al* 1999); the algorithm used mutual information and a four-step multi-resolution strategy (Mattes *et al* 2003). After the estimation of the deformation field between the two images, a contour propagation method is needed to obtain a spatial correspondence of the considered structures of interest. The contour propagation method consists of a surface 3D mesh generation step followed by a mesh deformation step; the final deformed contours are obtained by cutting the deformed object through the transversal plane (see Figure A.1).

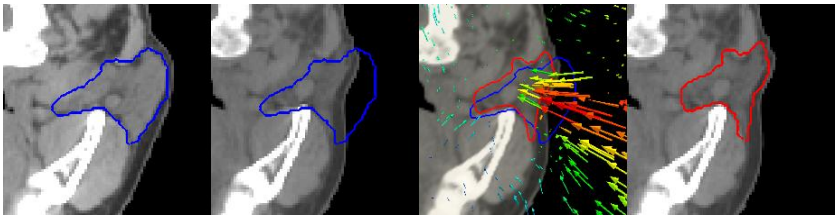

Figure A.1. Description of contour propagation algorithm. From left to right: parotid contour manually drawn on CT1; parotid contour manually drawn on CT1 visualized on CT2; displacement map; deformed contour visualized on CT2.

A deep validation of this method was performed to assess the accuracy of contour propagation method and to ensure a reliable quantification of parotid deformation. Accuracy evaluation was based on the comparison of parotid contours automatically propagated and contours manually traced by three experts and was aimed to demonstrate that automatic delineation was not significantly different from manual segmentation. In fact, results of our experimental protocols, which considered 10 paired of kVCT-MVCT images from 10 patients treated with IMRT, confirmed that neither parotid volume, neither DICE (DSC), COM distance, nor distance between contours (Average Symmetric Distance, ASD, and Maximum

Symmetric Distance, MSD) significantly differed between the two contouring methods (see Table A.1).

Table A.1. Analysis of contour propagation accuracy. Mean value ± standard deviation of parotid volume and COM distances are reported for each operators and the automatic method. For DSC, ASD and MSD index, mean value ± standard deviation are reported as average between operators (Op-Op) and between automatic and operators (Op-A).

	Op1	Op2	Op3	Auto
Volume [mm^3] *	16.8 ± 5.1	16.4 ± 5.0	18.2 ± 5.0	17.5 ± 5.1
COM distance [mm] **	111.4 ± 8.4	111.0 ± 8.6	110.4 ± 7.7	111.2 ± 8.0
	Op-Op		**Op-A**	
DSC ***	0.79 ± 0.04		0.77 ± 0.05	
ASD [mm] ***	1.57 ± 0.24		1.66 ± 0.34	
MSD [mm] ***	9.49 ± 1.90		9.47 ± 2.17	

* No significant differences found (Tukey test)
** No significant differences found (Anova test)
*** No significant differences found (Wilcoxon test)

The quantification of parotid deformation was carried out starting from the estimated deformation field, by calculating the Jacobian index, defined in each voxel of the image as the determinant of the gradient of the transfromation:

$$Jac(x) = det\,(\nabla\left(x_f + T\left(x_f\right)\right)$$

where, $\boldsymbol{x_f}=(x_f, y_f, z_f)$ is the fixed image domain and $T(\boldsymbol{x_f})$ is the estimated transformation. This index quantifies the shrinkage or the expansion of the single voxel; in particular: Jac=1 corresponds to a voxel that doesn't change; Jac>1 identifies an expanding voxel and Jac<1 a shrinking voxel (Davatzikos *et al* 1996, Ding *et al* 2010). The mean Jacobian index within an organ of interest (Jac_mean), calculated as the average value between all voxels belonging to this structure, is descriptive of the average deformation of the organ itself.

The structural characterization of parotid tissue was performed by the extraction of features related to the intensity patterns of the image, quantified by texture analysis. In this context, first and second order statistical indices were calculated in terms of mean gray value μ, variance σ^2, global entropy S_1, local entropy S_2 and homogeneity H; finally, fractal dimension FD was also computed. These parameters are descriptive of the complexity and organization of the image and can adequately characterized changes in parotid structure. In particular, high values of variance means an inhomogeneous image with high gray value differences, global entropy is an index of histogram uniformity: the more the value of entropy increases, the more disordered is the gray value distribution; high tissue homogeneity and high organization were featured by high values in H and low values in S_2. Fractal analysis provides a measure of the complexity and the roughness of a surface, determining the relative amounts of detail or irregularities at different scales. FD of a 2D image ranges between 2 (the topological dimension of a 2D image) and 3 (the topological dimension of a 3D volume), where larger FD indicates rougher image (Peitgen *et al* 1988).

Experimental protocols

Anatomical and structural variations in parotid glands were assessed in this project by considering different populations and different time-points. First, starting from the known volume decrease measured after RT, the correlation between Jac_mean, descriptive of the anatomical deformation of the organs, and some pre-treatment clinical and dosimetric parameters was evaluated in 168 parotid glands. kVCT or MVCT images were acquired at the beginning and at the end of therapy, depending on the type of IMRT used. A multivariate analysis (MVA) was performed between Jac_mean and clinical/dosimetric parameters, in order to find the most relevant variables related to parotid shrinkage. Moreover, parotid glands DVHs were stratified according to their degree of de-

formation, trying to assess the most predictive dose-volume combination in the low and medium dose region.

Second, a further multivariate regression analysis was carried out in the same population considering density variations between the start and the end of treatment; correlation between Jac_mean and density variation was also assessed to investigate if anatomical changes could be directly associated to functional modifications globally described by a change in the image intensity.

Then, we studied the kinetic of textural indices during the whole treatment in 37 patients (74 parotid glands), considering CT images acquired at the beginning, at the half and at the end of therapy. Differences between textural parameters and volume at each time-point were tested using t-test statistics for each index, to evaluate time trend variations. Moreover, correlations between total variations measured at the end of therapy were assessed with Pearson's coefficient.

Another important issue in studying the effect of RT on OARs is the capability of early predict those subjects that will experiment worse side effects and thus that can mostly benefit of a replanning strategy. Considering this intent, the ability of textural features in predicting parotid shrinkage measured at the end of treatment, as an index which is known to be related to the presence of acute toxicity, was preliminary investigated in 21 patients, taking into account CT images acquired in the first, second and last week of RT. Fisher's linear discriminant function analysis was applied to variations occurred in the first two weeks of RT, in order to assess the power of textural indices in predicting parotid shrinkage after treatment. A priori classification was based on the amount of total parotid volume decrease, as index of parotid shrinkage. Discriminant analysis was applied to each index and to different combinations of parameters and accuracy (Acc) of classification was estimated.

Finally, in these same 21 patients we evaluated possible correlations between the found structural variations and the clinical outcome. This aspect can help in understanding the clinical impact

of image-based analysis in head and neck RT and in finding possible patients which can better benefit of a re-planning of dose delivery during treatment, based on the prediction of RT side effects. The correlation between early parotid gland variations in the first two weeks of RT and xerostomia was investigated. A logistic uni-variate analysis was performed and a ROC curve was utilized to evaluate the predictive value of the model. Finally the probability risk of experiencing high scores of xerostomia vs early density variation was evaluated.

Results

Overlap between PTVs and parotid gland, age, mean dose on parotids and most of the DVH parameters were found as the pre-treatment variables significantly correlated with Jac_mean. MVA analysis showed that age, overlap between PTV and parotid gland and V10 were the best independent predictors of low values of Jac_mean (great parotid shrinkage). Parotid glands were divided in three different sub-groups (bad-, medium- and good-DVH) based on the DVH shape. The risk to have Jac_mean less than the first quartile of the population was 39.6% vs 19.6% vs 11.3% in these three groups. By including in the MVA analysis this “DVH grouping” parameter, age and bad-DVH was found as the most predictive parameter for large shrinkage.

A decrease in density was found in 116/168 parotids (69% of the whole population, 78% when only kVCT patients were considered). Individual density variation was highly correlated with parotid deformation both in terms of volume change and Jac_mean, and with neck thickness variation; these correlations were much stronger for kVCT data. Logistic analyses showed a two-variable model including large deformation (Jac_mean < 0.68) and initial neck thickness to be the most predictive variables ($p < 0.0005$, AUC = 0.683; AUC = 0.776 for kVCT).

Regarding the behavior of textural indices, a general decrease was measured ($\Delta\mu$=-4.7 HU and -5.3 HU, ΔS_2=-0.15 and -0.27, ΔFD=-0.02 and -0.03, ΔV=-3.5 cm^3 and -5.1 cm^3, in the first half and in the whole treatment respectively), with different time trends (see Figure A.2). T-test revealed that significant differences were present for each parameters during the whole treatment ($p<0.001$) and in the first half ($p<0.001$), while in the second half a significant variation was found for S_2, V ($p<0.001$) and FD ($p<0.01$), but no significant difference was found for μ. Strong linear correlations were found between ΔV-$\Delta\mu$, ΔV-ΔS_2 and $\Delta\mu$-ΔS_2 (see Table A.2).

Table A.2. Results of Pearson correlation analysis between variations of each parameter during the whole treatment. Pearson coefficient and significance are reported.

	ΔS_2_total	**ΔFD_total**	**ΔV_total**
$\Delta\mu$_total	0.309**	0.215	0.405**
ΔS_2_total		0.113	0.591**
ΔFD_total			-0.078

** $p<0.001$

In the prediction analysis of parotid shrinkage, when variations in the first two weeks were considered, it was found that the most powerful predictors were V and μ (Acc=66.7%), followed by FD (Acc=50%). Considering the multi-parametric analysis, the best results (Acc=71.4%) were achieved by the combinations of FD and V, and the combination of all considered indices.

Finally, a clear correlation was found between early changes of volume and density and mean xerostomia score. A significant difference for both the $\Delta\mu$ and ΔV was found when splitting the population in two groups according to the median value of the mean xerostomia score (1.57). On the contrary, no significant results were found for local entropy and fractal dimension. The group with a mean xerostomia $\geq$ 1.57 has a larger density and volume variation during the first part of treatment, while it is almost unchanged at

the end (or during the second half of treatment); on the other hand, patients with low xerostomia mean scores show almost constant values for both $\Delta\mu$ and ΔV during the entire course of treatment. Figure A.3 shows the probability risk of experiencing a mean xerostomia ≥ 1.57 versus $\Delta\mu$.

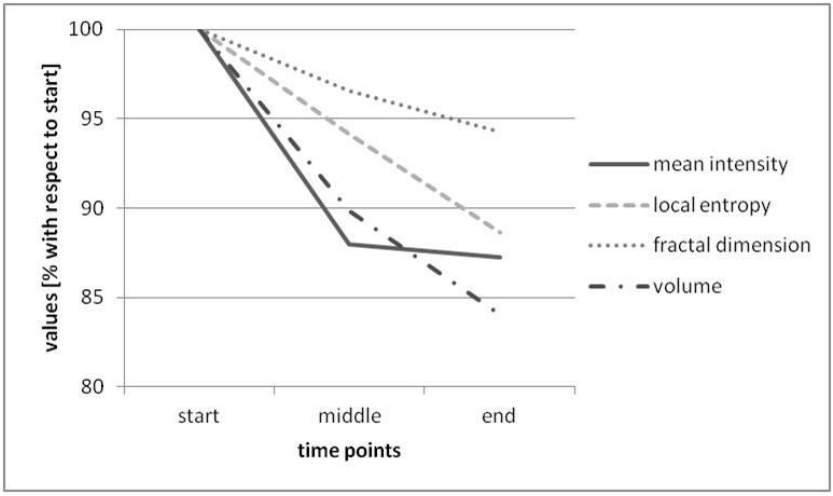

Figure A.2. Variations of mean intensity, local entropy, fractal dimension and volume during RT, considering CT images acquired at the beginning, half and end of therapy.

Conclusion

CT-based features proposed in this PhD project were deeply studied for the characterization of radiation-induced effects on parotid glands during the RT on HNC patients. We evidenced that parotid shrinkage is highly related to low dose DVH values; at the same time, density variation measured after RT is significantly correlated with volume decrease, suggesting that the loss of acinar cells and the consequent increase in the percentage of the fatty component

is related to the decrease in functionality. We proved that the major reduction in density is concentrated in the first half of the treatment, while the decrease in volume and in tissue complexity (measured by local entropy and fractal dimension) is quite constant during the whole treatment. Finally, we found that the most accurate prediction of parotid shrinkage is achieved by the combination of variation in volume, density and fractal dimension measured in the first two weeks and that the early prediction of xerostomia score was preliminary achieved by early density and volume variation. These last analyses are still an open challenge, since our dataset was too small to generalize this conclusion.

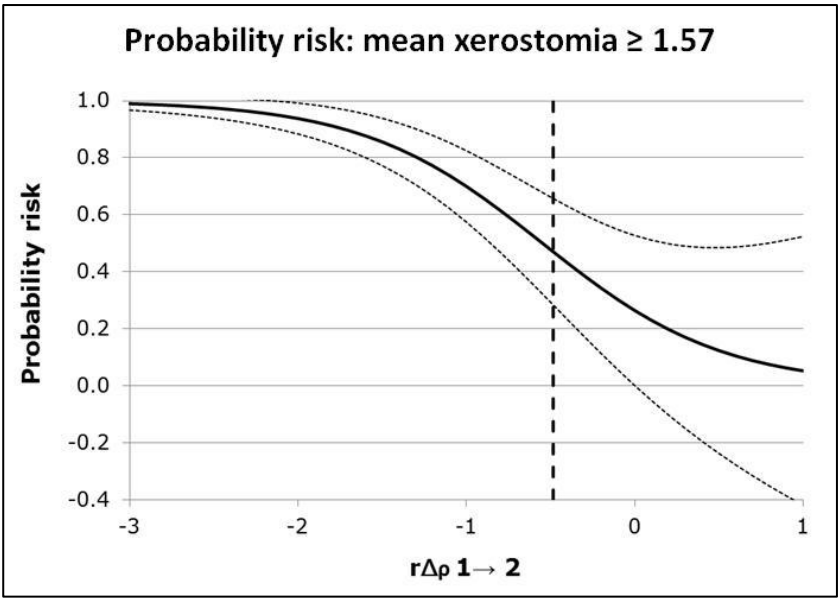

Figure A.3. Probability risk (95%CI) of mean xerostomia ≥ 1.57 (median value) vs early density variation, expressed as daily variation rate (rΔρ1→2). The dashed line indicates the best cut-off value (-0.49) of rΔρ.

Possible future works in this line of research will regard the improvement in accuracy and optimization of the registration

method and texture analysis. Moreover, results of correlations with clinical outcome should be confirmed by considering a larger dataset. For a complete evaluation of the RT treatment in the HN district, this image-based analysis should be also performed on different medical imaging acquisitions (e.g. MRI, PET), in order to have a multi-parametric characterization of parotid tissue. Finally, an extension of these methods on other OARs interested by dose delivery in HNC treatment and playing a relevant role in the quality of life of patients (e.g. organs assigned to swallowing) should be considered.

CONTENTS

LIST OF ABBREVIATIONS

ASD	Average Symmetric Distance
CBCT	Cone Beam Computed Tomography
CT	Computed Tomography
DSC	Dice Similarity Coefficient
DVH	Dose-Volume Histogram
FD	Fractal Dimension
FFD	Free Form Deformation
GTV	Gross Target Volume
H	Homogeneity
HN	Head and Neck
HNC	Head and Neck Cancer
HT	Helical Tomotherapy
HU	Hounsfield Unit
IGRT	Image Guided Radiotherapy
IMRT	Intensity Modulated Radiotherapy
Jac	Jacobian index
JVH	Jacobian Volume Histogram
KVCT	KiloVoltage CT
MI	Mutual Information
MRI	Magnetic Resonance Imaging
MSD	Maximum Symmetric Distance
MVCT	MegaVoltage CT
NMAR	Normalized Metal Artefacts Reduction
NRR	Non Rigid Registration
NTCP	Normal Tissue Complication Probability
OAR	Organ at risk
PG	Parotid Gland
PTV	Planning Target Volume
RT	Radiotherapy
S_1	Global entropy
S_2	Local entropy
US	Ultrasound

TPS-RPM	Thin Plate Spline-Robust Point Matching
μ	mean intensity
σ^2	variance

Chapter 1

Introduction

The main goal in Radiotherapy (RT) is to accurately focus radiations on tumor, sparing normal tissues, in order to damage the DNA of tumoral cells, thus blocking their proliferative properties. However, in many case, organs at risk (OARs) are partly overlapped with the planned high dose region and a complete sparing of these structures is impossible. Modern techniques, like Intensity Modulated RT (IMRT), generates steep dose gradients, providing higher conformity to target volumes with complex shapes and avoiding OARs more accurately than classical 3D conformal RT approach. Another important step in improving RT techniques was made by the availability of tomographic images acquired during the treatment, allowing the on-line correction of patient positioning errors before each RT fraction, and thus guiding the therapy (Image-Guided RT, IGRT). This new approach is able to correct global and rigid misalignments, but local anatomical deformations that occur during RT, due to physiological movements (heartbeat, breathing, visceral movements) or to the effects of therapy (weight loss, alteration in muscle mass and fat distribution), have to be taken into account.

For the treatment of head-and-neck cancer (HNC) it is important to consider this second kind of local deformations, since the weight loss and the radiation-induced effects on some critical structures have a significant impact on the quality of life of the treated patients. In particular, this PhD project was focused on the effects of

RT on parotid glands (PG), the main salivary glands, which are known to have a volume reduction and a shift toward the midline, moving from the low-dose region to the high-dose region, thus receiving a radiation dose higher than that planned. This condition has a strong impact on the health of the patient, which in many cases experiments a dry mouth and difficulties in swallowing, a pathology known as xerostomia. The analysis of images acquired during RT can help in characterizing the parotid gland tissue and in assessing the causes of these symptoms, the other possible effects of radiations on parotid glands, and the possibility of an early prediction of those patients who could be interested by severe xerostomia. In particular, this last aspect could be crucial for a potential re-planning of the delivered dose during RT, thus adapting therapy based on the patient response to the treatment (Adaptive RT, ART).

The aim of this work was thus the evaluation of morphological and structural modifications induced by RT on parotid glands using image-based indexes extracted from CT images acquired during the treatment. In particular, in this PhD project it was proposed to estimate morphological changes by the deformation of the glands, evaluated by applying a non-rigid registration method expressly optimized and validated on CT images of the HN district. Secondly, a method of image analysis based on textural feature extraction was proposed to characterize structural variations of parotid tissue. All these methods were evaluated and optimized for the clinical problem and all these parameters were studied in relation to dosimetric and clinical indexes and to the clinical outcome, in order to better assess their contribution in this research field.

The work was developed at the Istituto di Bioimmagini e Fisiologia Molecolare - Consiglio Nazionale delle Ricerche (IBFM-CNR) of Milan (Italy) in collaboration with the Medical Physics Department of San Raffaele Hospital, and involved a multidisciplinary group of engineers, medical physicists and radiotherapists.

The thesis is so developed: in Chapter 2 a description of the anatomy, physiology, radiosensitivity and common imaging of parotid glands is reported, followed by an overview of the state of art

of image-based analysis of radiation-induced effects on parotid glands. In Chapter 3 and 4 the proposed and developed image analysis method is described. In particular, in Chapter 3 the extraction of morphological indexes is presented: the first part of the chapter is focused on the image registration method and its validation on our dataset, while the second part treats the quantification of parotid glands deformation directly derived from the deformation field estimated by image registration. In Chapter 4 the structural analysis based on texture analysis is described: here a method for the correction of metal artifacts in CT images is proposed and textural features are widely faced. Moreover, correlations between image-based indexes and dosimetric and clinical parameters are studied; an initial analysis with clinical outcome is also performed. Finally, in Chapter 5 discussion of all the reported results is presented with further research possibilities to continue this project line.

Chapter 2

Parotid glands as organs at risk in radiotherapy

2.1. DESCRIPTION OF PAROTID GLANDS ANATOMY, PHYSIOLOGY, RADIOSENSITIVITY AND IMAGING

Salivary glands play an important role in oral health and their normal functionality is essential to maintain a good quality of life in patients. The major salivary glands consist of paired parotids, submandibular and sublingual glands, that work in concert with many other minor salivary glands for the saliva production, aiding in food digestion, protecting oral mucosa, facilitating remineralization of dental hard tissues and moistening the palate for articulation (Grundmann *et al* 2009). In this section, an essential overview of the normal anatomy, functionality and radiosensitivity of parotid glands is reported, followed by a list of the classical imaging modalities employed in clinical practice.

2.1.1. Anatomy

Parotids are the largest salivary glands and are located in the space that extends (see Figure 2.1, 2.2) (Bridge and Tipper 2011):

- posteriorly from the pinna to the anterior borders adjacent to and occasionally over the masseter muscle;
- inferiorly beyond the angle of the mandible to the platysma muscle;
- medially adjacent to the fatty parapharyngeal space.

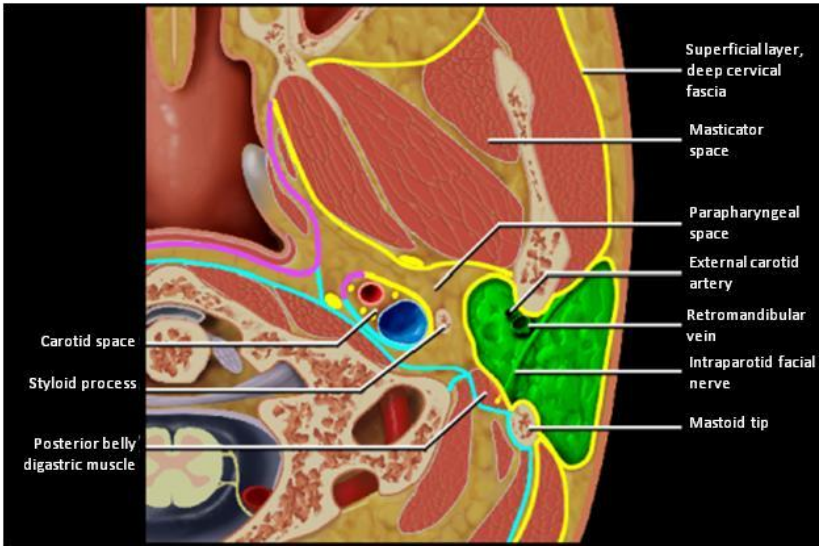

Figure 2.1. Axial graphic of the parotid space (PS) at the level of C1 vertebral body. The PS contains from medial to lateral the external carotid artery, retromandibular vein and facial nerve. The intraparotid Cranial Nerve (CN7) creates a surgical plane that divides the gland into superficial and deep lobes. PS is enclosed by the superficial layer of the deep cervical fascia. Figure from Amirsys reference centers.

Parotid glands can be partitioned into deep and superficial lobe; despite this definition, there is actually no anatomic separation between these portions. By convention, parotid tissue situated deep to the facial nerve is referred as the deep lobe, while parotid tissue superficial to this plane is considered to be the superficial

lobe (Som and Brandwein-Gensler 2011). Another possible division of parotid portions can be done with respect to the mandible: parotid tissue external to the mandible is referred to as superficial, whereas the smaller amount of parotid tissue that resides behind and deep to the mandible is referred to as the retromandibular or deep portion of the parotid gland.

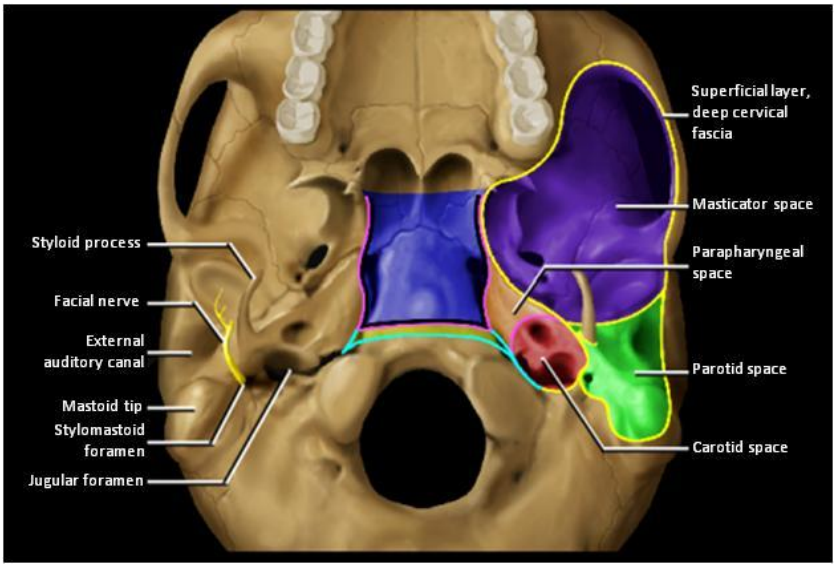

Figure 2.2. Axial graphic of skull base viewed from below illustrating the interaction between the parotid space and the skull base. CN7 exits through the stylomastoid foramen at the skull base, just posterior to the styloid process and lateral to the jugular foramen. The PS is the most lateral space in the nasopharyngeal and oropharyngeal area, extending from the external auditory canal above to the level of the mandibular angle below. Figure from Amirsys reference centers.

Each salivary gland consists of acinus, myoepithelial cells, and ducts, organized as a tree-like branching pattern in intercalated, striated and excretory duct (see Figure 2.3). All salivary acinar cells contain secretory granules: in adult parotid glands, the acini are

purely serous (protein-secreting), while in other glands (e.g. submandibular) serous acini are mixed with mucous acini (mucin-secreting). The fat component is characteristic in parotids with respect to other salivary glands: in fact, the adipocyte to acinar cell ratio is 1:1 and this ratio tends to increase with age.

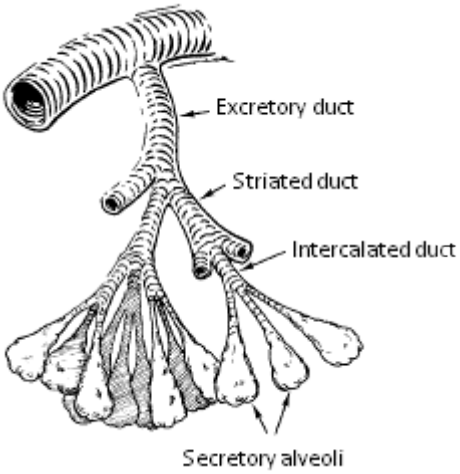

Figure 2.3. The tree-like branching structure of parotid ducts. Figure from (Som and Brandwein-Gensler 2011)

From histological images, terminal secretory portions (adenomeres) are clearly visible with their acinous or alveolar shape, containing cubic or pyramidal exocrine cells, with spherical nuclei and secretory vesicles in the cytoplasm, and with contractile myoepithelial cells surrounding acini. Each acinar cell is drained by intercalated ducts, which drain in striated ducts, whose cells are specialized in concentrating secretory products (Figure 2.4).

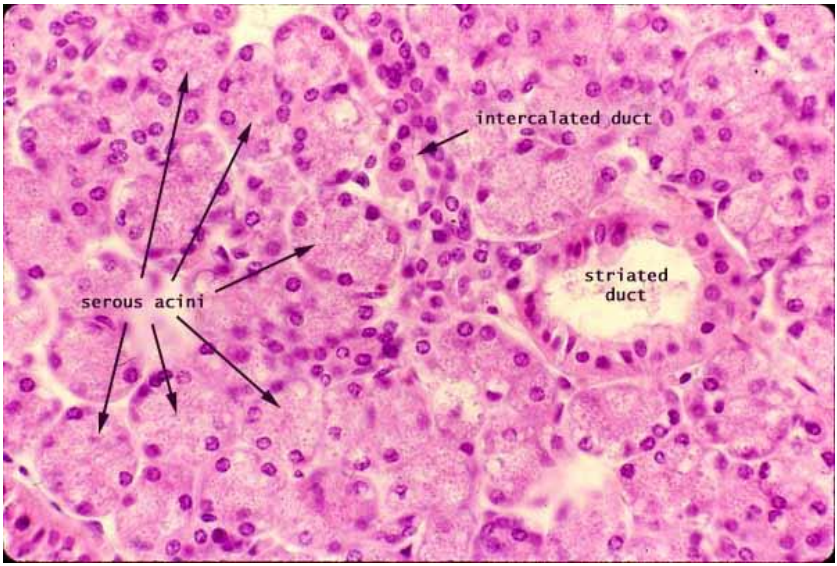

Figure 2.4. Example of histological image of parotid tissue, in which serous acini, intercalated duct and striated duct are clearly visible (figure from www.pathologyoutlines.com).

2.1.2. Physiology

Salivation is physiologically controlled by the parasympathetic nervous system; the interruption of parasympathetic innervation to the salivary glands results in atrophy, while the interruption of the sympathetic results in no significant changes (Som and Brandwein-Gensler 2011). The stimulation by the parasympathetic nervous system produces an abundant, watery saliva with a decrease in amylase concentration in saliva and an increase in amylase concentration in the serum. On the other hand, the stimulation by the sympathetic nervous system produces a scant, viscous saliva rich in organic and inorganic solutes with an increase in amylase concentration in the saliva and no change in the amylase concentration in the serum.

Normal saliva is composed predominantly of water (99.5%) and parotids contribute about the 45% of the total secretion. The secretion of electrolytes into saliva is under parasympathetic con-

trol via acinar cholinergic receptors, whose stimulation activates the transport of sodium, which enters along the basal cell membrane following an electrochemical gradient. The result of this process is the formation of an isotonic, high-sodium, low-potassium fluid. The saliva becomes hypotonic as sodium is reabsorbed and potassium is excreted in the striated ducts (Mason and Chisholm 1975).

Saliva's functions are multiple: it protects mucosa from the harmful effects of microbial toxins, noxious stimuli, and minor trauma. The salivary mucins are glycoproteins, which act as lubricants. Although the minor salivary and sublingual glands produce 10% of the total saliva volume, they secrete the majority of the mucinous components of saliva, and functional compromise of these glands (e.g., by autoimmune disease or irradiation) results in xerostomia. The antibacterial activity of saliva is accomplished by secretory IgA (Immunoglobulin A), plus enzymes such as lysozyme, peroxidase, alpha-amylase, and lactoferrin and ions such as thiocyanate and hydrogen (Mason and Chisholm 1975).

2.1.3. Radiosensitivity

Since parotid glands are normal tissue interested by dose delivery in RT, it is essential the knowledge about the radiosensitivity of these organs, in order to understand their behavior in response to radiation.

Salivary glands are extremely sensitive to radiation, yet, unlike classically radiosensitive tissues, they proliferate slowly and are made up of highly differentiated cells. In fact, a high radiosensitivity is generally a characteristic of undifferentiated cells. Early and late effects of radiation generally correlate with a tissue's rate of proliferation. Early (acute) effects occur within few days or weeks of irradiation, due to high levels of cell death. Late effects occur months or years after irradiation and may be affected by vascular damage and loss of parenchymal cells (Grundmann *et al* 2009).

In the acute phase the loss of acinar cells occurs with a glandular shrinkage (Robar *et al* 2007), which affects the composition and volume of saliva (Dirix *et al* 2006). The acute reduction in saliva

flow and changes in saliva composition have been attributed to an impairment of the gland tissue to produce sufficient saliva volume, as well as to reduced secretion of certain components of normal saliva (Makkonen *et al* 1986). Chronic radiation-induced effects may be caused by acute damage, as reported in many studies (Stephens *et al* 1986, Li *et al* 2007): also in this case, patients show a significant decrease in saliva flow for several months or years after the end of the RT. It is reported that in some cases, parotids that have received lower dose (< 25 Gy) can recover the salivary function within 12-24 months (Dirix *et al* 2006, Li *et al* 2007). However, in many subjects a permanent salivary gland hypofunction occurs, which has been attributed to attrition of acinar cells followed by replacement with fibrotic tissue (Radfar and Sirois 2003).

The possible mechanism of damage of salivary glands after RT was studied by Konings et al (Konings *et al* 2005), who observed that saliva-producing cells do not disappear but lose their function during the first days after irradiation. Two separate mechanisms to explain this dysfunction are proposed. First, there is a defect in cellular functioning because of selective membrane damage, confounding the receptor-mediated signaling pathways of water excretion. No immediate cell death or lysis takes place. Late damage is explained by classical cell killing of progenitor cells and stem cells, thus inhibiting proper cell renewal, and by damage to the cellular environment, causing a shortage of properly functioning secretory cells. This two mechanisms are clearly visible during the kinetics of damage expression, described in 4 different phases, after the irradiation with 15 Gy:

1. Phase I (0-10 days), acute phase of radiation damage. Water excretion is quickly impaired to about 60% of the normal condition, while no cell loss is observed and the amylase secretion is not affected (Figure 2.5, top).
2. Phase II (10-60 days). The compromised acinar cells, suffering damage to the plasma membrane, disappear and, at the same rate so does the secretion of amylase (Figure 2.5, bottom).

3. Phase III (60-120 days). No major changes are observed with respect of phase II in terms of secretion and cells number (Figure 2.5, bottom).
4. Phase IV (120-240 days), late phase of radiation damage. This phase is marked by a lack of functional acinar cells, caused by the killing of progenitor and stem cells. Generation of new acinar cells takes place in this period, but flow rate and amylase production are deteriorated (Figure 2.5, bottom).

In a successive study of the same authors (Konings *et al* 2006) it was evidenced that parotid glands have a different response to radiation with respect to the irradiated portion. In fact, from a histopathologic study of the rat, it has been seen that the irradiation of the cranial half resulted in a positive volume effect for late tissue injury because function loss was more than proportional to the irradiate volume. These volume effects are caused by late development of secondary radiation damage in a nonexposed region of the parotid gland. The most probable first step (primary radiation event) in the development of this secondary damage is radiation exposure to the hilus region (located between the ventral and dorsal lobe). By injuring major excretory ducts and supply routes for blood and nerves in this area, the facility system necessary for proper functioning of the nonexposed lateral lobe is seriously affected.

Typical imaging modalities employed to image salivary glands are ultrasounds (US), computed tomography (CT) and magnetic resonance (MR) images, depending on the pathology to be assessed. CT and US are the modalities chosen for patients interested by inflammatory disease and calcifications, while MR is generally useful to identify and characterize parotid's pathology before surgery.

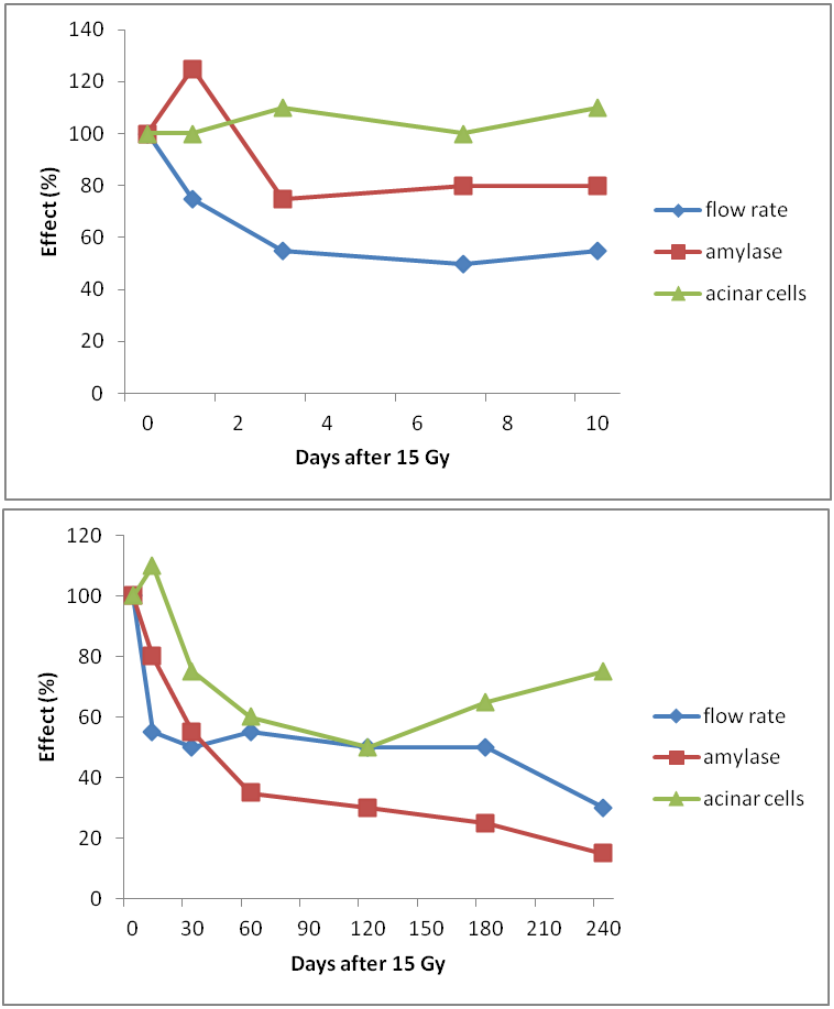

Figure 2.5. kinetics of parotid glands damage in terms of flow rate, amylase and acinar cells number. On the top: acute phase (0-10 days); on the bottom: whole period (0-240 days). Figure modified from (Konings *et al* 2005)**.**

2.1.4. Imaging modalities

2.1.4.1. CT imaging

Normal salivary glands are visualized on CT images as a relatively fatty structure with numerous thin interstitial strands interlacing throughout it; the resulting classical CT attenuation is around 15-25 HU, lower than that of the muscles but greater than that of fat. The fine anatomy of the intraglandular ducts is not normally visualized on CT images, but it is possible to individuate the retromandibular vein and the external carotid artery. In Figure 2.6 an example of CT images at different axial planes of the parotid gland is presented.

Figure 2.6. Example of CT scan of the parotid region (white arrow). Left: axial view; centre: coronal plane; right: sagittal plane. The crosshair indicates the same point in the 3 views. Figure from Amirsys reference centers.

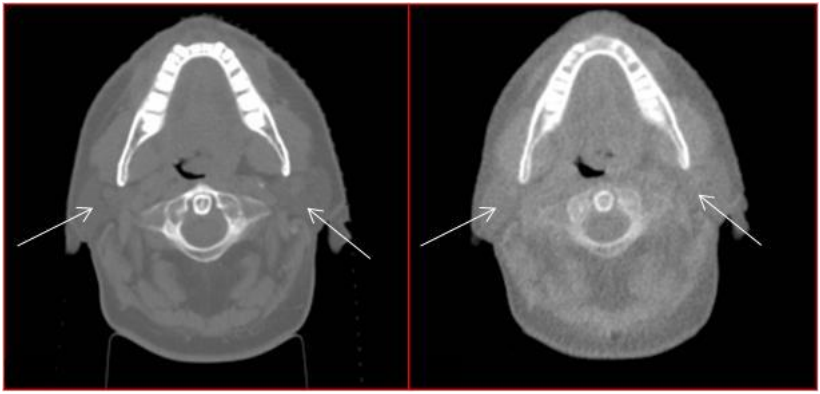

Figure 2.7. Example of kVCT (left) and MVCT (right) of the same patient. Parotid glands, indicated by the white arrows, are well visible in kVCT image, but hardly identifiable in MVCT image.

CT scan is the modality of choice in RT protocols, since the treatment planning is based on the information about the x-ray attenuation provided for each voxel. Moreover, a diagnostic kilo-Voltage CT (kVCT) is always acquired before the treatment to plan the dose map that has to be delivered to the patient, based on the contours of OARs and target delineated and on the dose that should be delivered to this structures. The new frontier of RT is based on the use of images for the optimization of the treatment, in terms of significant reduction of errors due to patient repositioning. Depending on the type of treatment chosen, the images acquired during treatment for this purpose can be of different type and quality: kVCT with high resolution and good contrast can be replaced by different x-ray tomographies, with worse contrast and quality, but delivering less dose and in the same energy range used for treatment. Mega-Voltage CT (MVCT) images are an example of these, characterized by higher noise level and lower soft-tissue contrast with respect to kVCT, due to their high energy, since they are generally used only for repositioning through bone matching. On MVCT images parotid glands are hardly identified, but it is still possible to ob-

tain some quantitative information, in terms of parotid volume and deformation, useful in assessing radiation-induced effects on these glands. In Figure 2.7 it is possible to appreciate the difference in image quality and noise of kVCT and MVCT acquisition of the same patient.

The major problem with CT imaging is the presence of metal artifacts due to dental filling (see Figure 2.8), that worsens the quality of the image, making difficult the contouring of parotid glands even for radiologic experts and affecting the quantitative information within the image. A possible solution to this limitation is the application of a method able to reduce these artifacts; more information about it can be found in Chapter 3.1.

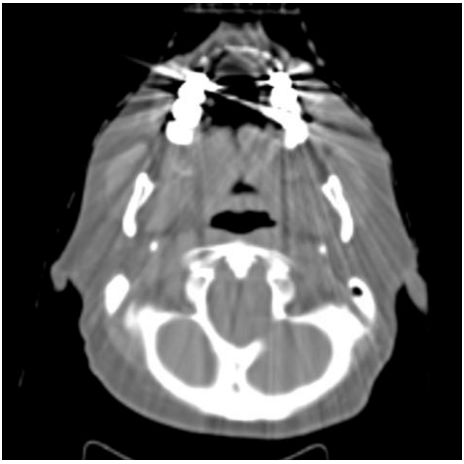

Figure 2.8. Example of CT image with metal artifacts due to dental filling. It is evident that the quality of the image is worsened and the identification of parotid glands becomes very difficult.

2.1.4.2. MR imaging

The poor contrast between soft tissue, typical of CT scans, limits the ability of identify the microanatomy of the glands, that can be better assessed using a different acquisition technique, like

the ultrasound, or, preferably, the magnetic resonance imaging. The T1-weighted signal intensity of the gland is nonhomogeneous, with multiple irregular areas of lower signal intensity that represent interstitial tissues, salivary ducts, and possibly branches of the facial nerve. The major vessels are identified by their flow voids and the facial nerve and the intraparotid ducts can be identified on MR imaging. The parotid gland showed intermediate signal intensity and the fat spaces showed high signal intensity (Figure 2.9, top row). The vessels had variable signal intensity, depending on the saturation. The nerves, muscles, ducts, and saliva had lower signal intensity. On fast spin-echo T2-weighted images the gland maintains an intermediate to high signal intensity reflecting both its fat content and the gland's water content (Figure 2.9, bottom row). Generally, both T1-weighted and T2-weighted sequences are acquired to better assess the pathology of salivary glands (Som and Brandwein-Gensler 2011).

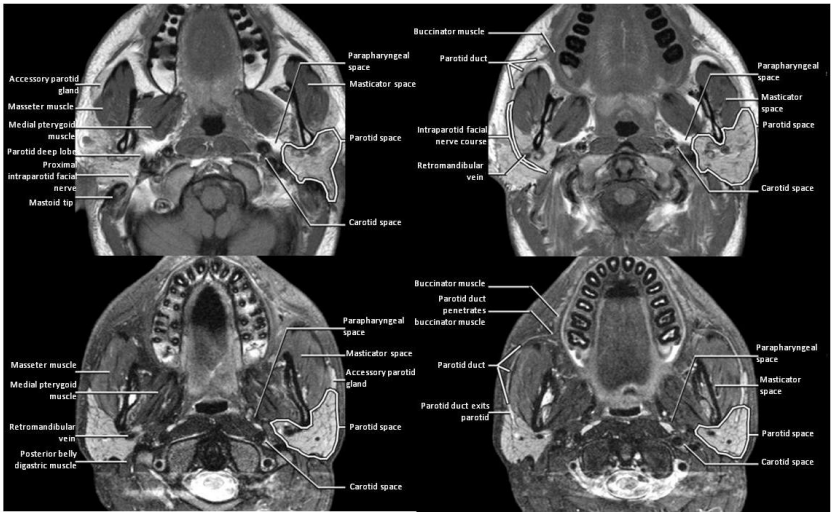

Figure 2.9. Example of MR T1-wighted (top row) and MR T2-weighted (bottom row) scan of the parotid region, at different axial planes. Figure from Amirsys reference centers.

2.1.4.3. US imaging

US has traditionally been used to differentiate solid and cystic salivary gland masses and to identify salivary calculi. Normal parotid glands present a homogeneous and highly reflective echostructure, with a large number of echoes, regularly placed all over the glandular space (Figure 2.10, left). After irradiation, the echo-pattern of the glands become heterogeneous due to the presence of nonuniform US reflective interfaces from the disorganized acinar cells arrangement after parenchymal loss and cell atrophy (Yang *et al* 2012) (Figure 2.10, right).

Usually, the US examination is performed with a linear probe, high frequency (7-10 MHz) transducer. This gives higher resolution images but does not penetrate as deeply as the lower-MHz transducer. This limitation is one of the reason that US is not utilized as frequently as CT or MR imaging to examine patients with possible deep extensions of their salivary lesions (Som and Brandwein-Gensler 2011).

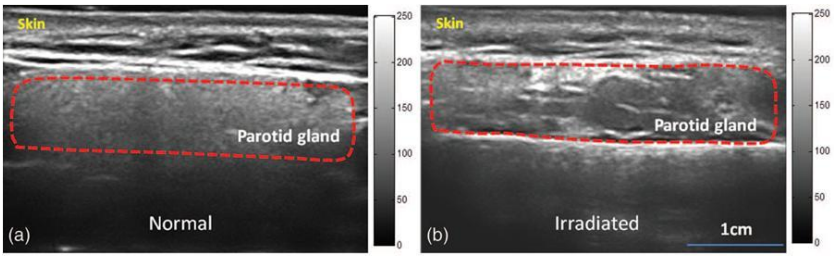

Figure 2.10. Example of US study of a normal (left) and irradiated (right) parotid gland, in which is evident the more heterogeneous echo-pattern induced by radiation. Figure from (Yang *et al* 2012)

In this work, image-based assessment of the effects induced on parotid glands by RT is performed on kVCT and MVCT images, widely available when radiation treatment is required.

2.2. IMAGE-BASED ANALYSIS OF RADIATION-INDUCED EFFECTS ON PAROTID GLANDS: STATE OF ART

The study of RT effects on salivary glands was widely faced by a large number of groups, since acute and late toxicity can severely affect the quality of life of patients. Therefore, it is important to assess the possible causes of salivary glands toxicity, related to the clinical and dosimetric parameters registered and imposed before RT and to the possible effects of radiations. Moreover, each subject has a different radiosensistive behavior and an early identification of those patients that could experiment the worst consequences is of great interest. The availability of tomographic images acquired during and after the treatment has significantly improved the accuracy of these studies and the extraction of image-based indexes has become a valid support in evaluating RT effects.

The first and more evident effect of RT on parotid glands is the shrinkage of these glands and a shift towards the midline and the high dose region (Barker Jr *et al* 2004, Hansen *et al* 2006, Robar *et al* 2007, Broggi *et al* 2010, Bhide *et al* 2010). This aspect was deeply assessed by Vasquez Osorio et al (Vásquez Osorio *et al* 2008), who proposed an image registration framework in order to estimate local shape and position variations in parotids. In this study, parotid and submandibular glands were classified in two groups (irradiated and spared glands) in order to assess if the mean dose delivered on these organs has an impact on the volume changes measured after the whole treatment. They found an average volume reduction for both groups of 14%, but an asymmetric shift, more evident for irradiated glands than for the spared. Moreover, they performed a local estimation of shape and position changes, by dividing parotids in six regions (superior, inferior, anterior, posterior, right and left), finding different displacements depending on the anatomical position. In particular, they found an average shift of 1 ± 3 mm and 3 ± 3 mm for the medial and lateral regions of the irradi-

ated glands, respectively (Figure 2.11 summarizes their results). They concluded that for irradiated glands, the lateral regions, with the lower planning doses, displace inward, toward the higher doses, while spared parotids present little and near homogeneous deformation.

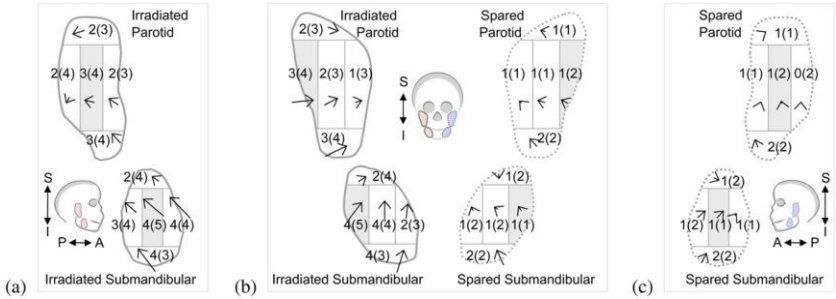

Figure 2.11. 3D lengths of average 3D vectors and standard deviations for each region in millimeters. Arrows show projection of average 3D deformation vectors in (a) right, (b) frontal, and (c) left views. Solid lines represent irradiated glands; dashed lines represent spared glands. External lateral walls of glands represented with gray shadows. Figure from (Vásquez Osorio *et al* 2008)**.**

The kinetic of parotid volume variation was studied by different groups (Bhide *et al* 2010, Tomitaka *et al* 2011, Fiorentino *et al* 2012), taking into account CT images acquired at different time points during and after RT. Bhide et al (Bhide *et al* 2010) studied the evolution of parotid volume in 20 patients during RT considering CT scans acquired before treatment and at weeks 2, 3, 4 and 5 during RT. The greatest reduction (14.7%) was found in the first two weeks of RT, and shrinkage was more evident in ipsi-lateral glands than in contro-lateral, though this difference was not significant. Another group (Fiorentino *et al* 2012) studied the kinetic of parotid volume in 10 patients during treatment, considering Cone-Beam CT (CBCT) daily acquired, for an average value of 14 scans for each patient. They found a linear trend in the volume decrease (r^2 of linear re-

gression=0.91), with a variation rate of 1.6% and 1.8% for ipsi- and contro-lateral parotid glands, respectively. In the third week of RT both parotid glands had shrunk of 30% of the original volume, and for this reason the authors suggest that a check of parotid volume or a re-planning at this time point could be indicated. A wider research, taking into account a larger period, was dealt in (Tomitaka *et al* 2011), where the authors considered CT images acquired before RT and 2 weeks and 6-12-24 months after 30 Gy irradiation to evaluate volume modifications in ipsi- and contro-lateral parotid glands. Their major finding about morphological changes was that parotid volume experimented a maximum shrinkage 6 months after RT, consistent with the other studies, but it gradually recuperated in the course of the subsequent 2 years.

This volume variation was also correlated with the dose distribution and dose changes during treatment. One of the first work that has studied volume and dosimetric changes in different structures using CT images at the beginning and at the end of IMRT reported a overdosage on parotid glands due to the shift toward the higher dose region (Hansen *et al* 2006). Similarly, in (Bhide *et al* 2010) an increase in the mean dose was found in the last two weeks, with respect to that planned: this is due to the medial shift of parotid glands started in the second week and to the shrinkage of the target. A high correlation ($p<0.001$, $r=0.68$) between the decrease in parotid volume and the planned mean parotid dose was found in (Vásquez Osorio *et al* 2008). Similar results were obtained by (Broggi *et al* 2010), where a two-variable linear model of parotid shrinkage was proposed. Performing a multi-variate analysis with clinical and dosimetric variables and considering volume variation at the end of RT as end-point, the authors suggested that the main predictors of absolute parotid shrinkage were the initial parotid volume and the mean dose, described by the equation:

$$\Delta Vcc = -2.44 - 0.076\, Dmean\ (Gy) + 0.279\, IVP\ (cc)$$

where ΔVcc is the volume variation in cc, $Dmean$ is the mean parotid dose at planning and IVP is the initial parotid volume, indicating that larger glands may experiment larger volume variations. When

the percentage of volume variation was considered, the main predictors were age and V40 DVH, suggesting that acute radiation-induced function loss of salivary glands could be more active in younger patients.

Knowing this relationship between volume decrease and dose received by parotid glands, the next step is the assessment of correlations with the degree of xerostomia, the more expected toxicity in acute and late phase after RT. Many works have underlined the dose-function relationship in parotids, trying to understand which is the contribution of dose-volume histogram in the progress of xerostomia. One the first study about this subject (Eisbruch *et al* 2001) discussed the importance of sparing parotid glands, reducing the severity of xerostomia over time: this is a benefit gained by IMRT with respect to the classical 3D standard RT. Jellema et al (Jellema *et al* 2005) , in accord to the other work, studied the effect of mean dose on parotid and submandibular glands on xerostomia over time. 6 months after RT xerostomia was more severe in patients with high mean dose both on parotids and submandibular glands, but after 12 months it was partially reversible, depending of the dose on these glands. It was reported by Deasy et al (Deasy *et al* 2010) that the risk of xerostomia is minimum if at least one parotid gland is spared to a mean dose of less than 20 Gy or if both glands are spared to less than 25 Gy. Loss of functionality of salivary glands was studied by Bussels et al (Bussels *et al* 2004) with SPECT imaging: their results suggested that after a low dose (10-15 Gy) there can be a serious loss of function. Moreover, they found that the dose resulting in 50% loss of excretion fraction 7 months after RT is 22.5 Gy. In a recent work (Beetz *et al* 2012), a NTCP (Normal Tissue Complication Probability) model was developed to study the significance of the radiation dose in the major and minor salivary glands of 167 patients treated with 3D conformal RT, and other pre-treatment and treatment factors, with regard to the development of xerostomia. With a multivariate analysis they found that the risk of developing xerostomia increased with age and was higher when minor baseline

xerostomia was present in comparison with patients without any xerostomia complaints at baseline.

Resuming these considerations, the reported parotid shrinkage was found to be correlated with the mean parotid dose and also the risk of xerostomia was demonstrated to be strictly related to the dose-volume histogram. Although there are a very limited number of studies reporting a direct influence of parotid volume decrease in the development of xerostomia in human (Teshima *et al* 2010), it is clear that a relationship between these two conditions exists. In particular, in this study (Teshima *et al* 2010), morphological changes of twenty patients treated with chemo-RT were evaluated using CT or MRI images acquired before and after RT; salivary function was evaluated before and after the treatment in terms of saliva production. After 30 Gy irradiation, both saliva production and parotid volume were significantly decreased; moreover, the parotid volume ratio was found to be inversely correlated with the saliva reduction amount ($r=-0.79$, $p<0.01$). The authors suggested that the volume reduction measured from CT/MRI images can be used as a predictive index of the decreased parotid gland function.

Recently, new studies were focused on new image-based indexes able to describe radiation-induced damage on parotid glands. In particular, more attention is given to the analysis of density variation estimated from intensity values in CT images. In fact, since CT values are linearly correlated with tissue density through the absorption coefficient, it is easy to extract a parameter which may represent functional behavior of the considered region. Therefore, changes in the composition of parotid gland tissue, i.e. the ratio between acinar cells and fat component, can be assessed by the variation of CT number. Teshima et al (Teshima *et al* 2012) published a work in which correlations between CT values variations and histopathological changes were assessed to evaluate the robustness of CT intensity in reflecting salivary function. They retrospectively evaluated the relationship between CT and histopathological findings of parotid and submandibular glands in six patients treated for advanced oral cancer, with preoperative chemoradiation therapy

(CRT) with a total dose of 30 Gy and oral S-1 (80 mg/m^2/day) and CT and histopathological images available. From CT images, they found a decrease in parotid volume and in CT number after 30 Gy irradiation; these results were confirmed in histopathological images by the loss of acinar cells and by the inverse correlation of CT values with adipose ratio ($r=-0.98$, $p<0.01$). These results suggest that acinar cell loss is a main contributor to changes in the volume and function of irradiated human parotid and submandibular glands and that CT value may reflect the adipose ratio rather than salivary function.

Another very recent work (Obinata *et al* 2013) evaluated morphological and functional changes in parotid glands of six patients after IMRT by the estimation of parotid volume and CT number before and after treatment. According to previous studies, they found a decrease in parotid volume (39.4 % and 26.5 % for ipsilateral and contralateral parotidds, respectively) and CT number (13.8 HU and 5.4 HU for ipsilateral and contralateral parotids, respectively). They also estimated the saliva production using Saxon test and correlated the reduced functionality of the glands with the decrease in volume and density. No significant correlation was identified with volume variation, probably due to the small sample size, but a strong correlation ($r=0.84$, $p<0.01$) was found between CT number and salivation. In accord with (Teshima *et al* 2012), they speculated that the CT number reduction after RT may have resulted from acinar atrophy, parenchymal loss, and fatty replacement. However, a consideration should be taken into account, as reported in (Rabin *et al* 1996): in some cases it is possible to individuate an increased attenuation which could be a result of increases in water content caused by edema of the inflamed parotid gland, in patients affected by sialadenitis.

Supporting this last consideration, a recent work (Houweling *et al* 2011), assessing early radiation-induced changes in salivary glands of 18 patients using anatomical MRI and DCE-MRI images, found a decrease in T1w signal of 10% and an increase in T2w signal of 25%. These results indicated an elevated water content, while

both the increase in ν_e and the decrease in k_{ep} (indexes related to DCE-MRI) suggested an increase in the extra-cellular extra-vascular space. These parameters can be related to the same underlying mechanism, vascular edema. Despite the edema, the gland volume reduced by 25%. The volume reduction of the glands was implying cell loss as an early effect, that have been proposed as the main effects of salivary gland dysfunction in previous studies (Konings *et al* 2006, Feng *et al* 2009).

High-resolution MRI (HR-MRI) was used in another work (Kan *et al* 2010) in order to evaluate morphological changes in the internal architecture of salivary glands induced by RT. The advantage of using HR-MRI (resolution=0.31 mm/pixel) is the possibility of providing precise information about the internal architecture of the gland, and in particular of the main excretory duct, without any invasiveness. The quantitative analysis performed by the authors on 12 patients showed that the width of the main duct is reduced and the intensity ratio of the main duct lumen is significantly decreased after RT. The signal intensity of the duct lumen reflects the salivary content and is considered to offer a measure for the evaluation of functional changes caused by RT.

Finally, sonographic images were also employed to evaluate the effects of RT on parotid glands (Yang *et al* 2012). Notwithstanding the type of image is very different from CT and MRI, it is worthy to mention this work, since its conclusions are consistent with all the other studies. US images were acquired in 7 healthy volunteers and after RT in 12 patients and then analyzed using texture analysis. Significant differences were found in textural features between healthy and post-RT subjects: normal parotid glands exhibited homogeneous texture, while the postradiotherapy parotid glands exhibited heterogeneous echotexture. This heterogeneous echopattern of post-RT parotid gland is likely due to the presence of nonuniform ultrasound reflective interfaces from the disorganized acinar cell arrangement after parenchymal loss and acinar atrophy.

Chapter 3

Extraction of morphological indexes

3.1. IMAGE REGISTRATION AND CONTOUR PROPAGATION METHOD

3.1.1. Typical image registration methods in Radiotherapy

Image registration is the process of finding a geometric transformation between two respective image-based coordinate systems that maps a point in the first image set to the point in the second set that has the same patient-based coordinate, i.e. represents the same anatomic location (Mattes *et al* 2003). The estimated geometric transformation finds a voxel-by-voxel correspondence between a fixed image *f* and a moving image *m*:

$$T(x, y, z): (x, y, z) \in \Omega_f \longrightarrow (X, Y, Z) \in \Omega_m$$

The image registration methods can be divided in two main groups, depending if the estimated spatial transformation is rigid, thus preserving distances between all points in the image, or non-rigid (NRR). Rigid registration allows only translations and rotations to align the images, and it can be used for a global transformation, such as for patient repositioning during a treatment, for multi-

modal image integration of non deformable districts (for example, the integration of CT and PET brain images) or for the initialization step in the NRR approach.

However, since human body cannot be seen as rigid body and misalignments at local scale can occur, NRR techniques are introduced for the correction of the elastic deformations that may happen due to physiological motions or anatomical changes. In literature, a great number of different NRR methods are reported, based on different information type used for the estimation of transformation.

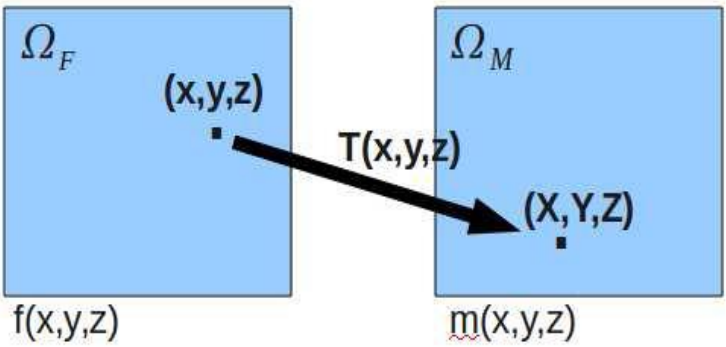

Figure 3.1. Image registration definition

Some approaches use specific features in the images (anatomical landmarks, implanted landmarks or delineated organs) which have to be realigned to find the best correspondence between the two images. One of the most applied method in RT is the thin plate spline - robust point matching (TPS-RPM), firstly proposed by Chui and Rangarajan (Chui and Rangarajan 2003) and improved by Bondar (Bondar *et al* 2010).This method iteratively estimates point correspondence between two sets of contour points of organs of interest, and updates a non-rigid transformation modeled by a thin-plate spline. The main advantage of this algorithm is the inde-

pendence of the registration accuracy from the image quality, from low contrast between structures or from the presence of artifacts. However, accuracy is controlled only on the neighborhood of the control points; moreover, modeling deformations using thin plate spline can be a disadvantage because it limits the ability to model complex and localized deformations, since a perturbation on a single point has influence on all the others. In RT applications, TPS-RPM has been employed in several contexts, for example to evaluate anatomical changes in head and neck cancer patients (Vásquez Osorio *et al* 2008), for the estimation of the dose actually delivered on tumor when two treatment modalities are combined (Vásquez Osorio *et al* 2011) and to automatically segment vessels in the liver (Vasquez-Osorio *et al* 2012).

The other main approach in NRR methods is represented by the intensity-based registration algorithms, which use only image intensity information to recover the spatial transformation connecting the images consequently being more automatic and less costly but more sensitive to image noise or intensity mismatching. Most used methods belonging to this category are optical-flow (Horn and Schunck 1981), Thirion's Demons algorithm (Thirion 1998) and B-spline free-form registration (Rueckert *et al* 1999).

Fluid registration, also known as optical flow (OF), methods consider that the differences between target and source images could be described as motion of voxels based on the OF equation, and, given two images, they find voxels correspondence by computing a displacement field describing the apparent motion represented by matching the intensity gradients in the two images. Different algorithms are proposed in literature to solve the OF equation, each of them was characterized by an additional set of equations introducing some constraints and conditions for estimating the actual flow (Horn and Schunck 1981, Lucas and Kanade 1981, Bruhn *et al* 2003). Thirion's Demons algorithm was inspired by the OF equation, but instead of having a flow field in the entire image, the forces are applied in the borders of the objects inside the images, introducing demons that push according to local characteristics of the images.

Demons algorithm is generally more accurate than OF methods, but it requires a great deal of computation time. The main drawback of these fluid registration methods is the limitation on mono-modal registration, since they are constrained by the assumption of intensity conservation between images. Thanks to their accuracy, Demons algorithms, and their novel improved implementations providing diffeomorphic registration (Vercauteren *et al* 2009, Janssens *et al* 2009), are widely employed in RT mono-modal applications; for example, they found their natural use in 4DCT thoracic images, to model breathing movement in lungs and GTV (Boldea *et al* 2003, Zhang *et al* 2008, Østergaard Noe *et al* 2008, Castillo *et al* 2009, Janssens *et al* 2011). In addition, Demons algorithm was used also to estimate daily prostate deformations (Wang *et al* 2005) and anatomical changes in head and neck patients (Wang *et al* 2005) during RT treatment for dose tracking, and to automatically delineate organs in adaptive head and neck RT (Hardcastle *et al* 2012).

In this thesis, the NRR method used to evaluate anatomical deformations of parotid glands is the free-form deformation (FFD) based on B-Spline (Rueckert *et al* 1999). The basic idea of FFD is to deform an object by manipulating an underlying mesh of control points (Sederberg and Parry 1986). This method, associated with a contour propagation method specifically developed, was validated in the context of head and neck CT image registration, as part of this research. The proposed method will be deeply described in the following paragraph, for the most part based on Faggiano et al (Faggiano *et al* 2011).

3.1.2. Image registration method

In order to obtain an accurate description of anatomical and structural variations induced by RT on parotid glands, a registration and contour propagation method is required. The flow-chart of the whole procedure employed to extract geometrical indexes describing parotid glands deformations is represented in Figure 3.2. In this section the focus is on the implementation and validation of the

proposed method, while in the next one it is on the description of morphological indexes.

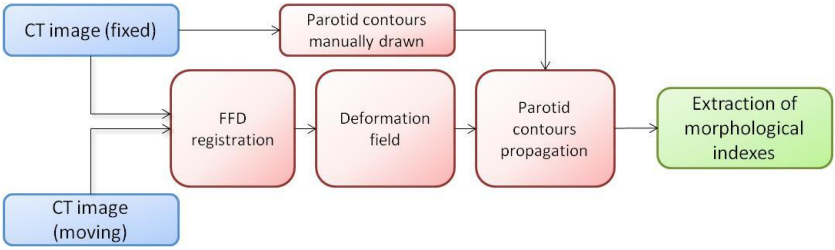

Figure 3.2. Flow-chart of the procedure employed to extract morphological indexes.

The adopted registration method was a classic sum of rigid and elastic transformation, modeled by a cubic B-spline hyperpatch (Rueckert *et al* 1999); the algorithm used mutual information and a four-step multi-resolution strategy (Mattes *et al* 2003). In the following paragraphs, the characteristics of the FFD registration will be described in terms of:

- Cost function (Mutual Information)
- Interpolation (B-spline)
- Transformation model (Free-form deformation)
- Optimization method

3.1.2.1. Cost function

For the estimation of the transformation between the two images, a cost function has to be defined and maximized (or minimized). In this implementation, the negative of the Mutual Information (MI) was used as term to be minimized. MI is a measure of statistical dependency between two data sets and it is particularly suitable for registration of images from different modalities, where intensity values of the two images could present any form of de-

pendency. MI between two random variables A and B starts from the entropy of the single variable, defined as:

$$H(A) = -\int p_A(a) log\ p_A(a) da$$

where $p_A(a)$ is the marginal probability density of that variable. The joint entropy of A and B is defined as:

$$H(A,B) = -\int p_{AB}(a,b)\ log\ p_{AB}(a,b) da\ db$$

where $p_{AB}(a,b)$ is the joint probability density of the variables A and B. If there is any dependency between A and B, then

$$H(A,B) < H(A) + H(B)$$

while if A and B are independent

$$H(A,B) = H(A) + H(B)$$

The MI between A and B is then defined as:

$$MI(A,B) = H(A) + H(B) - H(A,B)$$

Therefore, MI ≥ 0 and the equality is verified if A and B are independent.

In the discrete domain, as the digital image is, MI can be re-written as:

$$MI(A,B) = \sum_a \sum_b p_{AB}(a,b) log \frac{p_{AB}(a,b)}{p_A(a) p_B(b)}$$

Typically, the joint and marginal probability densities are not available and then these should be estimated from image data; MI estimation is thus calculated from the marginal and joint gray level image histograms. Usually, Parzen windows are used for this purpose, to generate continuous estimates of the underlying image distributions, thereby reducing the effects of quantization from interpolation and discretization from binning the data (Thévenaz and Unser 2000). With this method, densities are constructed taking from the image N samples of intensity values S ⊂ I (intensity values of the whole image) and super-positioning kernel functions centered on the sampled elements S. As kernel function, a large variety of functions could be used with the requirement of being smooth, symmetric, with zero mean and integrate to one. Typically, the parameters that have to be tuned in the implementation of MI calcula-

tion are the number N of voxels to be considered and the number of bins used for the histograms estimations.

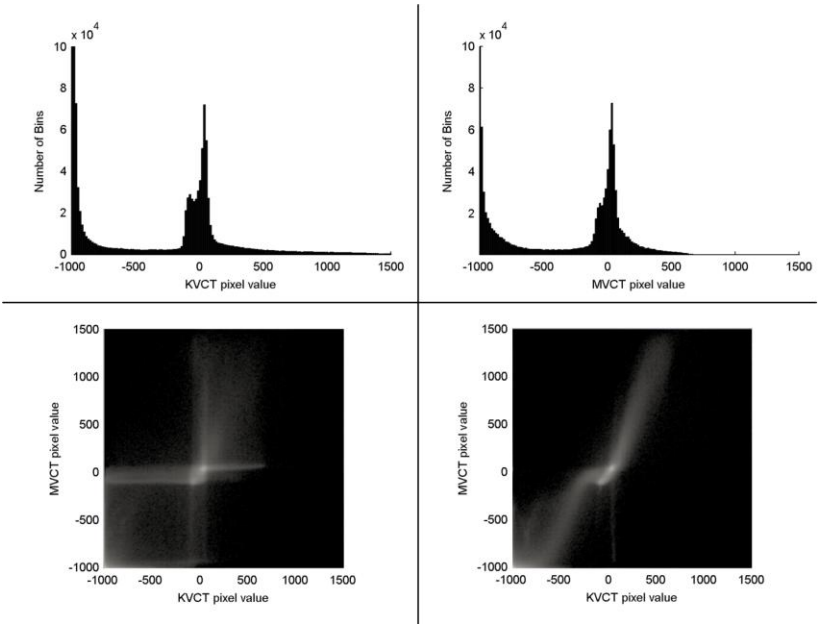

Figure 3.3: Marginal and joint gray level image histograms. In the first row, kVCT (left) and MVCT (right) histograms denote a similar gray level distribution in the two images. In the second row, joint gray level image histograms before image registration (left) and after image registration (right) are shown. The dispersion in the joint histogram after image registration is reduced, denoting good efficacy of the registration method.

An example of joint histogram is presented in Figure 3.3: in this case a kVCT image was considered as fixed image and a MVCT image was considered as moving image. The two studies have similar information content (first row) with a soft tissue intensity ranging from −200 to 250 HU (Hounsfield Unit) in kVCT and from −300 to 180 HU in MVCT, approximately. The spatial misalignment, present before registration, results in a joint histogram with marked disper-

sion (second row, left), indicating that the gray level of a pixel in an image does not systematically correspond to a specific gray level of the corresponding pixel in the second image. The effect of MI image registration in recovering the spatial mismatch is highlighted by the decreased dispersion of the joint histogram, which shows better correlation between pixel gray levels in the whole range (second row, right).

3.1.2.2. Spatial interpolation

Elastic transformation and image representation are modeled by using cubic B-spline as interpolant function (Unser 1999). Cubic B-spline are piecewise polynomial functions of degree 3 and are defined as the convolution of B-spline of degree (n-1) with B-spline of degree 0. In particular, basis function of the B-spline are the following:

$$B_0(x) = \frac{(1-x)^3}{6}$$
$$B_1(x) = \frac{3x^3 - 6x^2 + 4}{6}$$
$$B_2(x) = \frac{-3x^3 + 3x^2 + 3x + 1}{6}$$
$$B_3(x) = \frac{x^3}{6}$$

The general formulation of cubic B-spline is (see also Figure 3.4 for a graphical representation):

$$\beta^{(3)}(x) = \begin{cases} \frac{1}{6}(4 - 6x^2 + 3|x|^3), & 0 \le |x| < 1 \\ \frac{1}{6}(2 - |x|)^3, & 1 \le |x| < 2 \\ 0, & 2 \le |x| \end{cases}$$

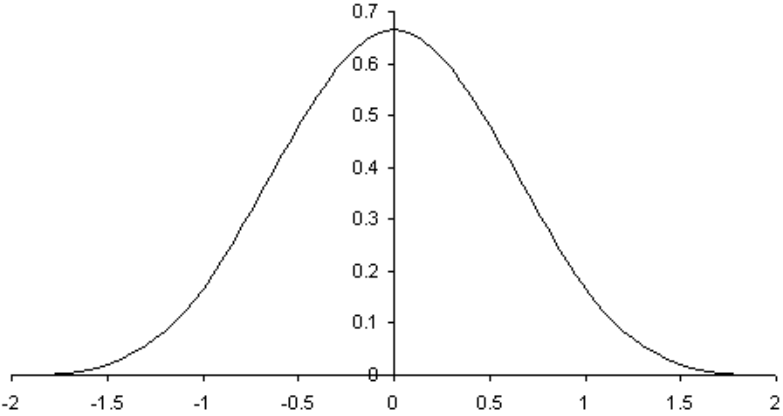

Figure 3.4. Graphical representation of cubic B-spline for mono-dimensional case.

In contrast to thin-plate splines, B-splines are locally controlled, which makes them computationally efficient even for a large number of control points. In particular, the basis functions of cubic B-splines have a limited support, i.e. changing control point affects the transformation only in the local neighborhood of that control point.

3.1.2.3. Transformation model

The transformation that has to be estimated is a composition of rigid motion recovery to correct global misalignment and local elastic deformation:

$$\boldsymbol{T}(x, y, z) = \boldsymbol{T_{rigid}}(x, y, z) + \boldsymbol{T_{elastic}}(x, y, z)$$

Rigid transformation: The rigid motion recovery is a classical global rigid transformation in 3D with 6 degrees of freedom (3 parameters for translation and 3 parameters for rotation):

$$\boldsymbol{T_{rigid}}(\boldsymbol{x}) = \boldsymbol{R} \cdot \boldsymbol{x} - \boldsymbol{T}$$

where ***R*** is a 3x3 homogeneous rotation matrix characterized by the Euler angles (θ, γ, ϕ), $\boldsymbol{x}=[x,y,z]^T$ is the position of any voxel in the fixed image and $\boldsymbol{T}=[t_x, t_y, t_z]^T$ is the translation vector. Therefore, the parameters to be estimated are:

$$\lambda_r = \{\theta, \gamma, \phi, t_x, t_y, t_z\}$$

Elastic transformation: The elastic deformation is estimated by the FFD model, based on B-splines. A deformation is defined on a sparse, regular grid of control points $\phi_{i,j,k}$ with resolution $\rho=[\rho_x, \rho_y, \rho_z]$, placed over the test image and is then varied by defining the motion $g(\phi_{i,j,k})$ of each control point. The FFD can be written as the 3D tensor product of the 1D cubic B-splines:

$$\boldsymbol{T_{elastic}}(x,y,z) = \sum_{l,m,n=0}^{3} B_l(u) B_m(v) B_n(w) \phi_{i+l,j+m,k+n}$$

where $i = \lfloor x/\rho_x \rfloor$, $j = \lfloor y/\rho_y \rfloor$, $k = \lfloor z/\rho_z \rfloor$, $u = \frac{x}{\rho_x} - i$, $v = \frac{y}{\rho_y} - j$, $w = \frac{z}{\rho_z} - k$, and B_l represents the *l*th basis function of the B-spline. The unknown parameters are the values of the control points $\phi_{i,j,k}$. The higher the number of control points, the higher the resolution of the grid and thus of the estimated transformation, but the higher the computational cost.

3.1.2.4. Optimization method

The optimization method adopted is different for the estimation of rigid and elastic transformation: for the rigid method a variant of gradient descent optimizer is used, while L-BFGS-B (limited memory Broyden, Fletcher, Goldfarb and Shannon minimization) optimizer is employed for the elastic registration (Jorge. Nocedal and Wright 1999). This method is useful here because of the high dimensionality of the parameter space: instead of estimating the entire Hessian during minimization, only a low-rank approximation is calculated.

The optimization criterion provides an efficient hierarchical multi-resolution scheme, in order to avoid local minima and to decrease computation time. The basic idea of multi-resolution is to initially recover the gross motion of the patient and large anatomic structures and then, increasing the resolution, to recover finer misalignments. This scheme is controlled by the resolution of the deformation grid, the number of image samples used to measure MI, the variance of the Gaussian blurring and the optimizer's termination criterion (see Figure 3.5). In particular, as the resolution increases, the Gaussian kernel narrows, the number of considered voxels increases and the stopping criterion decreases. In Table 3.1 multi-resolution parameters used in this implementation are reported.

Table 3.1. Multi-resolution parameters used for elastic registration

Parameters	**Level 1**	**Level 2**	**Level 3**	**Level 4**
Gaussian kernel (pixels)				
If dimension along z ≥ (dimension along x)/2	16/16/16	8/8/8	2/2/2	0/0/0
If dimension along z < (dimension along x)/2	16/16/8	8/8/4	2/2/2	0/0/0
Percentage voxels used in MI estimation	0.8	3.4	9.3	19.7
Stopping criterion	10^{-5}	10^{-6}	10^{-7}	10^{-8}
Final grid spacing	10x10x10 mm^3			

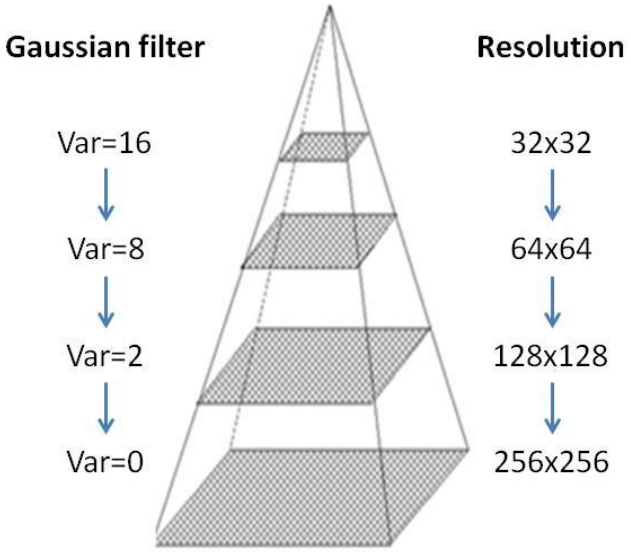

Figure 3.5. Multi-resolution scheme with the definition of the variance of the Gaussian filter and the grid resolution for each step.

Another step introduced to optimize the image registration performance is a pre-processing step by which the fixed and moving images are cropped and processed to maximize the mutual information in the region of interest. Therefore, the two images were resized and resampled to the same image size and resolution, and cropped around the volume of interest in order to avoid a great number of spatial samples belonging to the background. Then, we masked the background and bone areas to constrain the algorithm not to deform these regions. First, a threshold was applied to individuate the head and to set all the voxels outside this region to a fixed value of -1000 HU. For bone mask, a threshold of 300 HU was applied to obtain a binary bone segmentation, that was refined using morphological operations to merge or remove small islands. Fi-

nally, voxels inside the bone mask were set to 3000 HU (see Figure 3.6).

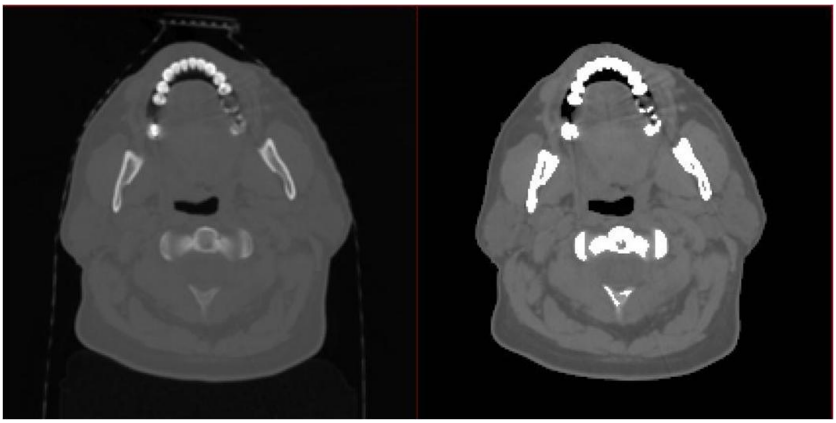

Figure 3.6. Pre-processing step of bone and background saturation. On the left: original CT image; on the right: saturated CT image.

3.1.3. Contour propagation method

After the estimation of the deformation field between the two images, a contour propagation method is needed to obtain a spatial correspondence of the considered structures of interest (see Figure 3.7). The contour propagation method here adopted and described in (Faggiano *et al* 2011) consists of a surface 3D mesh generation step followed by a mesh deformation step. The triangular mesh of parotid gland is generated from the contour points manually delineated by an expert on each CT slice, using the Power crust method proposed by Amenta et al (Amenta *et al* 2001). These surfaces are then deformed through the FFD procedure:

1. The world coordinate space (*x,y,z*) containing the object is associated to a parametric hyperpatch, defined by a trivariate cubic B-spline tensor product volume;

2. Object vertices are transformed into the hyperpatch reference coordinate system;
3. A number of control points are displaced with a consequent distortion of the hyperpatch;
4. Deformation estimated by the image registration step is applied to all the parameterized object vertices to produce the deformed object in the world coordinate.

The final deformed contours are obtained by cutting the deformed object through the transversal plane. The FFD surface deformation method ensure a regular parotid surface which does not need any post-deformation smoothing.

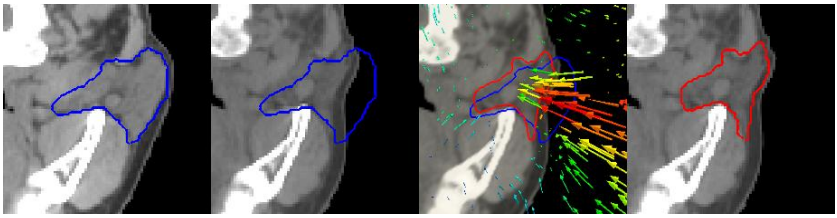

Figure 3.7. Description of contour propagation algorithm. From left to right: parotid contour manually drawn on CT1; parotid contour manually drawn on CT1 visualized on CT2; displacement map; deformed contour visualized on CT2.

3.1.4. Accuracy evaluation of contour propagation method[1]

To evaluate the accuracy of the contour propagation method in parotid glands delineation, we investigated inter-observer variability in contouring parotid glands on MVCT images and compared the results of the automatic method with the protocol- related observer variability. The analysis of operators contour variability in

[1] Based on Faggiano E et al. An automatic contour propagation method to follow parotid glands deformation during head-and-neck cancer Tomotherapy. Physics in Medicine and Biology, 2011. 56 (3), pp 775-791.

kVCT and MVCT also allowed us to verify the potential impact of contour propagation in this specific application.

3.1.4.1. Clinical dataset

For this validation, we considered 10 patients treated for HNC on an Helical Tomotherapy (HT) unit (HiArt2 Tomotherapy, Madison, Wisconsin). The planning kVCT images of all patients were acquired with a multislice CT scanner (GE Medical System), with a number of slices ranging from 66 to 129, an image plane size of 512 x 512 pixels and voxel size equal to 0.976 x 0.976 x 3.27 mm^3. The daily MVCT images of all patients were acquired using the on-board HiArt2 CT scanner of the Tomotherapy unit before each treatment fraction and were clinically used for patient repositioning. Each slice was 512 x 512 pixels with variable voxel size from 0.754 x 0.754 x 4 mm^3 to 0.754 x 0.754 x 6 mm^3.

MVCT delivers higher doses to the patient with lower image quality than diagnostic kVCT. MVCT images were relatively smaller and were included in the reference kVCT image space, as MVCT acquisition was restricted to the irradiated volume with small cranial-caudal margins.

The number of slices was different for each patient on different days, ranging from 23 to 48 for a voxel axial dimension of 4 mm, and from 19 to 36 for a voxel axial dimension of 6 mm.

For this study we used the planning kVCT scans of each patient and the final daily MVCT image (fraction 30, on average after 45 days from the start of the therapy).

3.1.4.2. Inter-observer variability.

Three expert operators manually contoured parotid glands slice-by-slice on the transversal view of the kVCT and MVCT studies of our dataset using a commercially available treatment planning software (Varian Eclipse v.8.6). No observers had knowledge of contours outlined by the other observers.

First, inter-observer variability related to both KVCT and MVCT was evaluated testing the equivalence between the three operators in terms of volumes and centre-of-mass (COM) distances using a two-way Anova test. The normality of the variables distributions was verified for volumes and COM distances using the Jarque-Bera test. A post-hoc Tukey test was used to evaluate statistical significance of the difference between two operators.

Parotid glands volumes were estimated using Gauss' theorem (Hughes *et al* 1996) and distances between right and left parotid COM were collected as suggested in (Lee *et al* 2008).

Then, a comparative analysis between kVCT and MVCT contouring variability was carried out in terms of DICE similarity coefficient (DSC) (Dice 1945) and volume variability coefficient (DeltaVol) (Geets *et al* 2005). Given two binary masks representing the area delimited by a contour, DSC was calculated as

$$DSC = 2\frac{A \cap B}{A + B}$$

where A and B are two different binary masks. DSCs were calculated between each pair of operators and averaged to obtain a mean index (Op-Op) for both kVCT and MVCT.

To calculate DeltaVol, the volume that is common to all observers (common volume) and the volume that encompasses all observers (encompassing volume) were calculated. DeltaVol was then obtained as the ratio between the common and the encompassing volumes (Geets *et al* 2005).

As DSC and DeltaVol indices were non-normal distributed (Jarque-Bera test), differences between their values in kVCT and in MVCT were tested using the non parametric Wilcoxon signed rank test.

In Table 3.2 parotid volumes and COM distances, estimated by the three observers on both kVCT and MVCT, are reported: there was no statistical difference among different operators in parotid volume estimation on kVCT (p=0.453) while differences were significant in MVCT contouring (p=0.0176). Regarding COM distances val-

ues, no statistical difference among different operators both in kVCT and in MVCT was found.

Table 3.2. Inter-observer variability in terms of volume and Centre-of-mass (COM) distance of parotid glands manually drawn by the three observers (mean value ± standard deviation).

	KVCT			**MVCT**		
	Op1	Op2	Op3	Op1	Op2	Op3
Volume [mm^3]	25.2 ± 6.3	24.6 ± 6.5	24.4 ± 6.3	16.8 ± 5.1	16.4 ± 5.0	18.2 ± 5.0
Anova		p=0.45			p=0.018	
COM distance [mm]	115.4 ± 8.3	115.4 ± 8.2	115.1 ± 8.2	111.4 ± 8.4	111.0 ± 8.6	110.4 ± 7.7
Anova		p=0.74			p=0.21	

Table 3.3 summarizes average DSCs and DeltaVols for both kVCT and MVCT studies. MVCT contours resulted significantly different from those drawn on kVCT ($p<0.05$) in terms of both DSC and DeltaVol values: MVCT indices were significantly lower than kVCT, indicating worst match in MVCT contour delineation. Finally we can note that kVCT DSC indices were always greater than 0.81 indicating good agreement between operators, while MVCT values ranged from 0.67 to 0.87, thus demonstrating more variability.

Table 3.3. Inter-observer variability in terms of Dice index (DSC) and DeltaVol, averaged between operators and subjects, presented as mean value ± standard deviation. Wilcoxon test is performed to evaluate significant differences between KVCT and MVCT.

	KVCT	MVCT	Wilcoxon test (p-value)
DSC	0.85 ± 0.03	0.79 ± 0.04	$2.2 \cdot 10^{-4}$
DeltaVol	0.64 ± 0.05	0.53 ± 0.07	$2.5 \cdot 10^{-4}$

3.1.4.3. Accuracy of contour propagation.

To apply contour propagation to our dataset, we created a median kVCT contour from the kVCT contours of the three observers. For each slice a coverage matrix was constructed: for each voxel on a 0.976 mm grid it was scored how many times the voxel was inside a contour. The median boundary was constructed by founding the 50% isocontour of the coverage image using a B-spline interpolation algorithm. KVCT and MVCT were then roto-translated and elastically registered to obtain control points displacements. A median mesh was then generated and deformed using our contour propagation method.

The deformed median kVCT contours on daily MVCT scans were qualitatively, i.e. visually, inspected by the three observers to ensure that they were within established anatomic boundaries of the parotid glands.

For quantitative evaluation, the deformed contours were compared with the manual contours directly outlined on MVCT images by the three observers, with the purpose of assessing if the uncertainties of the automatic contours fell within those of the human observers. This analysis was carried out by studying both the 3D performance and the 2D performance of our method. To analyze the 3D performance we compared parotid volumes and COM distances through Anova analysis of variance and DSC operator vs. operator (Op-Op) values to operator vs. automatic (Op-A) values through a Wilcoxon signed rank test. Since MVCT did not always

cover the extent of parotid glands and, additionally, parotid contours were usually delineated on 2D images, we performed a supplementary 2D analysis to verify the goodness of automatic 2D contours on axial image planes. In this analysis we excluded slices that were not contoured by all the operators in order to mask out the superior and the inferior end of parotid glands that were not well defined in MVCT images and involved large human variations (Zhang *et al* 2007, Lee *et al* 2008). 2D accuracy of contour propagation was evaluated in terms of Average Symmetric Distance (ASD) and Maximum Symmetric Distance (MSD) (Heimann *et al* 2009). Zero value for the two indices represents a perfect matching between two contours. The ASD gives an averaged accuracy assessment while MSD distance captures the worst case mismatch.

ASD between 2D contours A and B is defined by the following formula:

$$ASD(A,B) = \frac{1}{|C(A)| + |C(B)|}\left(\sum_{C_A \in C(A)} d\big(C_A, C(B)\big) + \sum_{C_B \in C(B)} d\big(C_B, C(A)\big) \right)$$

where *C(A)* and *C(B)* indicate the set of voxels belonging to the contours A and B, respectively; *d(v,C(A))* and *d(v,C(B))* indicate the shortest distance between an arbitrary voxel and the contours A and B, respectively, calculated using a 3D Euclidean distance map (Maurer Jr *et al* 2003), which found the closest point on the test contour from each reference contour point.

MSD is determined on the basis of the same considerations adopted for the ASD, but it yields the maximum distance between the contour sets, therefore being most sensitive to outliers. It is defined as:

$$MSD(A,B) = max\left\{ \max_{C_A \in C(A)} d(C_A, C(B)), \max_{\mathrm{C_B \in C(B)}} \mathrm{d(C_B, C(A))} \right\}$$

The final value was then obtained as the mean (for ASD) and the maximum (for MSD) value over the slices common to all the four delineations (Huyskens *et al* 2009).

Average ASD and maximum MSD between operators (Op-Op) and between automatic and operator (Op-A), were then calculated between each pair of manual contours and between automatic contour and each manual contour, respectively (Huyskens *et al* 2009).

As ASD and MSD were non-normal distributed (Jarque-Bera test), statistical significance of the differences between Op-A and Op-Op indices was assessed using Wilcoxon signed rank test.

All statistical analyses were performed using MATLAB 64bit (R2009b, The MathWorks, Natick, MA) and R (Hart *et al* 1994).

Table 3.4 summarizes the results of the 3D analysis of contour propagation accuracy. No significant differences were found between the automatic method and the manual contour delineations in terms of parotid volume ($p>0.05$ in multiple comparisons Tukey test), parotid COM distances ($p=0.3043$ by the Anova test) and DSC values ($p=0.1672$ by the Wilcoxon signed rank test).

Table 3.5 summarizes 2D analysis of accuracy. Also in these cases, no statistically significant systematic difference was found between manual and automatic contouring ($p=0.2043$ for ASD and $p=0.8228$ for MSD, by the Wilcoxon signed rank test).

These results suggest that the automatic contour method could successfully substitute manual operator, as it could be assessed in Figure 3.8.

Table 3.4. 3D analysis of contour propagation accuracy. Mean value ± standard deviation of parotid volume and COM distances are reported for each operators and the automatic method. For DSC index, mean value ± standard deviation are reported as average between operators (Op-Op) and between automatic and operators (Op-A).

	Op1	Op2	Op3	Auto
Volume [mm^3] *	16.8 ± 5.1	16.4 ± 5.0	18.2 ± 5.0	17.5 ± 5.1
COM distance [mm] **	111.4±8.4	111.0 ± 8.6	110.4 ± 7.7	111.2 ± 8.0

	Op-Op	Op-A
DSC ***	0.79 ± 0.04	0.77 ± 0.05

* No significant differences found (Tukey test)
** No significant differences found (Anova test)
*** No significant differences found (Wilcoxon test)

Table 3.5. 2D analysis of contour propagation accuracy. Mean value ± standard deviation of average symmetric distance (ASD) and maximum symmetric distance (MSD) between operators (Op-Op) and automatic and operators (Op-A) are reported.

	Op-Op	Op-A
ASD [mm] *	1.57 ± 0.24	1.66 ± 0.34
MSD [mm] *	9.49 ± 1.90	9.47 ± 2.17

* No significant differences found (Wilcoxon test)

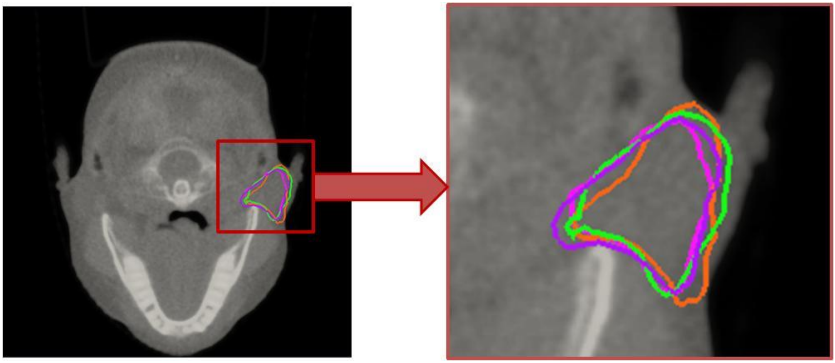

Figure 3.8. Comparison between manual contours drawn by the 3 experts (expert1, expert2, expert3) and the contour obtained by the algorithm (automatic contour). On the right, in the zoomed image, it is possible to see that the automatic contour is placed in the same position than the other three.

3.2. QUANTIFICATION OF DEFORMATION

Once image registration method was applied to a set of CT images acquired during RT treatment, and therefore the anatomical deformation was estimated and recovered, a quantification of these geometrical changes is useful for the evaluation of the treatment itself and of the correlated side-effects on normal tissues. The easiest index that can be extracted from CT images is the volume of the structure of interest (parotid gland in our case): the contour propagation method previously described guarantees that the considered parotid volume in each CT study is related to the same spatial location. Therefore, every volume variation can be related to anatomical modifications induced by the radiation treatment, unless the registration error previously estimated.

A direct quantification of the deformation can also carried out in terms of compression and expansion of each single voxel, using the Jacobian index.

3.2.1. Definition of the Jacobian index

As deeply described in the previous section, every point in the registered image $\boldsymbol{x_e}=(x_e, y_e, z_e)$ is defined by the corresponding point in the fixed image $\boldsymbol{x_f}=(x_f, y_f, z_f)$ and by the estimated transformation: $\boldsymbol{x_e}=\boldsymbol{x_s}+T(\boldsymbol{x_s})$. The Jacobian of the transformation is then defined as:

$$Jac(x) = \det(\nabla x_e) = \det\left(\nabla\left(x_s + T(x_s)\right) = \det\left(I + \nabla T(x_s)\right)\right.$$

where I is the identity matrix and grad is the transformation gradient. This index quantifies the shrinkage or the expansion of the single voxel; in particular: Jac=1 corresponds to a voxel that doesn't change; Jac>1 identifies an expanding voxel and Jac<1 a shrinking voxel (Davatzikos *et al* 1996, Ding *et al* 2010). A negative Jacobian index indicates a folding in space, which is not consistent with a physically admissible deformation, and thus it should be avoided: FFD, thanks to B-splines properties of local control and smoothness, has very few voxels (generally less than 1% of the image) characterized by a negative Jacobian value.

The Jacobian map can be visualized on the CT image using a different colormap, in order to easily individuate the expanding regions and the shrinking regions. In Figure 3.9, an example of the jacobian map overlapped on the reference CT image is shown: in particular, the colormap from green to blue indicates compression areas (green: Jac≈1; blue: Jac≈0), whilst the colormap from yellow to red indicates expanding areas (yellow: Jac≈1; red: Jac≈2).

The mean Jacobian index within an organ of interest (Jac_mean), calculated as the average value between all voxels belonging to this structure, is descriptive of the average deformation of the organ itself. This parameter can help in assessing the anatomical behaviour of parotid glands as a consequence of radiation treatment. In particular, the study of the correlation between parotid deformation at the end of RT and some clinical, anatomical and dosimetric parameters can be helpful in determining those pretreatment indexes predicting large anatomical variations. This type of analysis could provide some useful information about the optimi-

zation of the treatment and for the selection of those patients who could better benefit of a re-planning strategy. In this section, the assessment of the correlation between Jac_mean and pre-clinical parameters is presented in a large population of patients treated for head-and-neck cancer.

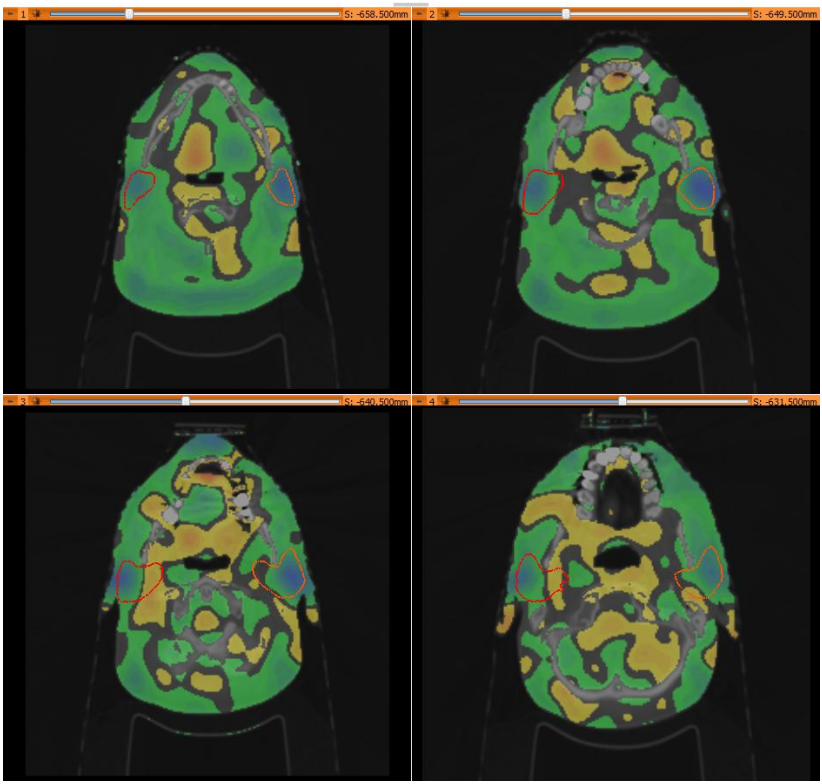

Figure 3.9. Example of jacobian map overlaid on the CT image and with parotid gland structure (in red), at different axial planes: from green to blue: shrinking voxels (1-->0); from yellow to red: expanding voxels (1-->2); uncolored voxels: no deformation (Jac=1). From the picture it is evident that shrinkage is focused on the superficial lobe of the parotid.

3.2.2. Patient dataset and imaging procedure

Data of 168 parotid glands of 84 patients from three institutions treated for different Head and Neck cancer, both with radical and adjuvant intent, were pooled. Median patient's age was 59 years (range: 29-86 years). Most of the patients (79/84, 94%) didn't undergo upfront surgery. 75/84 (89.2%) patients received chemotherapy: in 18 patients as neo-adjuvant treatment while concomitant to radiotherapy in 70 cases. 12 patients received both neo-adjuvant and concomitant chemotherapy. All patients were treated with intensity–modulated techniques (IMRT): 41 patients with the Helical Tomotherapy Unit, 43 with the conventional Linac IMRT, in dynamic or step-shoot modality. An inverse planning optimization approach was considered with the goal to deliver at least 95% of the prescribed dose to at least 95% of each PTV volumes, while keeping the dose as homogeneous as possible and sparing parotids without compromising PTVs coverage.

Parotid deformation was evaluated through images taken at start and at the end of the treatment. For the 41 patients treated with Helical Tomotherapy, MVCT images were acquired with 4-6 mm slice thickness; for the rest of the population, treated with conventional Linac IMRT, KVCT images were available with 3-5 mm slice thickness. The in-plane pixel resolution was about 1 mm in each image.

Image registration was performed between the images acquired at the beginning (MVCT/KVCT1) and at the end (MVCT/KVCT2) of the treatment, using the FFD method described in the previous section. The estimated deformation field was used to calculate the Jac_mean of the parotid glands, manually delineated on MVCT/KVCT1 by an expert in radiological images.

3.2.3. Clinical/geometric and dosimetric data

A number of clinical, anatomical/geometric and dosimetric data were collected. Age, chemotherapy (y/n), neo-adjuvant (y/n) and concomitant (y/n) chemotherapy, surgery (y/n) and primary

tumour site (oropharynx, nasopharynx, hypopharynx, larynx) were considered as clinical variables. Anatomical/geometric and dosimetric parameters included: initial parotid volume (IVP) (average: 27.49cc; range: 7.58–63.48 cc), tumour volume (T) (average:232.73cc; range:7.22–577.62cc), overlap between the parotid gland and the lynphnode chain volume (OVPPTV2) (average:4.10cc; range:0–22.90cc) and between the parotid and the high dose tumour (OVPPTV1) (average:1.11cc; range:0–14.20cc), prescribed dose and daily dose, parotid planning mean dose (Dmean) (average:33.03Gy; range: 20.20-70.42Gy) and V10-V40 dose–volume histogram (DVH) values at planning. In addition to these "pre-treatment" parameters, the absolute and the percentage body thickness variation (ΔT) between the start and the end of the treatment were also considered. Thickness variation was measured on the available CT images as the difference between the half-thickness between the end and the start of the therapy at the level of C2, taking the line tangent to the vertebral body on CT, selecting the side opposite to the disease and/or to previous neck surgery.

3.2.4. Statistical analysis

Several statistic tests were performed to assess correlation between parotid shrinkage and all considered parameters.

First, the correlation between Jac_mean and all the recovered parameters was assessed through Spearman's test. An univariate and a stepwise logistic multivariate analysis (MVA, selecting variables with p-value<0.1) were performed by considering as the end point the parotid Jac_mean value smaller than the first quartile value of the population (Q1). Parotid glands DVHs were stratified according to their degree of deformation, trying to assess the most predictive dose-volume combination in the low and medium dose region. Logistic MVA analyses including the shape of DVHs were also performed. Analyses were carried out with the MedCalc software (v. 12.1.4, MedCalc software bvba).

Table 3.6. Results of Spearman's correlation tests between parotid Jac_mean and the pre-treatment variables

Variable	***p-value***
Institute	0.192
Chemotherapy (y/n)	0.725
Chemo - neoadjuvant (y/n)	0.923
Chemo - concomitant (y/n)	0.369
Surgery (y/n)	0.378
Age	0.021
Tumor Site	0.001
Tumor Volume	0.152
Initial Parotid Volume (IVP)	0.193
Overlap parotid-lymphonodal tumour	0.003
Overlap parotid- tumour	0.004
Prescribed lymphonodal tumour dose	0.152
Prescribed tumour dose	0.030
Daily lymphonodal tumour dose	0.514
Daily tumour dose	0.606
Parotid mean dose (Dmean)	0.0005
V10	<0.0001
V15	0.0001
V20	0.0015
V30	0.0106
V40	0.0003

3.2.5. Results

3.2.5.1. Correlation between Jac mean and clinical/dosimetric parameters

It was found that, on average, the 82.6% of the parotid glands voxels experiments a shrinkage effect (Jac<1), and, in particular, 13.7% of voxels presents a compression greater than 50% (Jac<0.5).

The average value of Jac_mean among patients was 0.77 (median value=0.76; range: 0.38-1.10; first quartile Q1=0.67). Only 5.9% (10/168) of the parotid glands showed an expanding behaviour (Jac_mean>1).

Results of correlation tests for Jac_mean and all clinical, geometric, anatomic and dosimetric variables are reported in Table 3.6. Based on correlation tests, OVPPTV1 (p=0.004), OVPPTV2 (p=0.003), age (p=0.021) were found as the pre-treatment anatomical/clinical/geometric variables mostly correlated with Jac_mean; Dmean (p=0.0005) and all the DVH parameters, V10 (p<0.0001), V15 (p=0.0001), V20 (p=0.0015), V30 (p=0.0106), V40 (p=0.0003), were also found significantly correlated with Jac_mean. In addition to pre-treatment parameters, absolute and percentage body thickness variation were found significantly correlated (p<0.0001) with parotid deformation.

3.2.5.2. Risk of large deformations: pre-treatment variables

The results for the logistic univariate analysis are reported in Table 3.7 when considering Jac_mean<Q1. Focusing on pre-treatment parameters, OVPPTV1 (p=0.002; OR=0.934, CI:0.895-0.976) and OVPPTV2 (p= 0.005; OR=0.966, CI: 0.943-0.990) were found as the most predictive geometric variables; while V10 (p=0.019; OR=0.949, CI:0.909-0.992), V15(p=0.041; OR=0.974, CI: 0.950-0.999) and V40 (p=0.041; OR= 0.976, CI:0.953-0.999) were the dosimetric ones. MVA analysis reported that age (p=0.02; OR=1.05, CI:1.01-1.09) and OVPTV1 (p=0.0006; OR=0.92, CI:0.88-0.96) were found as the best independent pre-treatment predictors (p=0.0001; AUC=0.69 (0.61-0.75)). If we exclude geometrical parameters, (being correlated to dosimetric variables), V10 (p=0.02; OR=0.95, CI: 0.91-0.99) was found as the best predicted variable (p=0.008; AUC=0.64 (0.56-0.71)).

Table 3.7. Results of Univariate logistic analysis. End point: Jac_mean<0.67 (first quartile value of the population).

Variable	***p-value***
Chemotherapy (y/n)	0.647; OR= 0.76 (0.24 -2.42)
Chemo - neoadjuvant (y/n)	0.192; OR= 0.47 (0.15 – 1.45)
Chemo - concomitant (y/n)	0.892; OR= 0.94 (0.40 -2.21)
Surgery (y/n)	0.097; OR= 0.35 (0.10 -1.21)
Age	0.070; OR= 1.03 (0.998 -1.07)
Tumor Site	0.032; OR= 1.75 (1.05 -2.91)
Tumor Volume	0.2; OR= 0.999 (0.996 – 1.001)
Initial Parotid Volume (IVP)	0.56; OR= 0.990 (0.95 -1.03)
Overlap parotid-lymphonodal tumour	0.005 ; OR= 0.97 (0.94 -0.99)
Overlap parotid- tumour	0.002; OR= 0.93 (0.895 -0.976)
Prescribed lymphonodal tumour dose	0.824; OR= 0.99 (0.89 -1.10)
Prescribed tumour dose	0.557; OR= 1.03 (0.94 -1.12)
Daily lymphonodal tumour dose	0.416; OR= 2.84 (0.23 -35.31)
Daily tumour dose	0.647; OR= 0.67 (0.12 -3.67)
Parotid mean dose (Dmean)	0.042; OR= 0.96(0.92 -0.998)
V10	0.019; OR= 0.949 (0.909 – 0.992)
V15	0.041; OR= 0.974 (0.950 -0.999)
V20	0.104; OR= 0.98 (0.96 -1.004)
V30	0.129; OR= 0.981 (0.96 - 1.006)
V40	0.041; OR= 0.976 (0.953 -0.999)

3.2.5.3. Risk of large deformations: shape of parotid DVH

In order to better understand the correlation between parotid deformation and dosimetric parameters, the impact of the DVH shape was better investigated in the following way: the aver-

age DVHs of parotid gland with Jac_mean<Q1 (large shrinkage) and Jac_mean≥Q1 (small shrinkage) were compared through a two-tails t-test. As result, V10 and V40 were assessed as the most predictive dosimetric parameters, being corresponding to the lowest p-values. A further ROC analysis found V10=93% (sensitivity: 41.4%, specificity: 82.5%) and V40=36% (sensitivity: 68%, specificity: 52.5%) to be the best cut-off values discriminating large and small shrinking parotids. Parotid glands were then separated according to their DVH shape as: bad-DVH (V10>93% and V40>36%), intermediate-DVH (V10>93% and V40<36%), good-DVH (V10<93%). The risk to have Jac_mean<Q1 was 39.6% vs 19.6% vs 11.3% in three groups respectively (p=0.0001). When adding the "DVH grouping" variable in the MVA, patient's age (p=0.028; OR=1.04, CI:1.005-1.086), OVPPTV1 (p=0.009; OR=0.93, CI:0.88-0.98), OVPPTV2 (p=0.085; OR=0.96, CI:0.92-1.01), V30 (p=0.012; OR=1.07, CI: 1.01-1.12) and bad-DVH (p=0.0035; OR: 0.19; CI:0.06-0.58) were found as the clinical, geometric and dosimetric variables more significantly correlated with large parotid deformation (p<0.0001; AUC=0.78, CI:0.71-0.84). If we exclude geometric parameters correlated with dosimetric variables, patient's age (p=0.077; OR=1.032; CI:0.997-1.069) and bad-DVH (p=0.0009; OR=0.282; CI:0.133-0.597) were found as the best independent predicted variables (p=0.0009; AUC=0.70, CI:0.63-0.77) of the risk of large shrinkage (Jac_mean<Q1).

3.2.6. Risk of large deformations: inclusion of patient modifications

When considering not only pre-treatment parameters, but also patient modifications, the percentage (p<0.00001; OR=1.1807, CI:1.1022-1.2648) and the absolute (p<0.00001; OR=9.1887, CI:3.6704-23.003) body thickness variation were found significantly correlated with Jac_mean. When including these variables in the backward MVA, the final models (including or excluding geometric parameters, i.e.: OVPPTV1 and OVPPTV2) the predictivity of the model increases, with AUC passing from 0.70 and 0.78 to 0.79 and

Table 3.8. Results of the logistic regression models by considering or not body thickness variation and overlaps between targets and parotid glands.

Conditions	***Predictive Variables***			***Significance/ ROC curve***
	Variable	p-value	OR (95% CI)	
Body Thickness (no) OVPTV1/OVPT2 (yes)	Age	0.03	1.04 (1.01-1.09)	p<0.0001 AUC=0.78 (0.71-0.84)
	OVPPTV1	0.009	0.92 (0.88-0.98)	
	OVPPTV2	0.09	0.96 (0.92-1.01)	
	V30	0.01	1.07 (1.01-1.12)	
	Bad-DVH	0.004	0.19 (0.06-0.58)	
Body Thickness (no) OVPTV1/OVPT2 (no)	Age	0.08	1.03 (1-1.07)	p=0.0009 AUC=0.70 (0.63-0.78)
	Bad-DVH	0.0009	0.28 (0.13-0.60)	
Body Thickness (yes) OVPTV1/OVPT2 (yes)	BodyTh%	< 0.0001	1.26 (1.14-1.39)	p<0.0001 AUC=0.87 (0.81-0.92)
	OVPPTV1	0.002	0.90 (0.84-0.96)	
	OVPPTV2	0.06	0.96 (0.91-1.00)	
	V20	0.06	0.95 (0.91-1.00)	
	V30	0.0009	1.15 (1.06-1.25)	
	Bad-DVH	0.0010	0.12 (0.03-0.42)	
Body Thickness (yes) OVPTV1/OVPT2 (no)	BodyTh%	0.0003	1.17 (1.08-1.28)	p=0.0001 AUC=0.79 (0.70-0.86)
	Bad-DVH	0.07	0.40 (0.15-1.07)	

0.87 respectively. In Table 3.8, a summary of the four logistic models (including or not body thickness variation and/or OVPPTV1/OVPPTV2) is shown: in any case, bad-DVH grouping always results to be highly correlated to the risk of large deformations.

Chapter 4

Extraction of structural indexes

The morphological indexes previously described in Chapter 3 can be considered as directly related to the parotid shrinkage, which has been extensively discussed in Chapter 2. In particular, in several works, on the basis of CT images acquired during RT, the authors have described anatomic variations with a global index intrinsically related to the deformation, such as the Jacobian index (Fiorino *et al* 2011) or the simple volume variation (Vásquez Osorio *et al* 2008, Teshima *et al* 2010). Beside the anatomical variations, recent investigations have suggested that parotid deformation may be related to complex structural and functional modifications of the glands, by investigating the change in global structure/function during RT through the measure of density variations (Fiorino *et al* 2012, Teshima *et al* 2012). In this scenario, a full exploitation of the information contained in CT images, provided, for example, by texture analysis, could lead to a more precise description of parotid gland modifications, in terms of structural characterization of tissue organization.

In this chapter, texture analysis and its applications in RT will be deeply discussed and this method will be introduced on CT images with the aim to characterize structural variations in parotid glands during the course of treatment and, moreover, the predic-

tion power of these parameters in early determining parotid shrinkage will be assessed.

4.1. TEXTURE ANALYSIS

4.1.1. State of art

Texture analysis has been used in various context in medical imaging, for identification, classification and segmentation of regions or structures. Ganeshan et al used texture analysis at different scales to reveal changes in apparently disease-free areas of the liver in colorectal cancer patients with liver metastases as compared to those with no evidence of tumour or extra-hepatic tumour only, making this detection less complex than classical perfusion techniques (Ganeshan *et al* 2009). Differentiation between aggressive and nonaggressive malignant lung tumors was performed in (Al-Kadi and Watson 2008) by measuring fractal dimension on Contrast Enhanced CT images, in order to enhance CT tumor staging prediction accuracy through identifying their malignant aggressiveness.

Classification of different grades of neoplasia was dealt by Ahammer et al, by the extraction of fractal dimension and statistical features from histological images of anal carcinoma (Ahammer *et al* 2011). A classification between different type of tissue in pelvic district (bladder, rectum and prostate) was performed with textural feature extraction in (Nailon *et al* 2008, Liao *et al* 2010). In these works, a method for features reduction was also presented, in order to identify the most powerful parameters in classifying tissues. Unsupervised classification results demonstrated that with a reduced feature set the approach offered significant classification accuracy on axial, coronal and sagittal CT image planes and had the potential to be developed further for radiotherapy applications, particularly towards an automatic outlining approach.

Texture analysis can be used also for automatic segmentation of structures, as proposed by Assefa et al in delineating glioblastoma on T1-w and T2-w MRI brain images (Assefa *et al*

2010). They have presented a new and computationally efficient technique for texture analysis based on the second order statistics of the power map of the localized Hartley transform. The power map enhanced dominant texture and revealed information which might not be accessible in the original image, allowing a more accurate segmentation of the structures of interest. In head and neck district, target delineation on parotid glands using a voxel-based approach based on textural information was described by (Yu *et al* 2009) on FDG-PET and CT images; a preliminary textural characterization of oral cancer involving buccal mucosa for the differentiation between the various grades of the tumor was proposed by (Raja *et al* 2012), using fractal dimension and statistical features.

Parotid glands structure was described in sonographic images using texture analysis to discriminate different type of salivary glands tumor, based on fractal dimension (Chikui *et al* 2005). Recently, a description of radiation-induced parotid gland injury was proposed in (Yang *et al* 2012) through the extraction of textural features from ultrasound images. In this case, textural features identified a different echo-pattern for irradiated glands with respect to normal subjects (see also Chapter 2.2) and, thus, these parameters have been proved to be able to correctly characterize the biological process induced by RT.

In this project, structural and functional changes during the therapy were assessed on CT images in two phases: first, a simple analysis of density variation in OAR was performed to evaluate first-order statistical variations (Palma *et al* 2011); then, a more complex texture analysis, including the extraction of first and second order statistical indexes and fractal dimension, was carried out to take into account changes in intensity pattern (Ahammer *et al* 2011). All these indexes were then correlated with pre-clinical and dosimetric parameters and with clinical outcomes, in order to reach an exhaustive description of the parotid glands behavior due to radiation.

4.1.2. Influence of noise and image registration in texture analysis

The assessment of the influence of quantum noise and blurring effect, typical in radiographic images, in the estimation of textural features, and in particular of fractal dimension, was dealt in literature by some groups. This is an interesting evaluation, since in real images the characteristics of the imaging technique influence their information content and thus the estimated textural features. The main source of noise in CT images is the quantum noise, which depends on the number of discrete x-ray photons reaching the detector. The most straightforward way to improve the signal to noise ratio is to increase the radiation dose to the patient, which has its own detriments.

Mathematically, the amplitude of the quantum noise closely follows a Poisson distribution, which can be approximated by a Gaussian when the count is large. Although the quantum noise occurs in the raw projection data, simulating its effects can be simplified by introducing it directly to the reconstructed image, following some linear attenuation corrections (Herman 2009). Therefore, to study the effects of quantum noise on the estimation of fractal dimension, Veenland et al (Veenland *et al* 1996) simulated different signal to noise ratios on synthetic fractal images (Peitgen *et al* 1988) by varying the noise level of a Poisson process and used a modulation transfer function to describe the image blurring. Different methods of fractal dimension estimation were tested with this images and results have shown a decrease in the estimated range, independently from the algorithm used. Therefore, when a comparison of fractal dimension in different images is needed, the only way to achieve a reliable result is to provide the same controlled acquisition protocol, in order to ensure similar image quality in terms of spatial resolution and signal to noise ratio.

The same group (Veenland *et al* 1998) evaluated the impact of noise and blurring on the estimation of other textural features: statistical indexes from co-occurrence matrix, features from the

Fourier Power Spectrum (Bajcsy 1973, Katsuragawa *et al* 1988, Liu and Jernigan 1990) and fractal dimension calculated with Power Spectrum method (Pentland 1984) and Blanket method (Peleg *et al* 1984). All texture analysis methods are negatively influenced by noise, although the influence of noise depends on the image type; again, the comparison of images with different noise characteristics is not sensible since the different image quality has a different influence on the discriminative performance of the methods.

Recently, the influence of registration in texture analysis was studied (Cunliffe *et al* 2012, Cunliffe *et al* 2013) for lung CT images. In several ROIs identified in the baseline CT within lung borders and matched in the follow-up CT using different image registration algorithms (rigid, affine, B-splines and demons) a total of 140 textural features were extracted and compared. Since the considered subjects were not affected by lung pathologies, the authors hypothesized that textural features had similar values in both CT studies; therefore, the effects of registration and image acquisition protocols were assessed by comparing values of the extracted features. Among the studied image registration methods, the lowest registration-dependent bias introduced in textural features was achieved by demons algorithm. Moreover, the authors identified the 19 "registration-stable" parameters and measured the magnitude of variation introduced by registration: this knowledge would allow for better distinction between texture differences caused by disease progression and texture differences from registration-induced artifacts (Cunliffe *et al* 2012). In the following work (Cunliffe *et al* 2013), the same authors went deeper in this kind of analysis, focusing on the effects of demons algorithm and trying to minimize the registration-induced changes in texture analysis. These works can thus help in choosing the better set of features for an accurate detection of local changes in serial CT lung images.

4.1.3. Texture analysis method

4.1.3.1. Metal artifacts correction[2]

In the HN district, dental filling can cause metal streaks artifacts that affect the image quality. Previous works have demonstrated that metal artifacts in HN district degrade the precision of contouring (O'Daniel *et al* 2007) and increase the dose estimation inaccuracies (Kim *et al* 2006). Metal streaks can also affect the estimation of intensity calculation (Yazdia *et al* 2005, Bal and Spies 2006), increasing the value of the standard deviation within a region of interest. Therefore, in RT it is important to reduce metal artifacts in CT images to improve contour delineation and densitometric evaluation.

Various methods of metal artifacts reduction (MAR) have been illustrated in literature, based on the interpolation of sinogram data, aimed at removing data belonging to metal trace (Kalender *et al* 1987, Wei *et al* 2004, Bal and Spies 2006, Abdoli *et al* 2009). I proposed here a modified version of a previously published algorithm (Meyer *et al* 2010) and I evaluated the improvement of image quality after the correction both qualitatively and quantitatively. In particular, variations in intensity calculation are studied to assess the adequacy of the correction to perform an accurate density analysis in ROIs for RT.

- Algorithm

Starting from the algorithm proposed by Meyer et al. (Meyer *et al* 2010), here a modified version of the proposed Normalized Metal Artefacts Correction (NMAR) is implemented. NMAR is a method based on sinogram inpainting, where metal trace in the original sinogram is treated as missing data and is then replaced by

[2] Based on Scalco E.; Fiorino C.; Sanguineti G.; Cattaneo G.M.; Rizzo G. Metal artifacts reduction for Radiotherapy application. Atti del Congresso Nazionale di Bioingegneria, Roma, 26-29 Giugno 2012.

interpolated data. Innovation in NMAR with respect to previous works is the step of normalization of the sinogram before the interpolation. To perform the normalization, a prior image is created; this image is a segmented version of the original image, where four different classes are defined: air, soft tissue, bone and metal. In (Meyer *et al* 2010) the original CT image is segmented using a simple thresholding, after having applied a Gaussian filter, to reduce the streaks artefacts. The metal class is then forward projected to define the metal trace in the original sinogram. The normalized sinogram is obtained by dividing the original sinogram by the prior sinogram, in order to give more emphasis to the metal trace and preserve bone information. Metal trace in the normalized sinogram is linearly interpolated and the corrected sinogram is denormalized; the final corrected image is obtained by a Filtered Back-Projection of the corresponding sinogram. A schematic representation of this algorithm is reported in Figure 4.1.

Two different modifications, as proposed by (Bal and Spies 2006), with respect to the original NMAR method are implemented:

1. an adaptive filter, instead of a Gaussian filter, was applied to the original image to reduce the noise content and to selectively smooth streaks artefacts.
2. k-means algorithm, instead of the simple thresholding, was used to automatically segment the filtered image into the four classes. A morphological operation of erosion is also performed on the metal class to correct misclassification errors of bone voxels, caused by the smoothing filter. In this case prior image can be obtained in a completely automatic way, thus avoiding the problem of choosing threshold values, although we expect a corrected image very similar to the one obtained using a simple threshold.

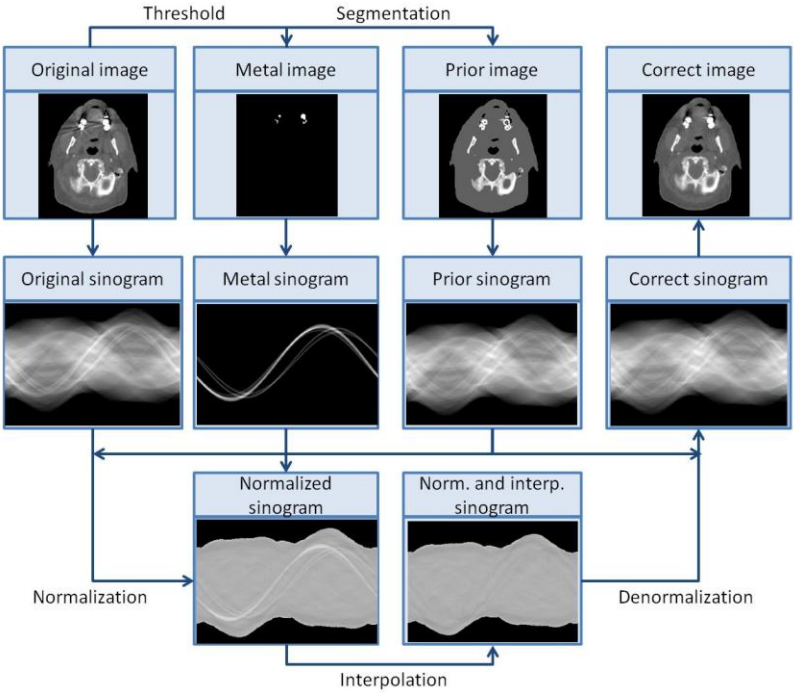

Figure 4.1. Schematic representation of the implemented NMAR method.

- Algorithm evaluation

The described algorithm was applied to 5 different CT images of the HN district of 5 patients undergone to RT treatment. Metal artefacts were due to multiple dental filling of both side of the jaw. Evaluation of the correction was made both qualitatively, by visually comparing image quality, and quantitatively. To quantify the effect of the algorithm, mean intensity value with its standard deviation of different ROIs in the images was calculated before and after metal artefacts correction, as proposed in (Bal and Spies 2006). ROIs were placed close to the source of artefacts (Art_ROI) and in a typical OAR (parotid glands) for HN RT planning. We also considered a ROI in an artefact-free region, in order to verify that there's not statisti-

cal difference between the original and the corrected image in an area that doesn't need a correction (see Figure 4.2).

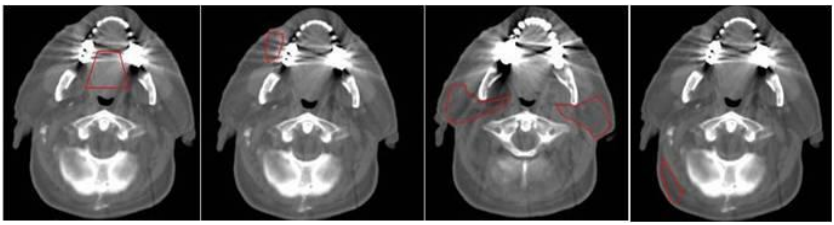

Figure 4.2. Position of the ROIs in the image. From left to right: Art_ROIs, placed near teeth, parotid ROI and artefact-free ROI.

- Results

Figure 4.3 shows the results of the correction method, applied to an exemplificative case: in the left the original image with streaks artefacts and in the right the corrected image. Artefacts are well eliminated and anatomical structures, affected by streaks, become more visible, improving, therefore, the contour delineation of target and OAR.

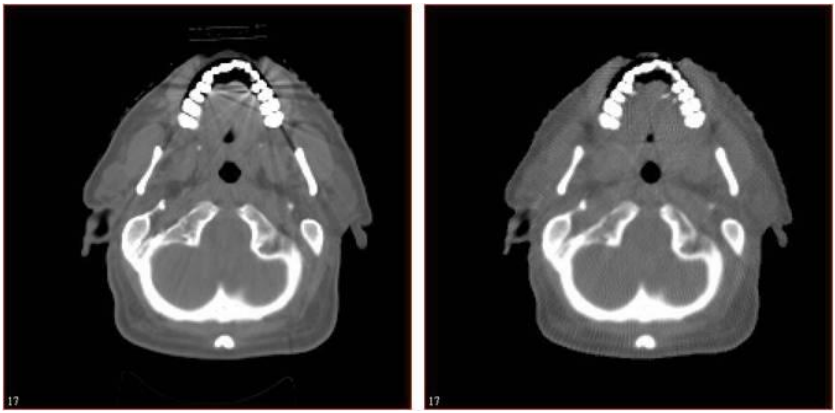

Figure 4.3. Result of the correction method. Left: original image with streaks artefacts; right: corrected image. Evident metal streaks are removed and image quality is improved.

Tables 4.1, 4.2 and 4.3 show the results of the quantitative evaluation: in Art_ROI, standard deviation of intensity is significantly different (Wilcoxon signed rank test, p= 0.005) between original and corrected images. For parotid glands both mean and standard deviation become significantly smaller (Wilcoxon signed rank test, p=0.009 and p=0.005 for mean and standard deviation respectively), confirming improvements in image quality. In artefact-free ROI, no statistical difference between original and corrected image was found (mean intensity value of the original image: -97.26 ± 19.32; mean intensity value of the corrected image: -99.03 ± 21.97; p_value > 0.05).

Table 4.1. Mean intensity and standard deviation (HU units) in Art_ROI.

		Original		***Corrected***	
		mean	std	mean	std
Art_ROI	P1	142.66	118.08	61.15	52.22
		48.66	121.49	33.07	87.94
	P2	97.45	148.80	65.50	82.57
		-7.94	187.46	46.40	65.86
	P3	53.76	74.01	65.83	47.18
		41.89	87.80	16.56	77.67
	P4	68.81	88.11	53.90	55.65
		89.06	79.47	26.36	39.31
	P5	64.69	60.36	60.53	31.01
		105.65	57.83	72.92	45.66
Mean		**70.47**	*102.34*	**50.22**	*58.51*
WILCOXON TEST			*p_value mean= 0.074* *p_value std= 0.005*		

Table 4.2. Mean intensity and standard deviation (HU units) in parotid glands.

		Original		***Corrected***	
		mean	std	mean	std
Parotids	P1	-30.84	32.24	-40.59	30.61
		-81.17	56.47	-94.79	35.93
	P2	-29.69	65.48	-43.84	51.99
		-21.52	67.03	-31.97	55.23
	P3	-34.33	55.85	-43.56	42.03
		-67.74	69.69	-59.60	41.73
	P4	10.40	78.07	-2.43	73.79
		-23.86	47.63	-34.31	36.92
	P5	-18.98	44.50	-29.42	35.23
		-50.11	54.55	-53.18	41.49
Mean		**-34.78**	*57.15*	**-43.37**	*44.49*
WILCOXON TEST			*p_value mean= 0.009* *p_value std= 0.005*		

The significant decrease in mean and standard deviation in the intensity measurements is in agreement with other works (Yazdia *et al* 2005, Bal and Spies 2006), which evidenced the capability of the method of recovering the CT number of the imaged objects; meanwhile, the method can preserve original intensity value in artefact-free regions. These two properties can allow an accurate densitometric analysis.

Table 4.3. Mean intensity and standard deviation (HU units) in artefacts-free ROI.

		Original		***Corrected***	
		mean	std	mean	std
artefacts-free ROI	P1	-97.96	20.60	-110.14	24.17
	P2	-106.72	19.72	-104.28	23.51
	P3	-101.03	16.11	-100.88	18.29
	P4	-85.46	20.64	-79.25	23.81
	P5	-95.11	19.52	-100.58	20.06
Mean		**-97.26**	*19.32*	**-99.03**	*21.97*
WILCOXON TEST		*p_value mean > 0.05* *p_value std > 0.05*			

4.1.3.2. Index description

To perform texture analysis using statistical approach, the image is treated as a 3D surface, where the intensity values are the third dimension of a 2D image. Statistical approach provides the estimation of first order and second order texture parameters. In first order statistical analysis, texture parameters are extracted from the histogram of image intensity; this analysis gives global information about the image without consider the spatial information between pixels. In second order statistics, texture parameters are calculated taking into account spatial correlation between pixels, using the co-occurrence matrix (Ahammer *et al* 2011).

- First-order statistical texture analysis

First order statistical parameters are calculated from the histogram of the intensity of a set of pixels. The first order histogram is defined as:

$$P(i) = \frac{n(i)}{N}; \qquad i = 0,1,2,\dots,L$$

where *n(i)* is the number of pixel with actual gray value of *i*, *L* is the maximal gray value and *N* is the total number of pixel in the considered region.

From the histogram, standard indices can be extracted to describe the properties of the image texture. In this study, the mean gray value μ, the variance σ^2 and the entropy S_1 are computed as:

$$\mu = \sum_{i=0}^{L} iP(i)$$

$$\sigma^2 = \sum_{i=0}^{L} (i-\mu)^2 P(i)$$

$$S_1 = -\sum_{i=0}^{L} P(i) log_2 P(i)$$

High values of variance means an inhomogeneous image with high gray value differences. The entropy is an index of histogram uniformity: the more the value of entropy increases, the more disordered is the gray value distribution.

- Second-order statistical texture analysis

Second order statistical parameters are calculated from the co-occurrence matrix (Haralick *et al* 1973). In this matrix, the entries are the probability of finding a pixel with gray level value of *i* at a distance *d* and angle α from a pixel with a gray level value of *j*. The co-occurrence matrix C is defined as:

$$C_{d,\alpha}(i,j) = \frac{n(i,j)}{N}; \quad i = 0,1,2,\dots,L, \;\; j = 0,1,2,\dots,L$$

where *n(i,j)* is the number of occurrences of pixels with gray level *i* and pixel with gray level *j* at a distance *d* and angle α; *N* is the total number of pixel in the region and *L* is the maximal gray value.

We computed the symmetric co-occurrence matrix for *d*=1 and α=[0°, 45°, 90°, 135°], in order to consider eight-neighborhood of a pixel. The resulting parameters, calculated from each matrix,

were averaged as proposed by (Ahammer *et al* 2011) in order not to emphasize a particular direction.

From the co-occurrence matrix, homogeneity *H* and local entropy S_2 were then computed as follows:

$$H = \sum_{i=0}^{L}\sum_{j=0}^{L}\left(\frac{C(i,j)}{1+(i-j)^2}\right)$$

$$S_2 = -\sum_{i=0}^{L}\sum_{j=0}^{L} C(i,j)log_2C(i,j)$$

These indices were used to characterize spatial patterns of an image; in particular high tissue homogeneity and high organization were featured by high values in H and low values in S_2.

- Fractal dimension

Fractal analysis provides a measure of the complexity and the roughness of a surface, determining the relative amounts of detail or irregularities at different scales. FD of a 2D image ranges between 2 (the topological dimension of a 2D image) and 3 (the topological dimension of a 3D volume), where larger FD indicates rougher image (Peitgen *et al* 1988).

Among the different methods proposed in the literature for FD estimation (Dubuc *et al* 1989, Chaudhuri and Sarkar 1995, Veenland *et al* 1996, Murato and Saito 1999), for this study we adopted the variogram method (Murato and Saito 1999), proven to be the most accurate in FD estimation (Nauta *et al* 2011) and based on the statistical Gaussian modeling of images: FD is estimated by assuming that an image is derived from a fractional Brownian motion (fBm). In fBm, the expected value of the intensity difference between two points is zero but the square of difference is proportional to the distance between the points at a power 2H, where H is the Hurst coefficient. FD is related to H with this relation:

$$FD = n + 1 - H$$

where n is the Euclidean dimension. A common technique for estimating FD, assuming the data was statistically similar to fBm, is provided by the semi-variogram function *γ(h)*, defined as:

$$\gamma(h) = \frac{1}{2N}\sum_{i=1}^{N}(F(x_i) - F(x_i + h))^2$$

where N is the number of points whose lag is *h*. *γ(h)* is related to FD by a power law of the lag given by

$$\gamma(h) = ch^{4-2FD}$$

for a constant *c*. It is then possible to derive FD in the log-log space, by considering the linear slope *m* that the semi-variogram should have (see Figure 4.4):

$$FD = \frac{4 - m}{2}$$

Due to the finite size of the parotid volume, the range of lag for the straight line appearing on the log(γ(h)) versus log(h) is less than 10% of the profile length (only 6 points were considered in the linear regression), as suggested by Murato and Saito (Murato and Saito 1999) (see Figure 4.4). Moreover, the lag *h*=1 was not included in the regression in order to reduce the effects of voxelisation and CT noise.

This method was defined for profiles and can be extended to images by calculating FD of each row and column, averaging them all, and adding one (Nauta *et al* 2011).

The methods were tested for accuracy and precision across a range of FDs and image sizes. More specifically, the performance of each FD method was evaluated with a set of digital image representations of mathematical fractal surfaces known as fractional Brownian surfaces (see Figure 4.5) (Peitgen *et al* 1988), that can model radiologic images more reliably than other synthetic representations (Veenland *et al* 1998). These digital surfaces were generated to have known FDs ranging from 2.1 to 2.9 in steps of 0.1. The implemented semi-variogram method was evidenced to be accurate and precise, in accord to the findings of other works (Nauta *et al* 2011).

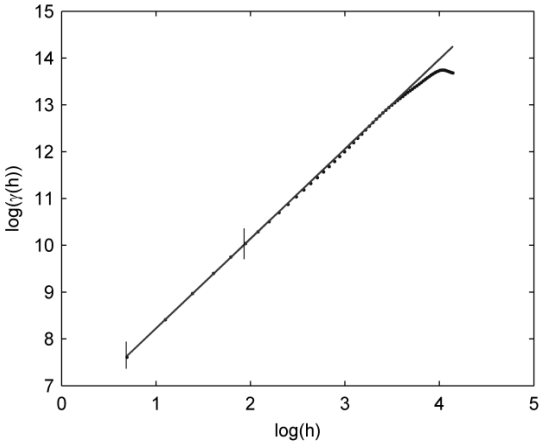

Figure 4.4. Representative plot showing the relationship between the semi-variogram γ(h) and the lag h in log-log space, calculated from a row in a CT slice of our dataset. FD can be derived from the slope of the regression line, considering only 6 points (about 10% of the profile length).

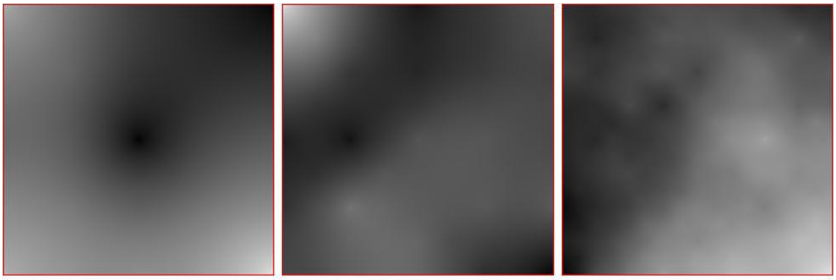

Figure 4.5. Examples of fractional Brownian surfaces represented as digital images, with known FD.

Texture analysis was performed using a 2D approach on each slice of the CT study, within the parotid contours; the textural indices descriptive of each parotid gland were calculated as the median

value between all slices, as proposed by Assefa et al (Assefa *et al* 2010).

4.2. CORRELATION OF MEAN INTENSITY WITH MORPHOLOGICAL, PRE-CLINICAL AND DOSIMETRIC PARAMETERS[3]

The first and simplest structural index giving a synthetic description of parotid function is the mean grey intensity value, linearly related to its density, estimated within the whole volume. The possibility to link deformation with density variation could be very important, being both the glandular volume variation and the relative weight of the fat component likely to be correlated with the glandular secretion capacity. Within the project dealing with the impact of organ deformation during HN IMRT, density changes measured with MVCT or kVCT of a large number of patients were investigated.

4.2.1. Materials and Methods

4.2.1.1. Patient data and imaging procedure

Data of 168 parotid glands of 84 patients from three Institutions treated for different HNC were pooled. Median patient's age was 59 years (range: 29–86 years). Most patients (79/84, 94%) did not undergo upfront surgery; 76/84 (90.5%) patients received chemotherapy (before Radiotherapy: 18; concomitant: 70; both: 12). All patients were treated with IMRT: 38 patients (from one Institution)

[3] Based on Fiorino C, Rizzo G, Scalco E, et al. Density variation of parotid glands during IMRT for head-neck cancer: correlation with treatment and anatomical parameters. Radiotherapy and Oncology, 2012. 104, pp 224-229.

with the Helical Tomotherapy Unit (Hi-Art II), 46 (from two Institutions) with Linac-IMRT, in dynamic or step-shoot modality.

In all Institutes, an inverse planning optimization approach was followed with the goal to deliver P95% of the prescribed dose to P95% of PTV volumes, while keeping the dose as homogeneous as possible and sparing both contro- and omo-lateral parotid glands without compromising PTVs coverage. Different dose-volume constraints and optimization approaches were applied in the different institutions, generating a wide range of parotid DVH shapes.

Parotid deformation was evaluated through images taken at the start and at the end of the treatment. More specifically, in one institute MVCT taken with the Helical Tomotherapy Unit on the first and last day of the treatment were considered (image matrix of 512 x 512 pixels, pixel size of 0.754 x 0.754 mm^2, slice thickness of 4 or 6 mm). In the other two centres, diagnostic images were acquired with multi-slice Helical CT (KVCT) scanners. KVCT images were taken at the first fraction and during the last week of the treatment, using similar protocols (image matrices of 512 x 512 pixels, voxel sizes of 0.977 x 0.977 x 2.5 mm^3 or 1.172 x 1.172 x3mm^3; acquisition parameters: 120 kV; 200 mAs in one Institute, 300 mAs in the other). These KVCTs images were performed as part of a pilot study with the aim of identifying those patients that could take advantage from adaptive re-planning.

The first and second CT of each patient were registered using the FFD algorithm described in the previous chapter and parotid glands spatial correspondence was achieved using the contour propagation method.

4.2.1.2. Quantification of deformation and density variation

The entity of deformation of each voxel belonging to the parotid glands volume, as identified by the manual contours, was assessed by the Jacobian of the deformation field calculated by image

registration, as reported in the previous chapter in terms of Jac_mean.

To overcome the problem of metal artefacts due to dental filling, that can affect the measurement of density values of parotid glands in kVCT images, the NMAR method, previously described, was applied (Meyer *et al* 2010). The assessment of density variation was performed by measuring the mean intensity value (Hounsfield units, HU) and standard deviation within the whole parotid volume delineated by the manual and propagated contours on both the first fraction and the end of treatment images. Density variations were quantified in terms of average HU change between last and first fraction (ΔHU); due to the linear relationship between HU and density in the relatively small range of variation of this study, ΔHU values taken with both kVCT and MVCT may be used for the purpose.

4.2.1.3. Statistical analysis

The correlation between ΔHU and a number of parameters was tested by the Spearman test. The considered variables were: chemotherapy, previous surgery, type of cancer (nasopharynx vs others), PTVs volume, age, prescribed dose, daily dose, initial parotid volume, mean parotid dose, fraction of parotid receiving more than 10,15,20,30,40 Gy (V10–V40), % parotid volume variation, neck half-thickness variation (measured at C2, in the normal neck direction in case of lateral tumor, Δs), weight variation, Jac_mean, % fraction of voxels with Jac < 0.9, 0.8, 0.7, 0.6, 0.5, 0.4, 0.3 (Jac0.9–Jac0.3).

Analyses were repeated when only considering kVCT data, due to the reduced noise concerning density estimate within parotids. A logistic univariate analysis was performed considering the ΔHU larger than the quartile value (-11 HU) as end-point, identifying the largely changing parotids. Best cut-off values of the most predictive continuous variables were assessed by ROC analysis. Stepwise multi-variate analyses were performed taking the most predictive factors ($p < 0.10$) at univariate analysis. The predictive value of the

models was assessed by the area under the ROC curve (AUC). The analyses were repeated for the whole and the kVCT population.

4.2.2. Results

4.2.2.1. Density variation

A summary of ΔHU data in the whole population and in the two MVCT/kVCT subgroups is reported in Table 4.4. ΔHU was <0 in 116/168 parotids (69%); this fraction was larger for kVCT (72/92, 78%). On average, the mean ΔHU was -7.3 (-9.3 for MVCT vs -5.6 for kVCT), corresponding to about 0.20-0.25 HU/fraction. The standard deviation of the distribution of ΔHU is much higher for MVCT than for kVCT patients (24.3 vs 7.4) due to the higher noise of MVCT compared to diagnostic kVCT images.

Table 4.4. Summary statistics of density variations for all parotid glands and for parotids acquired with MVCT or KVCT

	All parotids	**MVCT**	**KVCT**
Number	168	76	92
ΔHU mean	-7.3	-9.3	-5.6
Median	-4.6	-1.9	-5.0
Std	17.1	24.3	7.4
Max	24.0	24.0	13.8
Min	-94.0	-94.0	-27.9
Lower quartile	-11.0	-12.7	-10.5
Higher quartile	1.9	4.5	-1.0
N with ΔHU<0	116	44	72

4.2.2.2. Correlation between density variation and pre-treatment factors

A summary of the results concerning the correlation tests is reported in Table 4.5 (variables with p-value≤0.20). When considering the whole population, the pre-treatment variables mostly corre-

lated with ΔHU were PTV1 volume (p=0.015), % overlap between PTV and parotid (p=0.02), initial parotid volume (p=0.048) and secondarily initial neck thickness (p=0.10), V40 (p=0.13) and age (p=0.11): in particular larger PTV volumes, larger parotids, larger neck thickness and younger age predict a larger decrease of ΔHU. When considering the kVCT group, better correlations were found for initial neck thickness (p=0.03) and age (p=0.13).

4.2.2.3. Modeling large density variations

Logistic analyses taking ΔHU<-11 (quartile value of the whole population) as the end-point were performed for the whole and the kVCT populations: summary of the results are reported in Table 4.6. When considering the univariate analysis, the most predictive variables were the pre-treatment half-thickness of the neck and, much more important, thickness reduction, parotid volume reduction and JVH-based parameters/Jac_mean with this last one being the most predictive. When assessing the best cut-off value from ROC analysis, Jac_mean < 0.68 was the best value: the incidence of parotids with ΔHU < -11 was 18% and 45% below or equal/above the cut-off, respectively (12% vs 48% for kVCT). Stepwise multi-variate analysis showed initial neck half-thickness and Jac_mean as the most predictive independent variables. The predictive value of the models expressed in terms of AUC were 0.683 (CI:0.607–0.752) and 0.776 (CI:0.677–0.856) for all and kVCT, respectively. In Figure 4.6 the plot of the probability that ΔHU<-11 HU is shown for kVCT patients as a function of the initial neck thickness for parotids with large deformation (Jac_mean < 0.68) and with moderate/small deformation (Jac_mean ≥ 0.68).

Table 4.5. Summary of Spearman correlation tests (results presented only for correlations with p-value≤0.20): ΔHU vs pre-treatment parameters for all parotids and parotids acquired with KVCT.

Parameters	All parotids (n=168)		KVCT (n=92)	
	R	p-value	R	p-value
Age	0.12	0.11	0.16	0.13
PTV volume	0.19	0.015	-	-
% overlap PTV-parotid	0.18	0.02	0.21	0.04
Initial parotid volume	0.15	0.05	-	-
Initial neck thickness	-0.13	0.10	-0.22	0.03
V30	0.11	0.19	0.14	0.20
V40	0.12	0.13	-	-
ΔVolume [cc]	0.22	0.004	0.15	0.15
ΔVolume [%]	0.23	0.003	0.23	0.03
Δs [cm]	0.27	0.0005	0.31	0.003
Δs [%]	0.25	0.001	0.27	0.01
Jac_mean	0.22	0.004	0.36	0.0005
Jac0.2	0.21	0.008	-	-
Jac0.3	0.20	0.01	0.23	0.03
Jac0.4	0.18	0.02	0.15	0.15
Jac0.5	0.17	0.03	0.19	0.07
Jac0.6	0.20	0.01	0.38	0.0003
Jac0.7	0.20	0.01	-	-
Jac0.8	-	-	-	-
Jac0.9	0.16	0.04	-	-

Table 4.6. Summary of the results of the uni- and multi-variate logistic analysis (results presented for p≤0.20); end-point: ΔHU<-11 (quartile value of the population). Analyses for all parotids and parotids acquired with KVCT

Parameters	All parotids (n=168)		KVCT (n=92)	
	OR (95% CI)	p-value	OR (95% CI)	p-value
PTV volume	-	-	1.00 (0.99-1.01)	0.11
Initial neck thickness	1.58 (1.00-2.50)	0.05	1.91 (0.96-3.78)	0.06
ΔVolume [cc]	0.91 (0.84-0.98)	0.009	0.92 (0.84-1.01)	0.07
ΔVolume [%]	0.97 (0.94-0.99)	0.005	0.96 (0.92-1.00)	0.03
Δs [cm]	0.25 (0.11-0.58)	0.001	0.27 (0.10-0.77)	0.01
Δs [%]	0.91 (0.86-0.97)	0.003	0.92 (0.86-0.99)	0.03
Jac_mean	1.00 (1.00-1.26)	0.003	1.00 (1.00-1.03)	0.0008
Jac_mean < 0.68	3.76 (1.82-7.76)	0.0004	6.71 (2.39-18.8)	0.0003
Jac0.2	1.02 (1.00-1.03)	0.014	1.04 (1.01-1.06)	0.002
Jac0.3	1.02 (1.01-1.04)	0.036	-	-
Jac0.4	1.03 (1.01-1.04)	0.013	-	-
Best parameters retained in the Multi-variate model:				
Jac_mean < 0.68	3.80 (1.80-7.90)	0.0004	8.00 (2.70-24.2)	0.0002
Initial neck thickness	1.61 (0.99-2.62)	0.05	2.39 (1.07-5.33)	0.03
	AUC: 0.683		AUC: 0.776	

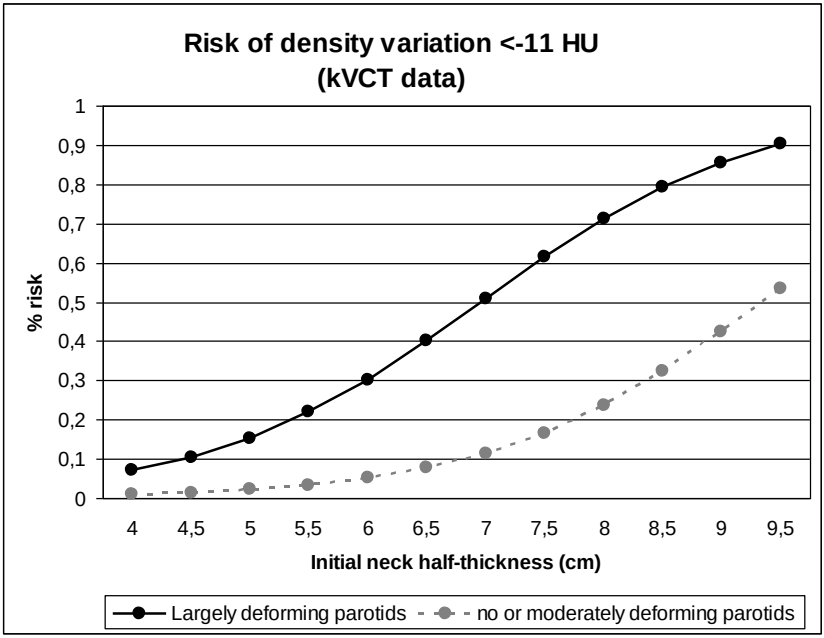

Figure 4.6. Relationship between ΔHU and initial neck thickness for largely deforming (Jac_mean < 0.68) and moderately(minimally deforming (Jac_mean ≥ 0.68) parotids, considering only KVCT data (logistic model: AUC=0.776; p=0.0001)

4.3. DYNAMIC CHARACTERIZATION OF STRUCTURAL MODIFICATIONS AND THEIR CORRELATIONS WITH DOSIMETRIC PARAMETERS

In IGRT, the availability of CT images acquired daily or weekly during the treatment opens the possibility to investigate the dynamic of structural variations in parotid tissue. In particular, texture analysis allows the extraction of various parameters related to different aspects of the spatial tissue organization. Therefore, the

analysis of density changes during RT can be placed beside a more complete characterization performed by texture analysis and considering different time points, in order to study the kinetic of these parameters.

Another critical issue is about the relationship between textural and volumetric variations estimated at the end of treatment and dosimetric and clinical parameters measured before RT; in fact, this can help in understanding the mechanism which can influence structural modifications induced by irradiation.

4.3.1. Materials and Methods

4.3.1.1. Dataset and imaging procedure

37 patients (74 parotid glands) in two different institutions were considered. All patients were treated with IMRT, in dynamic or step-and-shoot modality. CTV2 was defined as the contour including elective node chains, while CTV1 included the gross tumor volume+involved nodes. An expansion of 5 mm was used to define the corresponding PTV volumes. 24 patients (64.9%) received a simultaneous integrated boost approach (SIB), delivering 58.1Gy (1.66 Gy/day) on PTV2 68.25-70Gy (1.95-2 Gy/day) on PTV1 in 35 fractions, or delivering 54Gy (1.8 Gy/day) on PTV2 66Gy (2.2 Gy/day) on PTV1 in 30 fractions. On the other hand, a sequential approach was used for 35.1% patients delivering 50.4-64.8Gy (1.2-1.8 Gy/day) on PTV2 and 50.4-78Gy (1.66-1.8 Gy/day) on PTV1 in number of fractions ranging from 36 to 43.

CT images were acquired before RT (CT1), at half treatment (CT_half) and after RT (CT_last), using the same acquisition protocols: image matrices of 512x512 pixels, voxel size of 0.9766x0.9766x2.5 mm3 or 1.217x1.217x3 mm3 and acquisition parameters of 120 kV and 300 mAs.

Contours of parotid glands were manually delineated by an expert on each CT slice of CT1 and then they were automatically propagated on CT_half and CT_last using the contour propagation algorithm described in Chapter 3.1. Within this parotid contours,

textural features previously described (μ, σ^2, S_1, H, S_2, FD)and volume (V) were extracted in each CT study.

4.3.1.2. Dynamic analysis

Differences between textural parameters and volume in CT1 and CT_last, CT1 and CT_half, CT_half and CT_last were tested using t-test statistics for each index, to evaluate time trend variations. Moreover, in order to study the relationship between structural and morphological changes, correlations between total variations measured at the end of therapy for each parameter resulted significant after t-test were assessed with Pearson's coefficient.

4.3.1.3. Correlations with clinical and dosimetric parameters

Pearson correlation between the final variation (CT_last-CT1) of each parameter and the same dosimetric and clinical parameters listed in paragraph 2.1.3 was performed. Then, a stepwise multivariate logistic analysis was applied using as end-point the variation of volume or textural index at the end of RT, dichotomized based on the median value of population, and as variables the parameters with significant Pearson's coefficient. Finally, AUC value was calculated using ROC curve estimated from results of multivariate analysis.

4.3.2. Results

4.3.2.1. Dynamic analysis

In Tables 4.7 and 4.8 the average values of each parameter were reported. T-test revealed that no significant differences were present for S_1 and H; differences were significant for the other parameters (μ, σ^2, S_2, FD and V) during the whole treatment ($p<0.001$) and in the first half ($p<0.001$), while in the second half a significant variation was found for S_2, V ($p<0.001$) and FD ($p<0.01$), but no significant difference was found for μ. A general decrease was measured ($\Delta\mu$=-4.7 HU and -5.3 HU, ΔS_2=-0.15 and -0.27, ΔFD=-0.02 and -

0.03, ΔV=-3.5 cm^3 and -5.1 cm^3, in the first half and in the whole treatment respectively), with different time trends (see Figure 4.7).

Table 4.7. Textural features and volume measured in CT1, CT_half and CT_last. Values are represented as mean and standard deviation among the population.

	CT1		**CT_half**		**CT_last**	
	mean	*(std)*	**mean**	*(std)*	**mean**	*(std)*
Mean (μ) [HU]	**-8.62**	*(21.38)*	**-13.31**	*(23.17)*	**-13.9**	*(23.58)*
Variance (σ^2)	**817**	*(315)*	**889**	*(322)*	**934**	*(344)*
Global entropy (S_1)	**8.41**	*(1.26)*	**8.34**	*(1.28)*	**8.43**	*(1.29)*
Homogeneity (H)	**0.247**	*(0.028)*	**0.246**	*(0.027)*	**0.249**	*(0.031)*
Local entropy (S_2)	**8.41**	*(0.43)*	**8.26**	*(0.41)*	**8.14**	*(0.48)*
Fractal dimension (FD)	**2.591**	*(0.04)*	**2.571**	*(0.05)*	**2.557**	*(0.05)*
Volume (V) [cm^3]	**29.0**	*(10.5)*	**25.4**	*(8.3)*	**23.9**	*(8.5)*

Table 4.8. Differences between every time point for each textural and volume index and their significance estimated with t-test. Values are represented as mean and standard deviation among the population.

	CT_last-CT1		**CT_half-CT1**		**CT_last-CT_half**	
	mean	*(std)*	**mean**	*(std)*	**mean**	*(std)*
Mean (μ) [HU]	** **-5.28**	*(7.43)*	** **-4.69**	*(5.86)*	**-0.59**	*(5.34)*
Variance (σ^2)	** **117**	*(240)*	* **72**	*(224)*	* **46**	*(175)*
Global entropy (S_1)	**0.02**	*(0.83)*	**-0.06**	*(0.91)*	**0.08**	*(0.89)*
Homogeneity (H)	**0.002**	*(0.02)*	**-0.001**	*(0.01)*	**0.002**	*(0.018)*
Local entropy (S_2)	** **-0.27**	*(0.26)*	** **-0.15**	*(0.20)*	** **-0.12**	*(0.24)*
Fractal dimension (FD)	** **-0.03**	*(0.04)*	** **-0.02**	*(0.04)*	** **-0.01**	*(0.04)*
Volume (V) [cm^3]	** **-5.1**	*(4.8)*	** **-3.5**	*(4.0)*	** **-1.5**	*(3.3)*

* $p<0.05$
** $p<0.001$

A large decrease of μ in the first half of RT, followed by a plateau in the second half, was found. The different behavior shown by mean intensity changes (μ) with respect to S_2 and FD is likely to be related to the rapid loss of water excretion in the first days after irradiation.

For the correlation analysis we considered only μ, S_2, FD and V, as the indexes that significantly varied during RT; variance was excluded, since its variation was probably related to noise in image histogram. Strong linear correlations were found between ΔV-$\Delta\mu$, ΔV-ΔS_2 and $\Delta\mu$-ΔS_2 (see Table 4.9), indicating a relationship between structural and morphological variations, as expected.

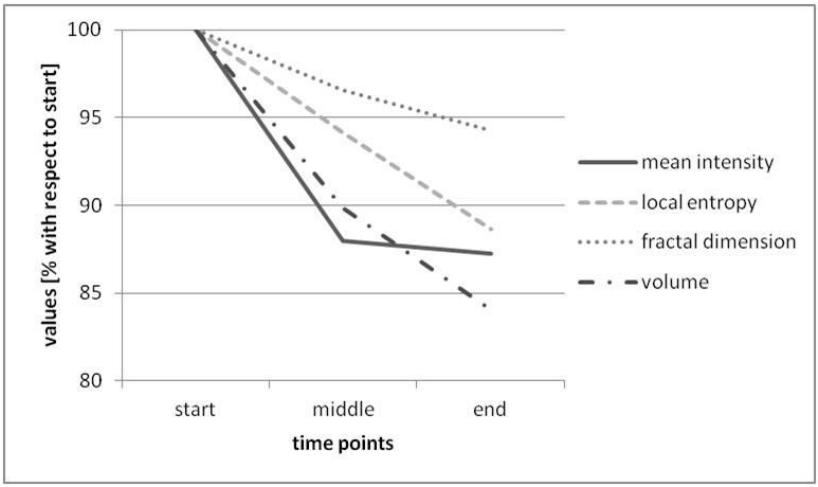

Figure 4.7. Variations of mean intensity, local entropy, fractal dimension and volume during RT, considering CT images acquired at the beginning, half and end of therapy.

4.3.2.2. Correlations with clinical and dosimetric parameters

The final variation of textural features ($\Delta\mu$_total, ΔS_2_total, ΔFD_total) has shown little correlation with dosimetric and preclinical parameters, with respect to the volume variation (see Table 4.10). In particular, ΔS_2_total was not significantly correlated with any index. This is probably due to the limited number of samples or because there is no evident relationship between dosimetric condition or the initial anatomical configuration and the structural variation described by these indexes.

Stepwise multivariate analysis was then performed using all these significant parameters for each structural and morphological variation. As expected, no significant regression model was found for local entropy and fractal dimension; mean intensity variation was explained by both PTV volume and the initial neck thickness (the model is different with respect to that found in the previous chapter because in this case we considered only pre-treatment factors, thus jac-mean was excluded), while volume variation was ex-

plained by the initial parotid volume and V20 (see Table 4.11). The first model has an almost random classification power (AUC=0.565), while the volume variation model reached a high value (AUC=0.878).

Table 4.9. Results of Pearson correlation analysis between variations of each parameter during the whole treatment. Pearson coefficient and significance are reported.

	ΔS_2_total	**ΔFD_total**	**ΔV_total**
Δμ_total	0.309**	0.215	0.405**
ΔS_2_total		0.113	0.591**
ΔFD_total			-0.078

** p<0.001

Table 4.10. Pearson's correlation coefficient between dosimetric and clinical parameters and the final variation of mean intensity, local entropy, fractal dimension and volume. Data presented only for correlation with p-value<0.05.

Parameters	**Δμ_total**	**ΔS_2_total**	**ΔFD_total**	**ΔV_total**
PTV volume	0.230*	-	-	-
% overlap PTV-parotid	-	-	0.249*	-0.220*
Initial parotid volume	-	-	0.269*	-0.593**
Initial neck thickness	-0.446**	-	-	-0.557**
V10	-	-	-	-0.313**
V15	-	-	-	-0.259*
V20	-	-	-	-0.284*
V40	-	-	-	-0.254*

* p<0.05
** p<0.001

Table 4.11. Multivariate regression models for mean intensity and volume variation after RT and their AUC values estimated by ROC curve.

Multivariate model for Δμ_total		
	OR (95% CI)	**p-value**
PTV volume	0.991 (0.983-0.999)	0.031
Initial neck thickness	2.3 (1.05-5.03)	0.037
	AUC: 0.565	

Multivariate model for ΔV_total		
	OR (95% CI)	**p-value**
Initial parotid volume	1.00 (1.00-1.00)	<0.001
V20	1.087 (1.029-1.148)	0.003
	AUC: 0.878	

4.4. EARLY PREDICTION OF PAROTID SHRINKAGE USING TEXTURAL PARAMETERS[4]

As already shown, mean CT intensity of parotid glands can be used as a functional descriptor of the parotid behavior after RT, strictly related to the anatomical deformation, and dependent from some pre-clinical and dosimetric conditions. Another important issue in studying the effect of RT on OAR is the capability of early predict those subjects that will experiment worse side effects and thus that can mostly benefit of a replanning strategy. Considering this intent, in this paragraph I present some preliminary results about the ability of textural features in predicting parotid shrinkage measured at the end of treatment, as an index which is known to be

[4] Based on Scalco E, Fiorino C, Cattaneo GM, Sanguineti G, Rizzo G. Texture analysis for the assessment of structural changes in parotid glands induced by Radiotherapy. Radiotherapy and Oncology, 2013. In press

related to the presence of acute toxicity, as reported in previous works (Teshima *et al* 2010) and extensively discussed in Chapter 2. For this study we considered the variations in textural parameters in the first two weeks of treatment, in order to assess if early changes in parotid structure could be correlated with later morphological variations.

4.4.1. Materials and Methods

4.4.1.1. Dataset and imaging procedure

The study included 21 patients treated with IMRT for naso-pharyngeal tumors in 6-8 weeks (more details can be found in Table 4.12), without involvement of parotid glands. For each patient, CT images were acquired on the first, second and last week of RT treatment (CT1, CT2 and CTlast, respectively), using the same image acquisition protocols: image matrices of 512x512 pixels, voxel size of 1.217x1.217x3 mm^3 and acquisition parameters of 120 kV and 300 mAs, in order to provide similar image quality.

The contours of the 42 parotids were delineated on CT1 by a single observer, and were automatically propagated on CT2 and CTlast using the contour propagation algorithm. The textural features described in Paragraph 1.3 (μ, σ^2, S_1, S_2, H and FD) and mean volume V were extracted for each CT study within the parotid region.

4.4.1.2. Statistical analysis.

In order to individuate textural descriptors that varied significantly for each subject during RT (thereby adequately characterizing individual structural modifications occurring during the treatment) non-parametric Wilcoxon signed-rank test statistics were performed between each textural parameter, averaged between the two parotid glands and calculated on CT1 and CT2, and CT1and CTlast. The significance of parotid volume variation (ΔV) during RT was also assessed with the same statistics.

Table 4.12. Summary of patients data.

Patients		21
Parotids		42
Sex	Male	19
	Female	2
Age	Median	54
	Mean	56
	Range	40-72
Tumore type	Nasopharynx	21
Surgery		0
Chemotherapy		21
(concomitant)	%	100
SIB		21
	%	100
Dose Range PTV1	Total	68.25-70 Gy
	Per fraction	1.95-2 Gy/fr
Dose Range PTV2	Total	58.1 Gy
	Per fraction	1.66 Gy/fr

In order to evaluate whether an early variation of these parameters can predict the final parotid shrinkage, a second analysis was carried out. For those parameters whose variations in the first two weeks proved significant, Fisher's linear discriminant function analysis (Fisher 1936) was applied on the 42 parotids. This analysis can classify single data with respect to *a priori* defined groups, based on the amount of parotid volume variation after RT, considering that significant shrinkage may be associated with subjects who could benefit from re-planning. A median value of ΔV (ΔV_{med}) was calculated, and parotids with $\Delta V > \Delta V_{med}$ were included in the first group (positive results); those with $\Delta V < \Delta V_{med}$ were included in the second group (negative results). The "leaving-one-out" technique was chosen to evaluate accuracy of classification (Gose *et al* 1996). For each index or combination of indices, sensitivity (Se, probability of a positive result given that the parotid shrank), specificity (Sp,

probability of a negative result given that the parotid did not shrink) and accuracy (Acc, percentage of correct classifications) of classification were calculated.

All statistical analyses were performed using SPSS package for Windows (version 16.0, SPSS Inc, Chicago, USA)

4.4.2. Results

Wilcoxon signed-rank test revealed that S_1 and H did not vary significantly during RT, indicating that these indices are less sensitive to parotid variations; on the contrary, a significant decrease was found for μ, S_2, FD and V and a significant increase was found for σ^2 at the end of RT (Table 4.13). The variations of these textural features and volume remained significant also in the first two weeks for μ and FD. The resulting decrease in these textural parameters during the treatment indicates a general decrease of complexity of parotid structure; moreover, the significant variation in the first two weeks suggests a dynamic variation process causing structural and anatomical modifications, starting at the beginning of RT.

Classification of the 42 parotid glands estimated by discriminant analysis with different combinations of parameters is presented in Table 4.14. Among single parameters, the most powerful predictors were V and μ (Acc=66.7%), followed by FD (Acc=50%). Considering the multi-parametric analysis, the best results (Acc=71.4%) were achieved by the combinations of FD and V, and the combination of all considered indices. This result indicates that the combination of multiple factors permitted a better classification than a single index, and, in particular, the use of FD in addition to V achieved the best classification, not improved when μ were included.

Table 4.13 - Textural parameters and volume of the first, second and last week of RT, averaged among subjects. Data presented as median and median of the absolute deviations from the median value (mad).

	CT1	CT2	CTlast	Delta values CT2-CT1	Delta values CTlast-CT1
Mean (μ) [HU]	**-10.3** *(24.5)*	**-10.4** *(25.7)*	**-10.8** *(27.1)*	[a] **-1.7** *(3.6)*	[a] **-3.8** *(6.6)*
Variance (σ^2) [HU]	**862** *(309)*	**1007** *(283)*	**1180** *(312)*	**60** *(150)*	[a]**76** *(198)*
Entropy (S_1)	**8.09** *(1.07)*	**8.45** *(1.11)*	**7.98** *(1.06)*	**0.15** *(0.51)*	**-0.16** *(0.53)*
Homogeneity (H)	**0.25** *(0.03)*	**0.24** *(0.03)*	**0.24** *(0.03)*	**-0.00** *(0.01)*	**-0.00** *(0.01)*
Entropy (S_2)	**8.35** *(0.41)*	**8.26** *(0.42)*	**8.07** *(0.42)*	**-0.06** *(0.10)*	[c] **-0.30** *(0.18)*
Fractal Dimension (FD)	**2.594** *(0.06)*	**2.590** *(0.07)*	**2.585** *(0.06)*	[b] **-0.016** *(0.02)*	[b] **-0.021** *(0.02)*
Volume (V) [cm^3]	**33.0** *(11)*	**31.3** *(11)*	**26.0** *(9)*	[b] **-1.7** *(2.0)*	[c] **-6.6** *(3.5)*

[a]= p-value<0.05
[b]= p-value<0.01
[c]=p-value<0.001

Table 4.14 - Classification of 42 parotid glands based on volume variation at the end of RT and estimated by Fisher's linear discriminant function analysis, using different combinations of variables, calculated as variations in the first week of RT. Number of correctly and incorrectly classified data, sensitivity (Se), specificity (Sp) and accuracy (Acc) are reported.

Parameters (variations in the first 2 weeks)	Correct classifications	Incorrect classifications	Se	Sp	Acc [%]
V	28	14	0.67	0.67	66.7
FD	21	21	0.50	0.50	50
μ	28	14	0.67	0.67	66.7
V, μ	28	14	0.67	0.67	66.7
V, FD	30	12	0.71	0.71	71.4
FD, μ	26	16	0.63	0.61	61.9
V, FD, μ	30	12	0.71	0.71	71.4

4.5. RELATIONSHIP BETWEEN STRUCTURAL INDEXES AND XEROSTOMIA

The last step of this project was to evaluate possible correlations between the found structural variations and the clinical outcome. This aspect can help in understanding the clinical impact of image-based analysis in head and neck RT and in finding possible patients which can better benefit of a re-planning of dose delivery during treatment, based on the prediction of RT side effects. As reported in Chapter 2.2, only a recent work studied the relationship between volume decrease and acute toxicity in salivary glands (Teshima *et al* 2010); therefore, a confirmation of these findings, and also the extension of this evaluation to structural indexes, should be of great interest.

Starting from the results achieved in the previous paragraph (early prediction of parotid shrinkage considering textural variations in the first two weeks), in this paragraph I present some preliminary results about the possible correlations of textural features variations with acute xerostomia.

4.5.1. Materials and methods

4.5.1.1. Dataset, imaging procedure and features extraction

The same dataset and the same imaging procedure described in the previous paragraph was considered in this work: the study included 21 patients treated with IMRT, and for each patient CT images were acquired during each week of treatment (CT1, CT2, CT3, ... and CTlast). Parotid contours were manually delineated on the first CT and then automatically propagated on the other CT studies.

Significant textural features (μ, S_2, FD) and volume were extracted within each parotid volume and differences between CT1-CT2 were calculated. The time interval between CT varied from patients to patient; then, in order to compare homogenous information, the rate of variation was calculated for volume [mm^3/day] (rΔV), mean intensity [HU/day] (rΔμ), local entropy (rΔS_2) and fractal dimension (rΔFD) for the first two weeks of treatment.

4.5.1.2. Measure of parotid glands toxicity

CTC-based (CTCv.3.0) prospective assessment of xerostomia was performed weekly throughout the entire treatment. For each patient, the peak value and the mean value of the xerostomia score were considered and the correlation with morphological and structural variations were studied. The mean score was chosen as a robust longitudinally assessed score depicting both severity and persistence of symptoms (Vásquez Osorio *et al* 2008, Gulliford *et al* 2010).

4.5.1.3. Statistical analysis

The correlation between early parotid gland variations in the first two weeks of RT and xerostomia (both peak and mean scores) was investigated. Maximum, minimum and average $r\Delta\mu$, $r\Delta S_2$, $r\Delta FD$ and $r\Delta V$ of the two parotid glands were separately considered for each patient. By dividing the population based on the median value of the mean acute xerostomia (1.57), the Mann-Whitney test was used to evaluate the difference between the two groups. A logistic uni-variate analysis was performed, taking as end-point a mean xerostomia greater than 1.57; a ROC curve was utilized to evaluate the predictive value of the model. Finally the probability risk of experiencing mean xerostomia ≥ 1.57 vs early $r\Delta\mu$ was evaluated.

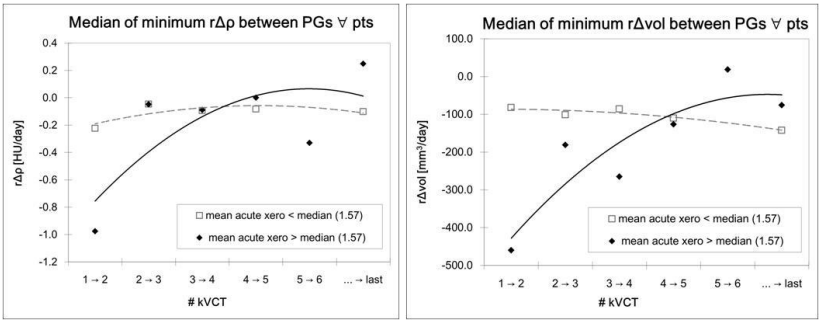

Figure 4.8. Mean rates of density ($r\Delta\rho$[HU/day]) and volume ($r\Delta$vol[mm^3/day]) variations calculated on parotid glands versus the kVCT number, divided based on the median value of the mean xerostomia during treatment (cubic fit). Density/volume variations refer to the minimum value between the two parotid glands for each patient.

4.5.2. Results

No correlation was found between features variations and peak toxicity during treatment. Instead, a clear correlation was found between early changes of volume and density (referred to the minimum, i.e. the lowest value between the two PGs, corresponding therefore to the larger shrinkage and density decrease) and

mean xerostomia score. A significant difference for both the Δμ and ΔV was found when splitting the population in two groups according to the median value of the mean xerostomia score (1.57). On the contrary, no significant results were found for local entropy and fractal dimension.

Considering rΔV and rΔμ, as the only parameters presenting significant correlations, and taking as end-point a mean xerostomia score during treatment ≥ 1.57, the logistic uni-variate analysis results in an OR=0.15 for Δμ (p=0.02) and OR=0.10 for ΔV (p=0.04) (Table 4.15). A ROC curve analysis shows values for AUC of 0.74 (p=0.02) and 0.77 (p=0.01) for Δμ and ΔV, respectively.

Table 4.15. Mann-Whitney test, logistic multi-variate analysis (MVA) and ROC curve for the population. The median value on the population of the mean xerostomia during treatment is 1.57. As end-point for the MVA a mean xerostomia ≥ 1.57 was considered.

		rΔρ [HU/day] 1→2		**rΔV [mm^3/day] 1→2**	
		mean xero ≥ 1.57	**mean xero < 1.57**	**mean xero ≥ 1.57**	**mean xero < 1.57**
Mann-Whitney test	**Median**	-0.98	-0.22	-455	-127
	95%CI	-1.37 to -0.43	-0.95 to 0.09	-970 to -216	-550 to 19
	p-value	0.05		0.03	
Logistic analysis	**OR**	0.15		0.10	
	CI 95%	0.03 to 0.93		0.99 to 1.00	
	p	0.02		0.04	
ROC curve	**AUC**	0.74		0.77	
	95%CI	0.52 to 0.90		0.56 to 0.91	
	p	0.02		0.01	
	Best Cut-Off	-0.49		-378	

Figure 4.8 shows that the group with a mean xerostomia ≥ 1.57 has a larger rΔρ and rΔvol during the first part of treatment, while it is almost unchanged at the end (or during the second half of treatment); on the other hand, patients with low xerostomia mean scores show almost constant values for both rΔρ and rΔvol during the entire course of treatment. Finally, Figure 4.9 shows the probability risk of experiencing a mean xerostomia ≥ 1.57 versus rΔρ. The dashed line indicates the best cut-off value of the ROC curve (-0.49, Table 4.15).

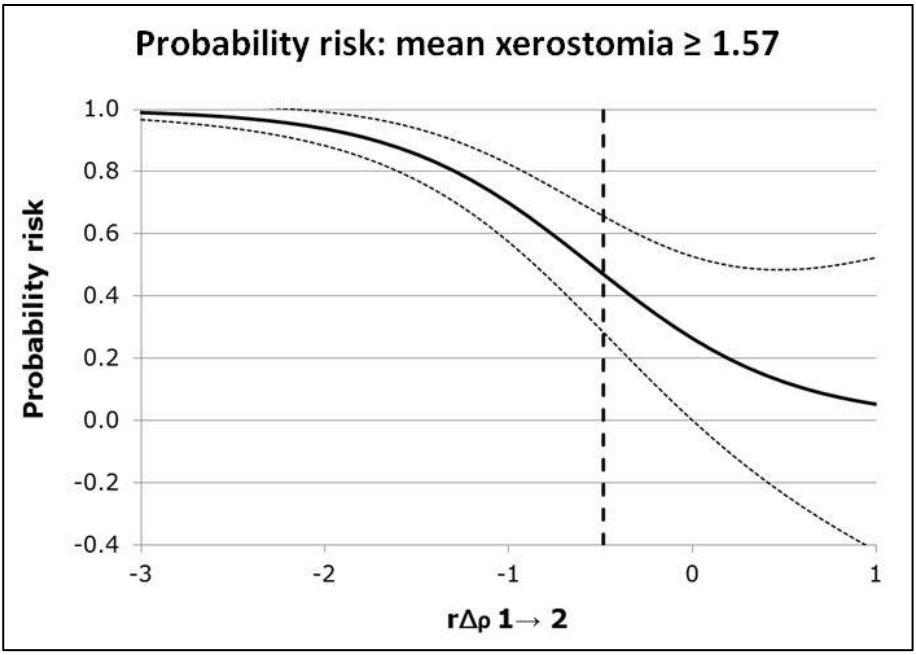

Figure 4.9. Probability risk (95%CI) of mean xerostomia ≥ 1.57 (median value) vs early density variation (rΔρ1→2). The dashed line indicates the best cut-off value (-0.49, Table 4.15) of rΔρ. Density/volume variations refer to the minimum value between the two parotid glands for each patient.

Chapter 5

Discussion

This PhD project was aimed to evaluate the effects of radiotherapy on parotid glands by extracting CT-based indices able to characterize geometric and structural properties of parotid tissue. Anatomical variations, in terms of volume changes and local deformations, were quantified by using an image registration method expressly validated, while structural modifications were evaluated by applying texture analysis to CT images. All these parameters were correlated with dosimetric and pre-clinical features and with the clinical outcome, in order to assess their relationship with RT plans and their predictive power of the acute toxicity level.

In this chapter the discussion of all the presented results is reported, focusing on the evaluation of image registration accuracy (Faggiano *et al* 2011), on the relationship between dose-volume parameters and jacobian index measured after the end of RT, on the correlation between density variations and jacobian (Fiorino *et al* 2012), on the structural characterization of parotid tissue through texture analysis and its ability in early predicting parotid shrinkage (Scalco *et al* 2013). Finally, the relationship between CT-based parameters and acute toxicity is discussed based on the preliminary results achieved.

5.1. IMAGE ANALYSIS METHODS

5.1.1. Accuracy of the image registration and contour propagation method

In RT it is essential to follow anatomical variations of organs of interest and recontouring is thus required; however, especially in the case of MVCT images, characterized by higher noise level and lower soft-tissue contrast with respect to kVCT images, this is a critical issue, since a high inter-observer contour variability is present, as demonstrated in an earlier study on prostate contours (Song *et al* 2006). Therefore, it is important to have a good contour propagation method to help the observers as well as to save time in recontouring.

According to these findings, also in the case of parotid gland contours, our results, presented in Chapter 3.1, on inter-observer variability showed low variability in kVCT where operators are always similar (DSC index always greater than 0.81) and an increased significant variability in MVCT delineations (DSC significantly different from kVCT DSC and p= 0.018 in Anova tests on parotid volumes comparisons). In particular, the major difficulties in contouring on MVCT scans are found for the identification of medial border of the deep lobe because of parotid similarity with surrounding soft-tissues. On the other hand, only the external part of the parotids is known to be subject to strong shrinkage during the treatment, and this portion can be clearly detected also with MVCT, so that the higher uncertainty in the definition of the medial border has a minor clinical relevance (Broggi *et al* 2010, Duma *et al* 2010).

Comparisons between automatic performance and inter-observer variability revealed that the automatic method, which was never significantly different from the manual contours, acts like an observer: in particular, the 3D accuracy analysis showed that no significant difference between automatic and manual contours was present for volumes (Tukey test), COM (Centre Of Mass) distances (Anova test) and DSC (Dice Similarity Coefficient) indices (Wilcoxon

signed rank test). The 2D analysis confirmed that inter-manual comparisons were not significantly different from automatic-to-manual comparisons (p-values > 0.05 for both ASD (Average Symmetric Distance) and MSD (Maximum Symmetric Distance) between contours). Also in absolute terms, differences between manual-to-manual and automatic-to-manual average ASD and MSD were very small (-0.09 mm for ASD and +0.02 for MSD). These findings suggest that our method can successfully substitute manual contouring on MVCT.

Considering HN RT applications, contour propagation methods were often studied applied to kVCT images (Wang *et al* 2008, Zhang *et al* 2007). In particular, Wang et al (Wang *et al* 2008) proposed an auto-propagation method from the planning kVCT to the daily kVCT that maps binary images generated from planning manual contours using a 3D vector deformation map obtained by Demons deformable image registration. This auto-mapping procedure produced small islands, holes and irregular boundaries on the propagated binary images and authors proposed a contour smoothing and modification procedure to correct them. This approach was validated on 8 head-and-neck, 9 lung and 1 prostate cancer patients comparing automatically generated contours with contours manually delineated by one observer using DSC index and the mean absolute surface-to-surface distance. In another work, Zhang et al (Zhang *et al* 2007) used the planning image as the moving image and the daily kVCT image as the fixed image, in a variational-based deformable registration to prevent artefacts (note that in this way the deformation map is not informative about the deformation occurred in patient during the course of therapy). They validated the algorithm using the same indices of (Wang *et al* 2008), on a total of 32 head-and-neck images. Because of the different signal-to-noise ratio and resolution of kVCT images with respect to MVCT images, results of our proposed method cannot be directly compared with these two works.

For a comparison of our results with other works present in literature, only Lee et al (Lee *et al* 2008) applied a contour propaga-

tion method on MVCT images to evaluate parotid glands changes after Tomotherapy. Their method deformed a 3D surface mesh constructed from manually drawn planning contours by a 3D vector deformation map obtained by a variational deformable approach (Lu *et al* 2006). With this approach they avoided the creation of holes inside the object, thus obtaining contours which were reasonable in shape and location and able to represent the anatomical changes of parotid glands. However, a post-processing procedure was required, since automatic contours presented an irregular surface and needed a smoothing. The validation was carried out by visual inspection and by comparison with manual uncertainty evaluated by two manual experts in terms of volume and COM distance. As in our work, authors concluded that automatic uncertainties were similar to manual.

Unlike the before mentioned classical methods, the main advantages of our contour propagation method are the smoothness of the obtained contours, that do not need post-processing adjustments, and the compact representation of the deformation that could be defined by a small number of control points. For example, the information about deformation field of an image of (240 x 240 x 32) voxels is generally stored in a (240 x 240 x 32 x 3) vector matrix, with a standard approach; with our method, the same deformation field calculated on a grid of about 10 mm is contained in a (27 x 27 x 14 x 3) matrix. This characteristic is very useful especially in radiotherapy applications where usually every patient study requires up to 30 deformation fields to be computed and stored. Moreover the information contained in the control point displacement matrix is a volumetric information that covers the entire image and that could produce the re-contouring of many objects at the same time. Our mesh generation and deformation method, once control point displacements are known, is very fast and it could be easily used in retrospective studies of different organs deformation and analysis.

The contour propagation method was associated to the FFD method based on B-spline in order to estimate the deformation field from one image to another. A drawback of the B-spline regis-

tration approach is the relatively high computation time (a typical HN registration takes approximately 15 minutes on a 2.26 GHz Intel(R) Xeon(R) processor, with 6 GB RAM). For this reason this approach could be an optimal method to perform retrospective studies and advanced geometric analysis about regions more involved in deformation (Vásquez Osorio *et al* 2008), but in the present form it is not suitable for fast re-contouring in real-time adaptive radiotherapy. Future works will be addressed to speed up the method by adopting a faster registration method (Bondar *et al* 2010, Paquin *et al* 2009) or by optimizing the here proposed registration procedure.

5.1.2. Quantification of deformation with jacobian index

HNC patients are known to be subject to significant anatomy modifications resulting from both tumor response and changes in normal tissues as a consequence of acute reactions, including weight loss. As suggested by several authors (Lee *et al* 2008, Vásquez Osorio *et al* 2008, Wu *et al* 2009, Wang *et al* 2009, Han *et al* 2008), all the observed anatomic changes may cause significant dosimetric effects when highly tailored dose distributions are delivered; in particular, parotid volume reduction and medial migration can lead to the delivery of an higher parotid dose compared to the planned one (see Chapter 2.2).

The quantification of deformation described in Chapter 3.2 had the primary aim of assessing pre-treatment predictors of parotid shrinkage with the potential to better guide planning optimization and to select patients that could significant take advantage from adaptive strategies. Compared to other investigations where anatomical variations were estimated in terms of volume variation or in terms of position differences, in this chapter parotid deformations were quantified by using the jacobian of the deformation field of the elastic registration. This simple and intuitive method, able to condense the information dealing with single voxel deformation in one number, is not novel; in fact, the Jacobian has been suggested to quantitatively assess local changes of pulmonary func-

tions during radiotherapy (Christensen *et al* 2007, Ding *et al* 2010), by considering expansion/compression of lung voxels during normal breathing. In addition, the introduction in a previous study (Fiorino *et al* 2011) of the Jacobian Volume Histogram (JVH), which acts as the DVH and permits to condense the information pattern into a single curve, provides the possibility to quantify the deformation as an "organ-effect". JVH-based parameters were found to add information compared to the mere volume reduction, enhancing the correlation between the type of the deformation and pre-treatment variables. In particular the correlations with Jac_mean were enhanced for parotid mean dose and V10.

Similarly to a previous study (Broggi *et al* 2010), we found that patient's age was the most predictive clinical variable of parotid shrinkage. It was confirmed that the parotid shrinkage is more relevant in younger patients, suggesting that massive apoptosis, leakage of granules and subsequent lysis of acinar cells, responsible for the acute radiation-induced function loss of salivary glands, could be more active for younger patients (Konings *et al* 2005). The low sensitivity of old patients compared to the younger ones could also be correlated to possible interactions with drugs (i.e. anti –depressive, anti-hypertensive) mostly used by older patients and/or a likely different level of parotid hydration between old and young patients.

The Jacobian-based method showed a clear correlation between parotid shrinkage and dosimetric variables; in particular, by considering the multivariate analysis taking also into account the DVH grouping, a significant correlation between parotid shrinkage and the planned DVH shape is evident, both in the low dose region (V10–V15) and in the medium dose region (V40), also if the low–dose bath effect seems the predominant one. In according to other papers (Bussels *et al* 2004, van Luijk *et al* 2009, Jeraj *et al* 2010) in which the low dose bath has been reported as a potentially detrimental factor when considering salivary function impairment, also in our study V10 and V15 were found as the dosimetric pre-treatment parameters more significantly correlated to parotid shrinkage. Although parotid shrinkage mainly involved the external

portion of the glands, our results do not exclude that the fraction of parotid receiving higher doses (i.e. V40 Gy) could play some role; neither a possible interaction between the internal parotid gland region irradiated at medium-high dose and the external region reactions could be excluded. In any case, our results confirm the importance of an accurate planning optimization approach in order to minimize as much as possible the parotids DVH in the whole dose range, including the fraction of parotid receiving doses as low as 10Gy (Vásquez Osorio *et al* 2008, Wang *et al* 2009).

The significant correlation found with the percentage body thickness variation, when not only including pre-treatment variables in the MVA analysis, seems to indirectly suggest that parotid deformation may be only partial explained by the planned dose distribution. A subjective patient's radiation reaction should be also considered.

In conclusion, the clear correlation between parotid deformation and clinical/geometrical/dosimetric parameters found in this study together with the possibility to use quantitative image-based scoring information from images taken during and after radiotherapy for measuring the radiation-induced damage (Jeraj *et al* 2010, Bayouth *et al* 2011) seems to be very promising in predicting individual reactions and possibly in adapting the treatment, primarily to reduce early and/or late toxicity.

5.1.3. Correlation of mean intensity with morphological, preclinical and dosimetric parameters

Following the considerations previously discussed about the possibility of using quantitative information from images taken during (and after) RT as image-based scores of toxicity (Jeraj *et al* 2010, Bayouth *et al* 2011), in Chapter 4.2 we extended these analysis by measuring parotid glands density from CT images. The general purpose was thus to predict individual reactions and possibly adapt the treatment, primarily to reduce toxicity, based on the correlation be-

tween pre-treatment parameters and functional and anatomical variations after RT.

The paradigmatic scenario of parotid morphological and functional changes measured by imaging techniques is very intriguing; as deeply reported in the previous sections, the largely visible effect of parotid shrinkage could be used as a surrogate of radiation-induced early reactions (Broggi *et al* 2010, Vásquez Osorio *et al* 2008, Kan *et al* 2010, Houweling *et al* 2011, Fiorino *et al* 2011, Teshima *et al* 2010, Henriksson *et al* 1994). The clear correlation between parotid deformation and a number of clinical/ anatomical/ dosimetric parameters is very promising (Vásquez Osorio *et al* 2008, Fiorino *et al* 2011) (see also Chapter 3.2). Within this picture, the addition of the simple measurement of parotid density could be an important, additional measure of a likely surrogate of functional changes. Parotid density has been reported to be correlated with age (Drummond *et al* 1995, Percival *et al* 1994) and consequently to the measurement of the fibro-fatty component that is expected to be correlated to the reduction of the gland functionality.

Despite density changes measured after RT may be due to complex mechanisms, including inflammatory reactions, the prevalence of a significant reduction of density has been reported in few studies (Cardello *et al* 1998, Cheung *et al* 2010): very recently, preliminary results on 16 patients treated with image-guided IMRT for different head–neck cancers were reported, showing an average reduction of parotid density around 0.30 HU/fraction (Cheung *et al* 2010) which well compares with our findings (0.20–0.25 HU/fraction).

Izumi et al. (Izumi *et al* 1997), investigating patients affected by Sjogren Syndrome, suggested a correlation between a decrease in saliva production and HU variation on CT images. Two very recent works (Teshima *et al* 2012, Obinata *et al* 2013), published at the same time as our study, estimated density variations within parotid glands volume after irradiation, considering CT images of a small cohort of patients (6 and 10 subjects, respectively) and found a significant decrease of CT number, in accord with our results.

Our work is the first large multi-center study clearly reporting this phenomenon in a large cohort of patients, more evident when considering diagnostic kVCT. The higher noise of in-room imaging (like MVCTs) is a well known issue that limits the reliability of density measurements in this situation where a relatively small effect is expected. Then, although the prevalent effect of parotid density reduction was visible and statistically significant in our MVCT population, the individual assessment of density changes during Radiotherapy seems to be unfeasible. Moreover, the relationship between HU and density has been found to change with time in Tomotherapy MVCTs (Duchateau *et al* 2010) and this represents an additional noise in this kind of study; in order to investigate this effect in our MVCT population, the HU fluctuation between the start and the end MVCT was assessed for all patients by measuring ΔHU of a fixed region of interest (ROI) in the brain, outside the irradiated volume. We found that ΔHU of this ROI was correlated with the corresponding ΔHU in the parotids, confirming that the individual assessment of small density variations in parotids through MVCT is highly uncertain. MVCTs images could be maybe used for individual density changes by re-normalizing HU values following the method here used (using the HU change in a ROI outside the irradiated volume); investigating this possibility is outside the aims of current investigation. On the contrary, no significant variations were seen in the ROI for kVCT images, neither correlation with density changes in the parotids.

One of the major results of this study is the strong correlation between parotid deformation and density reduction. In particular, jacobian-based parameters, expressing the map of the voxel-by-voxel compression within the glands, were found to be highly related to density reduction. Similarly, the parotid volume reduction and the neck thickness reduction were found to be correlated with density changes, although with a smaller predictive value.

The reason of this effect may be hypothesized as due to a prevalent effect of loss of number and dimension of acinar cells, with a consequent relative increase of the fatty component of the

gland leading to the average density reduction. This hypothesis was confirmed in (Teshima *et al* 2012), where density reduction measured from CT images was correlated with histopathological images; in fact, histopathological analysis demonstrated that 30-Gy irradiation resulted in a loss of acinar cells in parotid glands. The CT values after RT were inversely correlated with adipose ratios ($r = –0.98$, $p < 0.01$) and there was a strong correlation between CT values before and after RT ($r = 0.97$, $p < 0.01$). The authors suggested that acinar cell loss is a main contributor to changes in the volume and function of irradiated human parotid glands and that the CT value may reflect the adipose ratio rather than salivary function.

Several other investigators suggested that the reduction of salivary flow is associated with this phenomenon, so that, the measurement of density changes is candidate to become an additional easy-to-measure and robust functional score (Teshima *et al* 2010, Drummond *et al* 1995, Konings *et al* 2005, Radfar and Sirois 2003). The combination of morphological and density information with direct functional information measured with other imaging modalities (in particular, diffusion MRI) gives high promise to better quantify and model functional changes within the parotids (Kan *et al* 2010, Houweling *et al* 2011, Castadot *et al* 2011, Wu *et al* 2011, Lee *et al* 2011, Juan *et al* 2009, Dirix *et al* 2008).

Interestingly, the best logistic model when considering kVCT data includes Jac_mean and the initial half-thickness of the neck, suggesting that larger patients tend to show a larger decrease in density; however, this result is much less robust than the impact of deformation and should be confirmed in a larger population. Moreover, neck thickness was found correlated with age and weight variation in our population, so that the fact that neck thickness could be a surrogate of these variables (primarily age) should not be excluded.

In this study, DVH parameters were weakly correlated with density changes while density changes were highly correlated with parotid deformation; this finding indirectly suggests that both parotid deformation and density changes may be only partly explained by

the planned dose distribution; on the other hand, the strong correlation between parotid shrinkage and density reduction implies that early deformation/volume loss may be helpful in assessing the most early-reacting patients. Recently, a clear correlation between early reduction of saliva flow and volume reduction was reported (Teshima *et al* 2010). A preliminary analysis between grade 3 acute xerostomia and Jac_mean, which showed a significant correlation in a sub-group of patients prospectively followed in one of the three Institutions (see results in Chapter 4.5), seems to confirm this hypothesis.

However, more investigation is necessary to assess the correlation between CT image-based scores (both morphology and density changes) and the clinical impact on acute and late xerostomia subjectively reported by the patient: the ability of damage repair as well as the adaptation of the patient to the new situation after Radiotherapy may significantly affect the relationship between objective image-based changes and the subjective perception of symptoms that may potentially affect the quality of life.

5.1.4. Dynamic characterization of structural modifications and their correlations with dosimetric parameter

Characterization of tissue organization can be carried out with texture analysis by studying the spatial variation in the intensity of image pixel values. In Chapter 4.3 texture analysis, based on the calculation of statistical parameters and fractal dimension, was used to extract quantitative and synthetic parameters for the description of structural variations in parotids occurring during the course of RT.

Therefore, in addition to the significant parotid volume decrease, extensively described in the previous chapters, and to the density decrease, which it was written about in the former chapter, in this section we found a significant decrease in S_2 (decrease of 11.4%, $p<0.001$) and FD (decrease of 5.8%, $p<0.001$) between the start and end of treatment, indicating a less complex tissue organi-

zation after irradiation. Texture analysis allows the identification of other features which characterize the structure of parotid glands with respect to simple mean density, and provides a deeper exploitation of the information content of CT images.

When the kinetic of textural features was studied, a different behavior was found for mean intensity changes (μ) with respect to S_2 and FD; specifically, mean intensity experienced a large decrease in the first half of the treatment (-4.69 HU, $p<0.001$) followed by a plateau in the second half (-0.59 HU, $p>0.05$), while both S_2 and FD showed significant variation between CT1 and CT_half and CT_half and CT_last (-5.9% and -5.4% for S_2; -3.4% and -2.4% for FD, $p<0.001$). The behavior of density variation is likely to be related to the rapid loss of water excretion in the first days after irradiation (Konings *et al* 2005).

Texture analysis was widely employed in several contexts on different imaging modalities, for example, to distinguish normal and abnormal tissues in the body, to characterize tumors as aggressive or non-aggressive, to classify different grades of pathologies or to segment different structures of interest. Statistical features were used to characterize tumor region (Ahammer *et al* 2011, Raja *et al* 2012), finding an increase in mean intensity value and entropy compared to normal tissue, and indicating more complex tissue organization when a neoplastic lesion was present. Specifically, in parotid glands, texture analysis was applied to extract statistical features from echographic images to characterize neoplastic lesions, with the same results (Chikui *et al* 2005). Focusing on radiation-induced changes in parotids, a very recent work compared parotids of normal subjects with parotids submitted to RT using ultrasound images (Yang *et al* 2012): the authors found an increase in tissue heterogeneity in post-RT subjects, with a significant increase in variance and entropy with respect to normal subjects. Our findings, reporting a significant decrease in local entropy and fractal dimension, thus associated with a global decrease in tissue complexity, are apparently in disagreement with their results; however, our study dealt with variations during treatment, while Yang *et al* compared normal sub-

jects with patients a year and a half after RT. Moreover, their research was based on ultrasounds, while we studied CT images, and the texture analysis thus captured different information. Specifically, tissue of normal parotid glands, filled with homogenous serous acinar cells, provides uniform and highly reflective interfaces for the ultrasound beam. After RT, the loss of acinar cells in parotids leads to a more disorganized tissue organization, appearing in ultrasound images as an heterogeneous echographic pattern. Our decrease in local entropy, seen with CT images, can be interpreted in the same way: resolution of CT images does not permit the analysis of single cells, and it is therefore possible to record a relative increase of fat ratio, making the tissue more uniform.

Fractal dimension was extensively calculated in different contexts, as a synthetic index of tissue complexity. However, to our knowledge, there are no studies employing this parameter to evaluate structural changes induced by radiotherapy, and our results cannot, therefore, be compared with others. In previous works FD was used to identify different regions of interest on CT images (Nailon *et al* 2008), or, again, to characterize properties of neoplastic tissue (Chikui *et al* 2005, Ahammer *et al* 2011, Raja *et al* 2012), also in parotid gland tumors, finding a fractal dimension higher than in normal subjects. Our study found a significant decrease in fractal dimension during the treatment, consistent with the decrease in mean intensity and local entropy.

Correlation analysis has reported a significant high relationship of local entropy variation with volume variation ($R=0.591$, $p<0.001$) and with density variation ($R=0.309$, $p<0.001$) during the whole treatment and between density and volume variation ($R=0.405$, $p<0.001$), as already reported previously. This result suggests that local entropy changes, being mostly correlated with volume changes, are related to the same biological process of volume decrease, i.e. the loss of acinar cells, while density variation is only partly explained by this phenomenon. FD resulted not correlated with any of these parameters, suggesting that this feature is not di-

rectly amenable to the same causes; however further investigations are needed.

Interestingly, correlation analysis with pre-treatment parameters gave significant results only for volume (already known in literature (Broggi *et al* 2010)) and density variation (as discussed previously), but no significant correlations were found for local entropy and only slight correlations for fractal dimension. Since Pearson's coefficients for DVH parameters could become significant if more patients were considered, the lack of correlation for S_2 and FD could be explained by the limited number of data. Also in this case, a deeper evaluation should be performed, in order to understand if dosimetric prescription and pre-treatment conditions have an influence on the textural variation.

Texture analysis methods can be approached in 2D or 3D, as widely discussed in the literature (Mahmoud-Ghoneim *et al* 2003, Xu *et al* 2004, Sanghera *et al* 2012). In our work the 2D approach was chosen as a simpler method to implement and we followed the method proposed in (Assefa *et al* 2010), using an intermediate solution between a slice based and a 3D texture analysis, i.e. the computation of the median value between textural parameters extracted for each slice separately. As discussed in a previous work (Xu *et al* 2004), when a structure is homogeneous, results obtained from 2D data and those obtained from volumetric data are similar. Moreover, our volumetric data are, in fact, a set of 2D images and the sparseness of the set of slices affects the result for volumetric data since the inter-pixel distance is different from the inter-slice distance. On the other hand, the 3D approach should prove more effective for very heterogeneous structures, or in volumetric data with a cubic voxel dimension. A comparison between 2D and 3D texture analysis deserves future investigation in order to intrinsically study three-dimensional variations on parotid gland structure.

Moreover, an analysis of the influence of misregistration errors should be carried out in order to understand if errors in recontouring parotid glands have a significant impact on the extraction of textural features. In this case, a possible solution to this

problem can be a morphological erosion of the structure, so that only the portion that certainly belongs to parotid gland would be taken into account.

5.1.5. Early prediction of parotid shrinkage using textural parameters

In Chapter 4.3 we have demonstrated that texture analysis is able to adequately characterize structural modification induced by RT on parotid glands tissue. In Chapter 4.4 we assessed the ability of textural features in early predicting parotid shrinkage at the end of RT. For this purpose, a verification of the significant variation of parameters in the first two weeks of RT was carried out. The decrease in tissue complexity was shown by the variation of some textural features confirmed even in the first two weeks of RT. Specifically, mean intensity and fractal dimension experienced significant variation between CT1 and CT2, with a decrease in μ of 1.7 HU ($p=0.042$) and in FD of 0.6% ($p=0.0045$). This result suggests that these features could be used as early predictors of the final parotid volume decrease, also considering that the extraction of textural features is a very fast process on a standard PC and requires very little extra effort.

The main finding of this chapter was that textural parameters seem to be effective in the timely prediction of parotid shrinkage at the end of RT. We have already shown that volume and mean density variation are strongly correlated to parotid shrinkage (Broggi *et al* 2010, Fiorino *et al* 2011); here, the simple volume variation seems to be sufficient to capture parotid gland modifications. However, it can be deduced that a multi-parameter analysis, combining volume with other textural parameters, and thus, at the same time, characterizing tissue structure and deformation of parotids, could provide more information than a single-parameter description for the identification of subjects with parotid anatomical variations at the end of RT. Although the volume and mean intensity variations alone achieved better discriminative results with respect to FD, the com-

bination of all these parameters gave more accurate classifications of parotid glands. The ability of FD to capture structural processes, probably related to finer differences in the functional behavior of parotid glands, with respect to V and μ could help in reaching a complete description of the effects induced by RT; in particular, the combination of FD and V was sufficient to obtain the best result.

This work is a preliminary study to investigate the feasibility of using texture analysis on CT images to characterize parotid variations induced by radiation. Considering the limited number of patients studied (21), although our data were sufficient to obtain significant results, a confirmation of these findings should be assessed in a larger dataset in order to verify the significance of textural indices in assessing parotid gland behavior and therefore the real impact of textural analysis in the clinical frame. In particular, correlations between textural features and clinical outcome need further investigation, also including other anatomical, clinical and dosimetric parameters, as proposed in previous works (Broggi *et al* 2010, Fiorino *et al* 2011, Beetz *et al* 2012), in order to understand whether these structural variations are related to the risk of xerostomia.

Moreover, this study could be extended by including other organs at risk, such as other salivary glands or structures related to swallowing, in the textural analysis, in order to provide a more comprehensive frame of the structural modification induced by RT in head and neck patients.

5.1.6. Relationship between structural indices and xerostomia

HNC patients are known to suffer relevant toxicity both during and after RT. Even in the IMRT era, xerostomia is one of the most important adverse side effects, often occurring after few weeks from the start of the treatment and persisting for many months/years after the end of RT and potentially affecting patient

quality of life (Tribius *et al* 2013, Deasy *et al* 2010, Bjordal *et al* 1994).

In Chapter 4.5 we have shown some preliminary results about the relationship between image-based features described in this thesis and the xerostomia scores recorded for a subgroup of patients. This is a very interesting issue, since if we can demonstrate that variations in parotid glands structure, as measured from CT images, are correlated with acute toxicity, an early detection of these changes could be used to adapt the treatment in the early phase and/or activating specific supportive therapies. For this reason, we considered variations that occur in the first part of the treatment, and in particular in the first two weeks.

From the results presented in Chapter 4.3 it was evidenced that parotid glands density changes are observed mostly during the first part of RT, while variations in volume, local entropy and fractal dimension are quite constant during the whole treatment. Therefore, measuring anatomical and structural variations in the first weeks can reasonably capture the most part of the significant information. Our preliminary results have shown significant correlations between acute xerostomia and early changes in volume and density, but no correlation was found for the other textural features. However, since only 21 patients were considered, and only the lowest value of features variation among the two parotid glands was used, the sample size was probably too small to obtain significant correlations for local entropy. Therefore, further investigations are needed in this direction to confirm or update our results.

Density variation seems to be a more robust parameter than volume reduction, being also less dependent on contouring. We have previously demonstrated that parotid glands density variation was highly correlated with deformation. Our hypothesis is that a decrease in gland density, corresponding to a relative increase in fat component, is a surrogate of acinar cell loss, thus resulting in an in-vivo functional score.

It should be noted that mean xerostomia was not correlated with the parotid glands DVH/mean dose (p-value>0.30, data not

shown). Of note, DVH shapes were quite homogeneous within the considered population (coefficient of Kurtosis for parotid mean dose: 5.3; p-value=0.0005).

Our results indicate early density changes as predictors of clinically significant symptoms; roughly, an early rΔρ reduction of about 0.50 HU/day, corresponding to about 3.5 HU/week was able to correctly classifying patients with a mean xerostomia score during treatment larger than the median value of the considered population.

In conclusion, our first results seem to highlight that early density and volume variations highly predict an increased risk of experiencing more intensive acute xerostomia symptoms. This finding could guide the activation of ART strategies based on early density changes assessment with the aim of reducing xerostomia; prospective validation of such strategies is mandatory as well as the confirmation of these results on a larger prospectively followed cohort of patients, where also the long-term effects should be considered (unfortunately the limited number of patients did not permit to include long-term xerostomia in current study).

On the other hand, it cannot be excluded that early density changes could be just a sign of an already occurred effect; in this case xerostomia could not be avoided by ART. In any case, this information could be highly important in early identifying sensitive patients and activating appropriate supportive therapies (Bohuslavizki *et al* 1999).

5.2. CONCLUSION

In this work, methods to extract CT-based indices to perform an extensive analysis of the effects of irradiation on parotid glands were proposed and evaluated. In particular, a framework composed by an image registration method, based on FFD and B-splines, and an automatic contour propagation algorithm, was validated and ap-

plied on kVCT and MVCT images, in order to estimate anatomical deformations that occur during RT treatment on parotid glands. Then, an image analysis method, based on texture analysis, was proposed to extract features able to characterize parotid glands structure.

These CT-based features were then correlated with pre-treatment parameters and we evidenced that parotid shrinkage is highly related to low dose DVH values; at the same time, density variation measured after RT is significantly correlated with volume decrease, suggesting that the loss of acinar cells and the consequent increase in the percentage of the fatty component is related to the decrease in functionality. Other textural features were estimated during treatment, showing a different behavior during time: in particular, we proved that the major reduction in density is concentrated in the first half of the treatment, while the decrease in volume and in tissue complexity (measured by local entropy and fractal dimension) is quite constant during the whole treatment. Texture and deformation analysis, thus, have been demonstrated to be able in characterizing morphological and structural modifications due to irradiation.

Finally, we tried to predict volume decrease and clinical outcome by using the early variations of textural features and we found that the most accurate prediction of parotid shrinkage is achieved by the combination of variation in volume, density and fractal dimension measured in the first two weeks. The prediction of xerostomia score is still an open challenge, since our results showed a significant correlation only with early density and volume variation, but our dataset was too small to generalize this conclusion.

Our results can help in adding new information and new instruments to evaluate the effects of RT on parotid glands, by performing texture analysis on the CT images acquired in the first half of the treatment. In fact, as the extraction of textural features is an easy and fast operation, it could be easily introduce in the clinical practice to obtain new scores for a multi-parameters evaluation of the RT consequences on normal tissues. In particular, the availability

of CT images acquired for patient repositioning allows the image-based analysis without requiring any other acquisition and without adding any cost. Moreover, the clinical usefulness of these analyses should be evidenced by a significant correlation of these features with xerostomia: if this could be confirmed in a larger population, the contribution of this work would be even more interesting and valuable.

5.3. FUTURE WORKS

Some improvements of the methods presented in this thesis could be faced in future. In particular, regarding the image registration method, the algorithm should be optimized in order to improve the computation time, making its performance almost in real-time. This can be achieved by the exploitation of multi-cores processors, after the parallelization of the code. Also the accuracy can be improved, by the introduction of space-variant multi-resolution approaches, which refine image registration only in regions of interest, or constrain the algorithm to not deform rigid structures, like bones.

Texture analysis can be also improved, by considering the extraction of more statistical and frequency-based features, which describe in detail every characteristic of the spatial pattern of the image. A classification of these features should then be performed by applying data clustering methods, able to identify the most powerful parameters in characterizing structural variations.

As already discussed in the previous paragraph, results about the correlation between density and volume variation and xerostomia scores should be confirmed by considering a larger population. If these correlations would remained significant and also local entropy would become significant, it should be taken into account that a check of textural features and deformation in the first two weeks of treatment could help in identifying those patients that could benefit of a replanning.

The assessment of the radiation-induced effects on parotid glands was here performed by considering CT images acquired during treatment, since the availability of these acquisitions is quite easy. If other modalities are available, like anatomic MRI, diffusion or perfusion MRI, functional imaging (PET or SPECT), this analysis can be extended to obtain a multi-parametric characterization of parotid tissue. The combination of this multi-modal information allows the evaluation of parotid behavior under different point of view, considering both anatomical and structural modifications through the analysis of CT and MRI images, and functional variations, in particular thanks to the investigation of diffusion MRI and PET images. In this regard, we have started to collect T2-w MRI images and Choline-PET images: the high resolution and contrast of MRI studies allows a better investigation of parotid tissue, since it is possible to distinguish the different macro-components of the glands; on the other hand, the functional measure, provided by PET studies, permits a direct correlation between textural and anatomical features and a quantitative clinical outcome.

Finally, the extension of all these methods to other structures of interest in the HN district can be possible and advisable. First of all, the other minor salivary glands can be taken into account: in fact, salivary production is measured independently from the secretory gland, and it is thus possible that not negligible damages registered on specific organs have a minor impact on the global salivary excretion. Second, other organs at risk can be considered, involved in other type of toxicity: for example, structures assigned to swallowing have a great impact on the quality of life of the irradiated patients. Only recently the clinical interest was focusing on this problem (Wall *et al* 2013), thanks to the new technologies which allow sparing these structures, and the assessment of the effects of radiation by applying image-based analysis is currently an open challenge.

REFERENCES

Abdoli, M, Ay, M R, Ahmadian, A and Zaidi, H 2009 Reduction of dental filling metallic artifacts in CT-based attenuation correction of PET data using weighted virtual sinograms *Nuclear Science Symposium Conference Record (NSS/MIC), 2009 IEEE* : IEEE) pp 2752-5

Ahammer, H, Kroepfl, J, Hackl, C and Sedivy, R 2011 Fractal dimension and image statistics of anal intraepithelial neoplasia *Chaos, Solitons & Fractals* **44** 1 86-92

Al-Kadi, O S and Watson, D 2008 Texture analysis of aggressive and nonaggressive lung tumor CE CT images *Biomedical Engineering, IEEE Transactions on* **55** 7 1822-30

Amenta, N, Choi, S and Kolluri, R K 2001 The power crust *Proceedings of the Sixth ACM Symposium on Solid Modeling and Applications* : ACM) pp 249-66

Assefa, D, Keller, H, Ménard, C, Laperriere, N, Ferrari, R J and Yeung, I 2010 Robust texture features for response monitoring of glioblastoma multiforme on T1-weighted and T2-FLAIR MR images: a preliminary investigation in terms of identification and segmentation *Med. Phys.* **37** 1722-36

Bajcsy, R 1973 Computer description of textured surfaces *Proceedings of the 3rd International Joint Conference on Artificial Intelligence* : Morgan Kaufmann Publishers Inc.) pp 572-9

Bal, M and Spies, L 2006 Metal artifact reduction in CT using tissue-class modeling and adaptive prefiltering *Med. Phys.* **33** 2852

Barker Jr, J L, Garden, A S, Ang, K K, O'Daniel, J C, Wang, H, Morrison, W H, Rosenthal, D I, Chao, K, Tucker, S L and Mohan, R 2004 Quantification of volumetric and geometric changes occurring during fractionated radiotherapy for head-and-neck cancer using an integrated CT/linear accelerator system *International Journal of Radiation Oncology* Biology* Physics* **59** 4 960-70

Bayouth, J E, Casavant, T L, Graham, M M, Sonka, M, Muruganandham, M and Buatti, J M 2011 Image-based biomarkers in clinical practice *Seminars in Radiation Oncology* : Elsevier) pp 157-66

Beetz, I, Schilstra, C, Burlage, F R, Koken, P W, Doornaert, P, Bijl, H P, Chouvalova, O, Leemans, C R, de Bock, G H and Christianen, M E 2012 Development of NTCP models for head and neck cancer patients treated with three-dimensional conformal radiotherapy for xerostomia and sticky saliva: The role of dosimetric and clinical factors *Radiotherapy and Oncology* **105** 1 86-93

Bhide, S A, Davies, M, Burke, K, McNair, H A, Hansen, V, Barbachano, Y, El-Hariry, I, Newbold, K, Harrington, K J and Nutting, C M 2010 Weekly volume and dosimetric changes during chemoradiotherapy with intensity-modulated radiation therapy for head and neck cancer: a prospective observational study *International Journal of Radiation Oncology* Biology* Physics* **76** 5 1360-8

Bjordal, K, Kaasa, S and Mastekaasa, A 1994 Quality of life in patients treated for head and neck cancer: a follow-up study 7 to 11 years after radiotherapy *International Journal of Radiation Oncology* Biology* Physics* **28** 4 847-56

Bohuslavizki, K H, Klutmann, S, Bleckmann, C, Brenner, W, Lassmann, S, Mester, J, Henze, E and Clausen, M 1999 Salivary gland protection by amifostine in high-dose radioiodine therapy of differentiated thyroid cancer *Strahlentherapie und Onkologie* **175** 2 57-61

Boldea, V, Sarrut, D and Clippe, S 2003 Lung Deformation Estimation with Non-Rigid Registration for Radiotherapy Treatment, *Medical Image Computing and Computer-Assisted Intervention-MICCAI 2003* : Springer) pp 770-7

Bondar, L, Hoogeman, M S, Osorio, E M V and Heijmen, B J 2010 A symmetric nonrigid registration method to handle large organ deformations in cervical cancer patients *Med. Phys.* **37** 3760

Bridge, Pand Tipper, D J 2011 *CT Anatomy for Radiotherapy* : M&K Update Ltd)

Broggi, S, Fiorino, C, Dell'Oca, I, Dinapoli, N, Paiusco, M, Muraglia, A, Maggiulli, E, Ricchetti, F, Valentini, V and Sanguineti, G 2010 A two-variable linear model of parotid shrinkage during IMRT for head and neck cancer *Radiotherapy and oncology* **94** 2 206-12

Bruhn, A, Weickert, J, Feddern, C, Kohlberger, T and Schnörr, C 2003 Real-time optic flow computation with variational methods *Computer Analysis of Images and Patterns* : Springer) pp 222-9

Bussels, B, Maes, A, Flamen, P, Lambin, P, Erven, K, Hermans, R, Nuyts, S, Weltens, C, Cecere, S and Lesaffre, E 2004 Dose–response relationships within the parotid gland after radiotherapy for head and neck cancer *Radiotherapy and oncology* **73** 3 297-306

Cardello, P, Trinci, M, Messineo, D, Tuccimei, M, Massa, R, Marini, M and Trinci, M 1998 Diagnostic imaging of the salivary glands in head and neck cancer after irradiation *Radiol. Med.* **95** 3 224-31

Castadot, P, Geets, X, Lee, J A and Grégoire, V 2011 Adaptive functional image-guided IMRT in pharyngo-laryngeal squamous cell carcinoma: Is the gain in dose distribution worth the effort?*Radiotherapy and Oncology* **101** 3 343-50

Castillo, R, Castillo, E, Guerra, R, Johnson, V E, McPhail, T, Garg, A K and Guerrero, T 2009 A framework for evaluation of deformable image registration spatial accuracy using large landmark point sets *Phys. Med. Biol.* **54** 7 1849

Chaudhuri, B and Sarkar, N 1995 Texture segmentation using fractal dimension *Pattern Analysis and Machine Intelligence, IEEE Transactions on* **17** 1 72-7

Cheung, J, Chen, Y, Lindberg, M, Cannon, B and Dong, L 2010 SU-GG-J-146: Evaluation of Parotid Density Changes during IMRT of Head-And-Neck Cancer *Med. Phys.* **37** 3179

Chikui, T, Tokumori, K, Yoshiura, K, Oobu, K, Nakamura, S and Nakamura, K 2005 Sonographic texture characterization of salivary gland tumors by fractal analyses.*Ultrasound Med. Biol.* **31** 10 1297-304

Christensen, G E, Song, J H, Lu, W, El Naqa, I and Low, D A 2007 Tracking lung tissue motion and expansion/compression with inverse consistent image registration and spirometry *Med. Phys.* **34** 2155

Chui, H and Rangarajan, A 2003 A new point matching algorithm for non-rigid registration *Comput. Vision Image Understanding* **89** 2 114-41

Cunliffe, A R, Al-Hallaq, H A, Labby, Z E, Pelizzari, C A, Straus, C, Sensakovic, W F, Ludwig, M and Armato III, S G 2012 Lung texture in serial thoracic CT scans: Assessment of change introduced by image registration *Med. Phys.* **39** 4679

Cunliffe, A R, Armato III, S G, Fei, X M, Tuohy, R E and Al-Hallaq, H A 2013 Lung texture in serial thoracic CT scans: Registration-based methods to compare anatomically matched regions *Med. Phys.* **40** 061906

Davatzikos, C, Vaillant, M, Resnick, S, Prince, J L, Letovsky, S and Bryan, R N 1996 Morphological analysis of brain structures using spatial normalization *Visualization in Biomedical Computing* : Springer) pp 355-60

Deasy, J O, Moiseenko, V, Marks, L, Chao, K, Nam, J and Eisbruch, A 2010 Radiotherapy dose–volume effects on salivary gland function *International Journal of Radiation Oncology* Biology* Physics* **76** 3 S58-63

Dice, L R 1945 Measures of the amount of ecologic association between species.*Ecology* **26** 297-302

Ding, K, Bayouth, J E, Buatti, J M, Christensen, G E and Reinhardt, J M 2010 4DCT-based measurement of changes in pulmonary function following a course of radiation therapy *Med. Phys.* **37** 1261

Dirix, P, De Keyzer, F, Vandecaveye, V, Stroobants, S, Hermans, R and Nuyts, S 2008 Diffusion-weighted magnetic resonance im-

aging to evaluate major salivary gland function before and after radiotherapy *International Journal of Radiation Oncology* Biology* Physics* **71** 5 1365-71

Dirix, P, Nuyts, S and Van den Bogaert, W 2006 Radiation-induced xerostomia in patients with head and neck cancer *Cancer* **107** 11 2525-34

Drummond, J, Newton, J and Abel, R 1995 Tomographic measurements of age changes in the human parotid gland *Gerodontology* **12** 1 26-30

Dubuc, B, Zucker, S, Tricot, C, Quiniou, J, Wehbi, D, Dubuc, B, Zucker, S, Tricot, C, Quiniou, J and Wehbi, D 1989 Evaluating the fractal dimension of surfaces *Proceedings of the Royal Society of London.A.Mathematical and Physical Sciences* **425** 1868 113-27

Duchateau, M, Tournel, K, Verellen, D, Van de Vondel, I, Reynders, T, Linthout, N, Gevaert, T, de Coninck, P, Depuydt, T and Storme, G 2010 The effect of tomotherapy imaging beam output instabilities on dose calculation *Phys. Med. Biol.* **55** 11 N329

Duma, M N, Kampfer, S, Wilkens, J J, Schuster, T, Molls, M and Geinitz, H 2010 Comparative Analysis of an Image-Guided Versus a Non–Image-Guided Setup Approach in Terms of Delivered Dose to the Parotid Glands in Head-and-Neck Cancer IMRT *International Journal of Radiation Oncology* Biology* Physics* **77** 4 1266-73

Eisbruch, A, Kim, H M, Terrell, J E, Marsh, L H, Dawson, L A and Ship, J A 2001 Xerostomia and its predictors following parotid-

sparing irradiation of head-and-neck cancer *International Journal of Radiation Oncology* Biology* Physics* **50** 3 695-704

Faggiano, E, Fiorino, C, Scalco, E, Broggi, S, Cattaneo, M, Maggiulli, E, Dell'Oca, I, Di Muzio, N, Calandrino, R and Rizzo, G 2011 An automatic contour propagation method to follow parotid gland deformation during head-and-neck cancer tomotherapy *Phys. Med. Biol.* **56** 3 775

Feng, J, van der Zwaag, M, Stokman, M A, van Os, R and Coppes, R P 2009 Isolation and characterization of human salivary gland cells for stem cell transplantation to reduce radiation-induced hyposalivation *Radiotherapy and Oncology* **92** 3 466-71

Fiorentino, A, Caivano, R, Metallo, V, Chiumento, C, Cozzolino, M, Califano, G, Clemente, S, Pedicini, P and Fusco, V 2012 Parotid gland volumetric changes during intensity-modulated radiotherapy in head and neck cancer *Br. J. Radiol.* **85** 1018 1415-9

Fiorino, C, Maggiulli, E, Broggi, S, Liberini, S, Cattaneo, G M, Dell'Oca, I, Faggiano, E, Di Muzio, N, Calandrino, R and Rizzo, G 2011 Introducing the Jacobian-volume-histogram of deforming organs: application to parotid shrinkage evaluation *Phys. Med. Biol.* **56** 11 3301-12

Fiorino, C, Rizzo, G, Scalco, E, Broggi, S, Belli, M L, Dell'Oca, I, Dinapoli, N, Ricchetti, F, Rodriguez, A M and Di Muzio, N 2012 Density variation of parotid glands during IMRT for head–neck cancer: Correlation with treatment and anatomical parameters *Radiotherapy and Oncology* **104** 2 224

Fisher, R A 1936 The use of multiple measurements in taxonomic problems *Ann. Hum. Genet.* **7** 2 179-88

Ganeshan, B, Miles, K A, Young, R C D and Chatwin, C R 2009 Texture analysis in non-contrast enhanced CT: Impact of malignancy on texture in apparently disease-free areas of the liver *Eur. J. Radiol.* **70** 1 101-10

Geets, X, Daisne, J, Arcangeli, S, Coche, E, Poel, M D, Duprez, T, Nardella, G and Grégoire, V 2005 Inter-observer variability in the delineation of pharyngo-laryngeal tumor, parotid glands and cervical spinal cord: comparison between CT-scan and MRI *Radiotherapy and oncology* **77** 1 25-31

Gose, E, Johnsonbaugh, R and Jost, S 1996 *Pattern Recognition and Image Analysis* : Prentice-Hall, Inc.)

Grundmann, O, Mitchell, G and Limesand, K 2009 Sensitivity of salivary glands to radiation: from animal models to therapies *J. Dent. Res.* **88** 10 894-903

Gulliford, S L, Foo, K, Morgan, R C, Aird, E G, Bidmead, A M, Critchley, H, Evans, P M, Gianolini, S, Mayles, W P and Moore, A R 2010 Dose–volume constraints to reduce rectal side effects from prostate radiotherapy: evidence from MRC RT01 Trial ISRCTN 47772397 *International Journal of Radiation Oncology* Biology* Physics* **76** 3 747-54

Han, C, Chen, Y, Liu, A, Schultheiss, T E and Wong, J Y 2008 Actual dose variation of parotid glands and spinal cord for nasopharyngeal cancer patients during radiotherapy *International Journal of Radiation Oncology* Biology* Physics* **70** 4 1256-62

Hansen, E K, Bucci, M K, Quivey, J M, Weinberg, V and Xia, P 2006 Repeat CT imaging and replanning during the course of IMRT for head-and-neck cancer.*Int. J. Radiat. Oncol. Biol. Phys.* **64** 2 355-62

Haralick, R M, Shanmugam, K and Dinstein, I H 1973 Textural features for image classification *Systems, Man and Cybernetics, IEEE Transactions on* 6 610-21

Hardcastle, N, Tomé, W A, Cannon, D M, Brouwer, C L, Wittendorp, P W, Dogan, N, Guckenberger, M, Allaire, S, Mallya, Y and Kumar, P 2012 A multi-institution evaluation of deformable image registration algorithms for automatic organ delineation in adaptive head and neck radiotherapy *Radiation Oncology* **7** 1 90

Hart, D J, Mootoosamy, I, Doyle, D V and Spector, T D 1994 The relationship between osteoarthritis and osteoporosis in the general population: the Chingford Study.*Ann. Rheum. Dis.* **53** 3 158

Heimann, T *et al* 2009 Comparison and evaluation of methods for liver segmentation from CT datasets *IEEE Trans. Med. Imaging* **28** 8 1251-65

Henriksson, R, Fröjd, O, Gustafsson, H, Johansson, S, Yi-Qing, C, Franzén, L and Bjermer, L 1994 Increase in mast cells and hyaluronic acid correlates to radiation-induced damage and loss of serous acinar cells in salivary glands: the parotid and submandibular glands differ in radiation sensitivity.*Br. J. Cancer* **69** 2 320

Herman, G T 2009 *Fundamentals of Computerized Tomography: Image Reconstruction from Projections* : Springer)

Horn, B K and Schunck, B G 1981 Determining optical flow *Artif. Intell.* **17** 1 185-203

Houweling, A C, Schakel, T, van den Berg, Cornelis AT, Philippens, M E, Roesink, J M, Terhaard, C H and Raaijmakers, C P 2011 MRI

to quantify early radiation-induced changes in the salivary glands *Radiotherapy and Oncology* **100** 3 386-9

Hughes, S W, D'arcy, T, Maxwell, D J, Saunders, J, Ruff, C, Chiu, W and Sheppard, R 1996 Application of a new discreet form of Gauss' theorem for measuring volume *Phys. Med. Biol.* **41** 9 1809

Huyskens, D P *et al* 2009 A qualitative and a quantitative analysis of an auto-segmentation module for prostate cancer *Radiother. Oncol.* **90** 3 337-45

Izumi, M, Eguchi, K, Nakamura, H, Nagataki, S and Nakamura, T 1997 Premature fat deposition in the salivary glands associated with Sjögren syndrome: MR and CT evidence.*Am. J. Neuroradiol.* **18** 5 951-8

Janssens, G, de Xivry, J O, Fekkes, S, Dekker, A, Macq, B, Lambin, P and van Elmpt, W 2009 Evaluation of nonrigid registration models for interfraction dose accumulation in radiotherapy *Med. Phys.* **36** 4268

Janssens, G, Jacques, L, de Xivry, J O, Geets, X and Macq, B 2011 Diffeomorphic registration of images with variable contrast enhancement *Journal of Biomedical Imaging* **2011** 3

Jellema, A P, Doornaert, P, Slotman, B J, Rene Leemans, C and Langendijk, J A 2005 Does radiation dose to the salivary glands and oral cavity predict patient-rated xerostomia and sticky saliva in head and neck cancer patients treated with curative radiotherapy?*Radiotherapy and oncology* **77** 2 164-71

Jeraj, R, Cao, Y, Ten Haken, R K, Hahn, C and Marks, L 2010 Imaging for assessment of radiation-induced normal tissue effects *In-*

ternational Journal of Radiation Oncology Biology* Physics* **76** 3 S140-4

Jorge. Nocedaland Wright, S J 1999 *Numerical Optimization* : Springer New York)

Juan, C, Chen, C, Jen, Y, Liu, H, Liu, Y, Hsueh, C, Wang, C, Chou, Y, Chai, Y and Huang, G 2009 Perfusion characteristics of late radiation injury of parotid glands: quantitative evaluation with dynamic contrast-enhanced MRI *Eur. Radiol.* **19** 1 94-102

Kalender, W A, Hebel, R and Ebersberger, J 1987 Reduction of CT artifacts caused by metallic implants.*Radiology* **164** 2 576-7

Kan, T, Kodani, K, Michimoto, K, Fujii, S and Ogawa, T 2010 Radiation-induced damage to microstructure of parotid gland: evaluation using high-resolution magnetic resonance imaging *International Journal of Radiation Oncology* Biology* Physics* **77** 4 1030-8

Katsuragawa, S, Doi, K and MacMahon, H 1988 Image feature analysis and computer-aided diagnosis in digital radiography: Detection and characterization of interstitial lung disease in digital chest radiographs *Med. Phys.* **15** 311

Kim, Y, Tomé, W A, Bal, M, McNutt, T R and Spies, L 2006 The impact of dental metal artifacts on head and neck IMRT dose distributions *Radiotherapy and oncology* **79** 2 198-202

Konings, A W, Cotteleer, F, Faber, H, van Luijk, P, Meertens, H and Coppes, R P 2005 Volume effects and region-dependent radiosensitivity of the parotid gland *International Journal of Radiation Oncology* Biology* Physics* **62** 4 1090-5

Konings, A W, Faber, H, Cotteleer, F, Vissink, A and Coppes, R P 2006 Secondary radiation damage as the main cause for unexpected volume effects: a histopathologic study of the parotid gland *International Journal of Radiation Oncology* Biology* Physics* **64** 1 98-105

Lee, C, Langen, K M, Lu, W, Haimerl, J, Schnarr, E, Ruchala, K J, Olivera, G H, Meeks, S L, Kupelian, P A and Shellenberger, T D 2008 Evaluation of geometric changes of parotid glands during head and neck cancer radiotherapy using daily MVCT and automatic deformable registration *Radiotherapy and Oncology* **89** 1 81-8

Lee, F K, King, A D, Kam, M K, Ma, B B and Yeung, D K 2011 Radiation injury of the parotid glands during treatment for head and neck cancer: assessment using dynamic contrast-enhanced MR imaging *Radiat. Res.* **175** 3 291-6

Li, Y, Taylor, J M, Ten Haken, R K and Eisbruch, A 2007 The impact of dose on parotid salivary recovery in head and neck cancer patients treated with radiation therapy *International Journal of Radiation Oncology* Biology* Physics* **67** 3 660-9

Liao, H, Nailon, W H, McLaren, D B and McLaughlin, S 2010 Classification of bladder cancer on Radiotehrapy planing CT images using textural features *18th European Signal Processing Conference (EUSIPCO-2010)* pp 284-8

Liu, S and Jernigan, M 1990 Texture analysis and discrimination in additive noise *Computer Vision, Graphics, and Image Processing* **49** 1 52-67

Lu, W, Olivera, G H, Chen, Q, Chen, M and Ruchala, K J 2006 Automatic re-contouring in 4D radiotherapy *Phys. Med. Biol.* **51** 5 1077

Lucas, B Dand Kanade, T 1981 An iterative image registration technique with an application to stereo vision.*IJCAI* pp 674-9

Mahmoud-Ghoneim, D, Toussaint, G, Constans, J M and de Certaines, J D 2003 Three dimensional texture analysis in MRI: a preliminary evaluation in gliomas *Magn. Reson. Imaging* **21** 9 983-7

Makkonen, T A, Tenovuo, J, Vilja, P and Heimdahl, A 1986 Changes in the protein composition of whole saliva during radiotherapy in patients with oral or pharyngeal cancer *Oral surgery, oral medicine, oral pathology* **62** 3 270-5

Mason, D Kand Chisholm, D M 1975 *Salivary Glands in Health and Disease* : WB Saunders London)

Mattes, D, Haynor, D R, Vesselle, H, Lewellen, T K and Eubank, W 2003 PET-CT image registration in the chest using free-form deformations *IEEE Trans. Med. Imaging* **22** 1 120-8

Maurer Jr, C R, Qi, R and Raghavan, V 2003 A linear time algorithm for computing exact Euclidean distance transforms of binary images in arbitrary dimensions *Pattern Analysis and Machine Intelligence, IEEE Transactions on* **25** 2 265-70

Meyer, E, Raupach, R, Lell, M, Schmidt, B and Kachelriess, M 2010 Normalized metal artifact reduction (NMAR) in computed tomography *Med. Phys.* **37** 10 5482-93

Murato, S and Saito, T 1999 The variogram method for a fractal model of a rock joint surface *Geotech. Geol. Eng.* **17** 3 197-210

Nailon, W H, Redpath, A T and McLaren, D B 2008 Characterisation of radiotherapy planning volumes using textural analysis *Acta Oncol.* **47** 7 1303-8

Nauta, M, Villarreal-Barajas, J E and Tambasco, M 2011 Fractal analysis for assessing the level of modulation of IMRT fields *Med. Phys.* **38** 5385

Obinata, K, Nakamura, M, Carrozzo, M, Macleod, I, Carr, A, Shirai, S and Ito, H 2013 Changes in parotid gland morphology and function in patients treated with intensity-modulated radiotherapy for nasopharyngeal and oropharyngeal tumors *Oral Radiology* 1-7

O'Daniel, J C, Rosenthal, D I, Garden, A S, Barker, J L, Ahamad, A, Ang, K K, Asper, J A, Blanco, A I, de Crevoisier, R and Holsinger, F C 2007 The effect of dental artifacts, contrast media, and experience on interobserver contouring variations in head and neck anatomy *American journal of clinical oncology* **30** 2 191-8

Østergaard Noe, K, De Senneville, B D, Elstrøm, U V, Tanderup, K and Sørensen, T S 2008 Acceleration and validation of optical flow based deformable registration for image-guided radiotherapy *Acta Oncol.* **47** 7 1286-93

Palma, D A, van Sörnsen de Koste, John R, Verbakel, W F and Senan, S 2011 A new approach to quantifying lung damage after stereotactic body radiation therapy *Acta Oncol.* **50** 4 509-17

Paquin, D, Levy, D and Xing, L 2009 Multiscale registration of planning CT and daily cone beam CT images for adaptive radiation therapy *Med. Phys.* **36** 4

Peitgen, H O, Saupe, D, Barnsley, M F, Fisher, Y and McGuire, M 1988 *The Science of Fractal Images* : Springer New York etc.)

Peleg, S, Naor, J, Hartley, R and Avnir, D 1984 Multiple resolution texture analysis and classification *Pattern Analysis and Machine Intelligence, IEEE Transactions on* 4 518-23

Pentland, A P 1984 Fractal-based description of natural scenes *Pattern Analysis and Machine Intelligence, IEEE Transactions on* 6 661-74

Percival, R, Challacombe, S and Marsh, P 1994 Flow rates of resting whole and stimulated parotid saliva in relation to age and gender *J. Dent. Res.* **73** 8 1416-20

Rabin, B M, Meyer, J R, Berlin, J W, Marymount, M H, Palka, P S and Russell, E J 1996 Radiation-induced changes in the central nervous system and head and neck.*Radiographics* **16** 5 1055-72

Radfar, L and Sirois, D A 2003 Structural and functional injury in minipig salivary glands following fractionated exposure to 70 Gy of ionizing radiation: an animal model for human radiation-induced salivary gland injury *Oral Surgery, Oral Medicine, Oral Pathology, Oral Radiology, and Endodontology* **96** 3 267-74

Raja, J, Khan, M, Ramachandra, V and Al-Kadi, O 2012 Texture analysis of CT images in the characterization of oral cancers involving buccal mucosa *Dentomaxillofacial Radiology* **41** 6 475-80

Robar, J L, Day, A, Clancey, J, Kelly, R, Yewondwossen, M, Hollenhorst, H, Rajaraman, M and Wilke, D 2007 Spatial and dosimetric variability of organs at risk in head-and-neck intensity-modulated radiotherapy *International Journal of Radiation Oncology* Biology* Physics* **68** 4 1121-30

Rueckert, D, Sonoda, L I, Hayes, C, Hill, D L, Leach, M O and Hawkes, D J 1999 Nonrigid registration using free-form deformations: application to breast MR images *Medical Imaging, IEEE Transactions on* **18** 8 712-21

Sanghera, B, Banerjee, D, Khan, A, Simcock, I, Stirling, J J, Glynne-Jones, R and Goh, V 2012 Reproducibility of 2D and 3D Fractal Analysis Techniques for the Assessment of Spatial Heterogeneity of Regional Blood Flow in Rectal Cancer *Radiology* **263** 3 865-73

Scalco, E, Fiorino, C, Cattaneo, G M, Sanguineti, G and Rizzo, G 2013 Texture analysis for the assessment of structural changes in parotid glands induced by radiotherapy *Radiotherapy and Oncology*

Sederberg, T Wand Parry, S R 1986 Free-form deformation of solid geometric models *ACM Siggraph Computer Graphics* : ACM) pp 151-60

Som, P M and Brandwein-Gensler, M 2011 Anatomy and pathology of the salivary glands *Head and neck imaging (5th ed).Elsevier Mosby* **2** 2449-609

Song, W Y, Chiu, B, Bauman, G S, Lock, M, Rodrigues, G, Ash, R, Lewis, C, Fenster, A, Battista, J J and Van Dyk, J 2006 Prostate contouring uncertainty in megavoltage computed tomography images acquired with a helical tomotherapy unit during image-

guided radiation therapy *International Journal of Radiation Oncology* Biology* Physics* **65** 2 595-607

Stephens, L, King, G, Peters, L, Ang, K K, Schultheiss, T and Jardine, J 1986 Acute and late radiation injury in rhesus monkey parotid glands. Evidence of interphase cell death.*The American journal of pathology* **124** 3 469

Teshima, K, Murakami, R, Tomitaka, E, Nomura, T, Toya, R, Hiraki, A, Nakayama, H, Hirai, T, Shinohara, M and Oya, N 2010 Radiation-induced parotid gland changes in oral cancer patients: correlation between parotid volume and saliva production *Jpn. J. Clin. Oncol.* **40** 1 42-6

Teshima, K, Murakami, R, Yoshida, R, Nakayama, H, Hiraki, A, Hirai, T, Nakaguchi, Y, Tsujita, N, Tomitaka, E and Furusawa, M 2012 Histopathological Changes in Parotid and Submandibular Glands of Patients Treated with Preoperative Chemoradiation Therapy for Oral Cancer *J. Radiat. Res.* **53** 3 492-6

Thévenaz, P and Unser, M 2000 Optimization of mutual information for multiresolution image registration *Image Processing, IEEE Transactions on* **9** 12 2083-99

Thirion, J 1998 Image matching as a diffusion process: an analogy with Maxwell's demons *Med. Image Anal.* **2** 3 243-60

Tomitaka, E, Murakami, R, Teshima, K, Nomura, T, Nakaguchi, Y, Nakayama, H, Kitajima, M, Hirai, T, Araki, Y and Shinohara, M 2011 Longitudinal changes over 2 years in parotid glands of patients treated with preoperative 30-Gy irradiation for oral cancer *Jpn. J. Clin. Oncol.* **41** 4 503-7

Tribius, S, Sommer, J, Prosch, C, Bajrovic, A, Muenscher, A, Blessmann, M, Kruell, A, Petersen, C, Todorovic, M and Tennstedt, P 2013 Xerostomia after radiotherapy *Strahlentherapie und Onkologie* **189** 3 216-22

Unser, M 1999 Splines: A perfect fit for signal and image processing *Signal Processing Magazine, IEEE* **16** 6 22-38

van Luijk, P, Faber, H, Schippers, J M, Brandenburg, S, Langendijk, J A, Meertens, H and Coppes, R P 2009 Bath and shower effects in the rat parotid gland explain increased relative risk of parotid gland dysfunction after intensity-modulated radiotherapy *International Journal of Radiation Oncology* Biology* Physics* **74** 4 1002-5

Vásquez Osorio, E M, Hoogeman, M S, Al-Mamgani, A, Teguh, D N, Levendag, P C and Heijmen, B J M 2008 Local anatomic changes in parotid and submandibular glands during radiotherapy for oropharynx cancer and correlation with dose, studied in detail with nonrigid registration *International Journal of Radiation Oncology* Biology* Physics* **70** 3 875-82

Vásquez Osorio, E M, Hoogeman, M S, Teguh, D N, Al-Mamgani, A, Kolkman-Deurloo, I K, Bondar, L, Levendag, P C and Heijmen, B J 2011 Three-dimensional dose addition of external beam radiotherapy and brachytherapy for oropharyngeal patients using nonrigid registration *International Journal of Radiation Oncology* Biology* Physics* **80** 4 1268-77

Vasquez-Osorio, E M, Hoogeman, M S, Romero, A M, Wielopolski, P, Zolnay, A and Heijmen, B J 2012 Accurate CT/MR vessel-guided nonrigid registration of largely deformed livers *Med. Phys.* **39** 2463

Veenland, J, Grashuis, J and Gelsema, E 1998 Texture analysis in radiographs: the influence of modulation transfer function and noise on the discriminative ability of texture features *Med. Phys.* **25** 922

Veenland, J, Grashuis, J, Van der Meer, F, Beckers, A and Gelsema, E 1996 Estimation of fractal dimension in radiographs *Med. Phys.* **23** 585

Vercauteren, T, Pennec, X, Perchant, A and Ayache, N 2009 Diffeomorphic demons: Efficient non-parametric image registration *Neuroimage* **45** 1 S61-72

Wang, H, Dong, L, Lii, M F, Lee, A L, de Crevoisier, R, Mohan, R, Cox, J D, Kuban, D A and Cheung, R 2005 Implementation and validation of a three-dimensional deformable registration algorithm for targeted prostate cancer radiotherapy *International Journal of Radiation Oncology* Biology* Physics* **61** 3 725-35

Wang, H, Dong, L, O'Daniel, J, Mohan, R, Garden, A S, Ang, K K, Kuban, D A, Bonnen, M, Chang, J Y and Cheung, R 2005 Validation of an accelerated'demons' algorithm for deformable image registration in radiation therapy *Phys. Med. Biol.* **50** 12 2887

Wang, H, Garden, A S, Zhang, L, Wei, X, Ahamad, A, Kuban, D A, Komaki, R, O'Daniel, J, Zhang, Y and Mohan, R 2008 Performance evaluation of automatic anatomy segmentation algorithm on repeat or four-dimensional computed tomography images using deformable image registration method *International Journal of Radiation Oncology* Biology* Physics* **72** 1 210-9

Wang, Z, Yan, C, Zhang, Z, Zhang, C, Hu, H, Kirwan, J and Mendenhall, W M 2009 Radiation-induced volume changes in parotid and submandibular glands in patients with head and neck can-

cer receiving postoperative radiotherapy: A longitudinal study *Laryngoscope* **119** 10 1966-74

Wei, J, Chen, L, Sandison, G A, Liang, Y and Xu, L X 2004 X-ray CT high-density artefact suppression in the presence of bones *Phys. Med. Biol.* **49** 24 5407

Wu, Q, Chi, Y, Chen, P Y, Krauss, D J, Yan, D and Martinez, A 2009 Adaptive replanning strategies accounting for shrinkage in head and neck IMRT *International Journal of Radiation Oncology* Biology* Physics* **75** 3 924-32

Wu, V, Ying, M and Kwong, D 2011 Evaluation of radiation-induced changes to parotid glands following conventional radiotherapy in patients with nasopharygneal carcinoma *Br. J. Radiol.* **84** 1005 843-9

Xu, D H, Kurani, A, Furst, J D and Raicu, D S 2004 Run-length encoding for volumetric texture *The 4th IASTED International Conference on Visualization, Imaging, and Image Processing* pp 6-8

Yang, X, Tridandapani, S, Beitler, J J, Yu, D S, Yoshida, E J, Curran, W J and Liu, T 2012 Ultrasound GLCM texture analysis of radiation-induced parotid-gland injury in head-and-neck cancer radiotherapy: an in vivo study of late toxicity *Med. Phys.* **39** 9 5732-9

Yazdia, M, Gingras, L and Beaulieu, L 2005 An adaptive approach to metal artifact reduction in helical computed tomography for radiation therapy treatment planning: experimental and clinical studies *International Journal of Radiation Oncology* Biology* Physics* **62** 4 1224-31

Yu, H, Caldwell, C, Mah, K, Poon, I, Balogh, J, MacKenzie, R, Khaouam, N and Tirona, R 2009 Automated radiation targeting

in head-and-neck cancer using region-based texture analysis of PET and CT images *International Journal of Radiation Oncology* Biology* Physics* **75** 2 618-25

Zhang, G G, Huang, T, Guerrero, T, Lin, K, Stevens, C, Starkschall, G and Forster, K 2008 The use of 3D optical flow method in mapping of 3D anatomical structure and tumor contours across 4D CT data *Journal of Applied Clinical Medical Physics* **9** 1

Zhang, T, Chi, Y, Meldolesi, E and Yan, D 2007 Automatic delineation of on-line head-and-neck computed tomography images: toward on-line adaptive radiotherapy *International Journal of Radiation Oncology* Biology* Physics* **68** 2 522-30

LIST OF PUBLICATIONS

Journal articles

1. Scalco E, Fiorino C, Cattaneo GM, Sanguineti G, Rizzo G. Texture analysis for the assessment of structural changes in parotid glands induced by Radiotherapy. Radiotherapy and Oncology, 2013. 109 (3), pp 384-387.

2. Fiorino C, Rizzo G, Scalco E, Broggi S, Belli ML, Dell'Oca I, Dinapoli N, Ricchetti F, Mejia Rodriguez A, Di Muzio N, Calandrino R, Sanguineti G, Valentini V, Cattaneo GM. Density variation of parotid glands during IMRT for head-neck cancer: correlation with treatment and anatomical parameters. Radiotherapy and Oncology, 2012. 104, pp 224-229.

3. Rubinacci A, Tresoldi D, Scalco E, Villa I, Adorni F, Moro GL, Fraschini GF, Rizzo G. Comparative high-resolution pQCT analysis of femoral neck indicates different bone mass distribution in osteoporosis and osteoarthritis. Osteoporosis International, 2012. 23 (7), pp 1967-1975.

4. Faggiano E, Fiorino C, Scalco E, Broggi S, Cattaneo M, Maggiulli E, Dell'Oca I, Di Muzio N, Calandrino R, Rizzo G. An automatic contour propagation method to follow parotid glands deformation during head-and-neck cancer Tomotherapy. Physics in Medicine and Biology, 2011. 56 (3), pp 775-791.

5. Rizzo G, Scalco E, Tresoldi D, Villa I, Moro GL, Lafortuna CL, Rubinacci A. An automatic segmentation method for regional analysis of femoral neck images acquired by pQCT. Ann Biomed Eng. 2011 Jan;39(1):172-84.

Proceedings of international conferences

1. Scalco E, Fiorino C, Cattaneo GM, Sanguineti G, Rizzo G. Texture analysis for the characterization of structural variations in parotid glands during radiotherapy. Radiotherapy & Oncology, 2013. 106, Supplement 2, p S211.

2. Belli ML, Scalco E, Fiorino C, Broggi S, Dinapoli N, Ricchetti F, Sanguineti G, Valentini V, Rizzo G, Cattaneo GM. Parotid density and volume variation in IMRT for head-neck cancer: predicting final changes from early variations. Radiotherapy & Oncology, 2013. 106, Supplement 2, p S224.

3. Ricchetti F, Belli ML, Cattaneo GM, Scalco E, Broggi S, Sanguineti G, Rizzo G, Fiorino C. Early density and volume variations of parotid glands are correlated with acute xerostomia during IMRT for HN cancer. Radiotherapy & Oncology, 2013. 106, Supplement 2, p S253.

4. Garelli S, Raso R, Scalco E, Vagge S, Bacigalupo A, Salvetti C, Passoni P, Broggi S, Rizzo G, Fiorino C. Rectal motion during radio-chemotherapy of rectal cancer assessed by daily MVCTs and 3D local shift measurements. Radiotherapy & Oncology, 2013. 106, Supplement 2, p S471.

5. Mejia-Rodriguez AR, Scalco E, Tresoldi D, Bianchi AM, Arce-Santana ER, Mendez M, Rizzo G. A mesh-based approach for the 3D analysis of anatomical structures of interest in Radiotherapy. Proceedings of the IEEE-EMBS 34th Annual International Conference. San Diego, California USA, August 28 - September 1, 2012, 6555-6558.

6. Broggi S, Fiorino C, Scalco E, Belli ML, Sanguineti G, Dinapoli N, Valentini V, Di Muzio N, Rizzo G, Cattaneo GM. Parotid deformation during imrt for head-neck cancer correlates with clinical

and dosimetry information. Radiotherapy & Oncology, 2012. 103, Supplement 1, p 579.

7. Fiorino C, Rizzo G, Scalco E, Belli ML, Dell'Oca I, Mejia Rodriguez AR, Ricchetti F, Sanguineti G, Valentini V, Calandrino R. Density variation of parotid glands during imrt: correlation with treatment parameters and parotid shrinkage. Radiotherapy & Oncology, 2012. 103, Supplement 1, p S163.

8. Salvetti C, Scalco E, Fiorino C, Passoni P, Broggi S, Maggiulli E, Slim N, Di Muzio N, Rizzo G, Calandrino R. 3D local rectal displacements during radio-chemotherapy of rectal cancer: reduced motion during treatment. Radiotherapy & Oncology, 2012. 103, Supplement 1, p S201.

9. Broggi S, Fiorino C, Scalco E, Belli ML, Dell'Oca I, Sanguineti G, Richetti F, Dinapoli N, Valentini V, Di Muzio N, Calandrino R, Rizzo G, Cattaneo GM. Quantitative parameters of parotid deformation during IMRT for Head-Neck cancer correlate with individually assessed clinical and dosimetry information. Radiotherapy & Oncology, 2012. 102, Supplement 1, p S48.

10. Mejia-Rodriguez AR, Arce-Santana ER, Scalco E, Tresoldi D, Mendez MO, Bianchi AM, Cattaneo GM, Rizzo G. Elastic Registration Based on Particle Filter in Radiotherapy Images with Brain Deformations. Proceedings of the IEEE-EMBS 33rd Annual International Conference. Boston Massachusetts USA, August 30 - September 3, 2011, 8049-8052.

11. Scalco E, Faggiano E, Liberini S, Fiorino C, Maggiulli E, Broggi S, Cattaneo GM, Calandrino R, Rizzo G. Validation of elastic registration to study parotid deformation in head and neck Tomotherapy. Radiotherapy & Oncology, 2011. 99, Supplement 1, p S339.

12. Broggi S, Maggiulli E, Fiorino C, Dell'Oca I, Sanguineti G, Scalco E, Cattaneo GM, Di Muzio N, Rizzo G, Calandrino R. Quantitative parameters of parotid deformation are highly correlated to DVH: evidence of a dose-bath effect around 15Gy. Radiotherapy & Oncology, 2011. 99, Supplement 1, p S36.

13. Fiorino C, Rizzo G, Broggi S, Cattaneo GM, Maggiulli E, Scalco E, Sanguineti G, Calandrino R. Image-based dose-volume effects prediction. Radiotherapy & Oncology, 2011. 99, Supplement 1, p S205-206.

Proceedings of national conferences

1. Scalco E, Fiorino C, Sanguineti G, Cattaneo GM, Rizzo G. Characterization of structural changes induced by Radiotherapy in parotid glands through texture analysis. 8° congresso nazionale AIFM 2013, Torino, 16-19 Novembre 2013.

2. Scalco E, Ravanelli D, Fellin F, Sutto M, Cattaneo GM, Schwarz M, Rizzo G. Evaluation of an image registration method for dose accumulation in proton therapy. 8° congresso nazionale AIFM 2013, Torino, 16-19 Novembre 2013.

3. Scalco E, Fiorino C, Sanguineti G, Cattaneo GM, Rizzo G. Metal artifacts reduction for Radiotherapy application. Atti del Congresso Nazionale di Bioingegneria, Roma, 26-29 Giugno 2012.

4. Mejia-Rodriguez AR, Scalco E, Tresoldi D, Belli ML, Bianchi AM, Fiorino C, Rizzo G. Analysis of 3D anatomical structures in radiotherapy: a mesh-based approach. Atti del Congresso Nazionale di Bioingegneria, Roma, 26-29 Giugno 2012.

Chapter in book

1. Rizzo G, Spinelli A, Scalco E. Tecniche di imaging tomografico non distruttivo in medicina rigenerativa. In "Approccio integrato per la medicina rigenerativa", a cura di Tanzi MC, Bianchi AM, Farè S, Mantero S, Raimondi MT, Visai L. Patron Editore, 2013. pp 229-251.

Ringraziamenti

Arrivata alla fine di questo lungo percorso sono tante le persone che voglio ringraziare, per avermi permesso di arrivare fino a qui e per aver condiviso con me questi 3 anni. E quindi grazie a...

Innanzitutto alla mia tutor Ing. Giovanna Rizzo, che mi ha permesso di lavorare nel suo laboratorio, mi ha introdotto nel mondo della ricerca, mi ha assegnato questo bellissimo progetto, mi ha insegnato tanto, mi ha dato fiducia, consigli e responsabilità che mi hanno permesso di crescere e che mi sprona a fare sempre meglio. Senza di lei non sarei mai arrivata fino a qui. Grazie!

Al Dott. Claudio Fiorino per il suo continuo contributo scientifico e il suo entusiasmo trasmesso in ogni incontro; a tutto il resto del gruppo di fisica sanitaria dell'Ospedale San Raffaele, Dott. Mauro Cattaneo, Dott.ssa Sara Broggi e in particolare alla Dott.ssa Maria Luisa Belli per tutto il tempo che mi ha dedicato e per le ore di lavoro condivise.

Ai miei fantastici colleghi e compagni di laboratorio che si sono succeduti negli anni (Daniele, Elisa, Sofia, Sara, Fabio, Mattia, Elena, Paolo, Paola, Cristina, Antonio, prof. Lafo) e soprattutto ad Aldo che ha diviso con me scrivania e codici di registrazione per 3 anni e che mi supporta ora dal Messico.

Ai miei genitori che ormai si sono rassegnati ad avere una figlia che non comincerà mai un lavoro vero, ma che studia sempre, e che mi dimostrano costantemente il loro appoggio e la loro fiducia in me; a tutta la mia famiglia che mi fa sentire il proprio sostegno.

A Massimiliano che ha condiviso con me ogni giorno di questo percorso.